陽極氧化鋁模版法製作奈米結構材料
及其電子場發射特性研究

研究生：陳德銘

指導教授：潘扶民 教授
張　立 教授

國立交通大學
材料科學與工程學系博士班

摘要

本實驗的實驗目的是製作出高規則性的奈米陣列結構，並探討其場發射性質。本實驗是藉由陽極氧化鋁(AAO)之高規則孔洞分佈薄膜作為模板，控制TiO_x奈米點之排列位置，並利用TiO_x奈米點陣列作為nanomask蝕刻下面的基材，製作出高規則性排列之奈米陣列結構，這些利用AAO薄膜作為模板，開發出來的場發射奈米結構包括：TiN奈米柱、Si奈米尖錐、Si奈米尖錐包覆一層α-C layer 與Si 奈米尖錐電鍍一層氧化銥。

實驗方法是在矽晶元上依序沉積 TiN 與 Al 薄膜，經由陽極氧化處理後得到 TiO_x 奈米點，利用 TiO_x 奈米點作為 nanomask，以活性離子蝕刻（RIE）系統蝕刻下面的 TiN 基材。TiN 奈米柱有與 AAO 孔洞相同的陣列結構。而 TiN 奈米柱在移除掉頂部的 TiO_x nanomask 之後，其頂端會呈現有環狀尖銳形貌的結構。TiN 奈米柱因為具有高深寬比與頂端環狀凸起結構，有利於降低場發射時的起始電壓。實驗發現在這種結構下，場發射的起始電場為 1.6

V/μm。並從 F–N plot 計算出，在這種環狀凸起結構下，對場發射增強因子有～26%的貢獻。本實驗也用相同的方式製作出 Si 奈米尖錐； TiN 薄膜經由陽極氧化處理後，得到與 AA0 孔洞排列相同的 TiO_x 奈米點。藉由 TiO_x nanomask 蝕刻下面的 Si 基材，可製作出 Si 奈米尖錐。本實驗並用微波電漿氣象化學沉積法，利用自生（in-situ）的方式，在 Si 奈米尖錐上沉積厚度約~5 nm 的 α-C layer。從 Raman 與 Auger 得知這層 α-C layer 是含有大量的奈米級的石墨結晶。這層奈米級的石墨結晶與尖錐形的幾何形狀，有助於得到較大的場發射增強因子。為了在電場作用下得較好的熱穩定性，本實驗利用脈衝電流的方式電鍍 IrO_2 奈米顆粒在 Si 奈米尖錐上。IrO_2 奈米顆粒的大小約小於 5 nm，並且均勻分佈在 Si 奈米尖錐上。由於 IrO_2/Si 奈米尖錐擁有小的曲率半徑與較低的功函數，比 Si 奈米尖錐有更好的場發射特性。

Fabrication of Nanostructured Materials by Anodic Aluminum Oxide Templation and Study of Their Electron Field Emission Characteristics

Student: Te-Ming Chen   Advisors: Prof. Fu-Ming Pan
                                                  Prof. Li Chang

Department of Materials Science and Engineering
National Chiao Tung University

Abstract

Fabrication of highly ordered nanostructures and investigation on the corresponding field emission characteristics were engaged with nanoporous anodic aluminum oxides (AAO) as templates to regulate the formation arrangement of TiO_x nanodot arrays, which were consequently employed as nanomasks to etch TiN layers and the underlying layers to manufacture nanostructures of highly ordered arrangements. Nanostructures developed by AAO templates included TiN nanopillars, Si nanotips, amorphous carbon coated silicon nanotips and IrO_2 electrodeposited on Si nanotips for field emitter applications.

Sequential deposition of TiN and Al on Si substrates and the successive electrochemical anodization of film stacks fabricated TiO_x nanodot arrays to be used as masks to reactive-ion-etch (RIE) the underlying TiN layers. TiN nanopillars arranged in a compliant pattern with AAO had a ridge-shaped edge on the top after the removal of TiO_x nanomasks. TiN nanorods with a high aspect ratio and the protruding top edge, of which the field enhancement effect was evaluated by the ellipsoidal cylinder model, showed a low turn-on voltage

of 1.6 V/μm. An underestimation by around 26% was found for comparison with the enhancement factor derived from the Fowler-Nordheim (F-N) plot.

Similar processes were performed for Si nanotips. During the preparation of well-ordered AAO pore channel arrays, underlying TiN layers were anodically oxidized as well in the late stage of the AAO anodization to form titanium oxide nanomasks for Si nanotip fabrication. Well-ordered Si nanotip arrays were produced as a result of the arrangement pattern transfer of AAO pore channel arrays to Si substrates with titanium oxide nanomasks by the plasma etch in the MPCVD system. α-C layers about 5 nm thick and rich in nanocrystalline graphitic carbons according to Raman and Auger electron spectroscopies were in-situ deposited on Si nanotips during the MPCVD process. Nanocrystalline graphitic carbons in the coating and the sharp tip shape improved Si nanotips as excellent field emitters with a large field enhancement factor. In order to obtain thermally stable field emitters with high field-emission efficiency, well dispersed IrO_2 nanoparticles with a uniform size distribution below 5 nm were deposited on ordered Si nanotips by bipolar pulse electrodeposition. Small curvature and lower work function assured IrO_2/Si nanotips to be superior to bare Si nanotips in field emission performance in terms of the turn-on field and the field enhancement factor.

Acknowledgement

Contents

Table Caption

Figure Caption

Chapter 1 Introduction

1.1 Introduction of nanomaterials

Exploiting materials below 100 nm have been proved to be fascinating for potential enterprise applications [1-5]. By manipulating the geometry of otherwise conventional materials into within the mesoscopic length scales comparable to mean free lengths, exciton radius or Fermi wavelength, unconventional physical properties arise due to size effects and surface reconstructions. There are many advantages in size reduction of electronic devices such as high integration density, faster response, lower cost and less power consumption, etc. Fabrication techniques of nanomaterials have been extensively studied by many researchers for electronic device developments. Emphasis has been focused in the whole world on nanostructured materials with different shapes, such as films, wires and dots, etc. Different geometries of nanoscale materials show various peculiar physical phenomena including size dependent excitation, ballistic conductance, coulomb blockade, single electron tunneling and metal-insulator transition. Studies on one-dimensional (1D) nanowires or nanotips can help to understand fundamental concepts and to realize such unusual physical properties as field emission.

Many techniques for nanomaterial preparation have been developed, for example electron-beam lithographic techniques and other chemical and physical approaches. The photolithography process is required for field emitter array fabrication when sizes and densities of field emitters are limited by the optical resolution of the lithography tool in conventional microfabrication. The electron-beam lithography is also not suitable for large-scale device fabrication. Thus, nanofabrication with Si wafers to prepare nanoscaled field emitters without photomasking have recently been developed. Anodic aluminum oxide (AAO) nanoporous structures prepared by electrochemical anodization of aluminum become the most potential candidate for templation. As shown schematically in Fig. 1-1, the

1

nanoporous structure is consisted of the self-organized vertical pore channel array with hexagonal arrangement. Porous alumina membranes are used to fabricate nanometer scale composites for their relatively regular structures with narrow size distributions of pore diameters and interpore spacings. Many techniques such as chemical vapor deposition (CVD) [7], microelectrode deposition [8] and thermal evaporation [9] are used to fill nanoholes in AAO membranes to accomplish nanostructures such as ordered nanodots, nanowires, nanopillars and nanotubes.
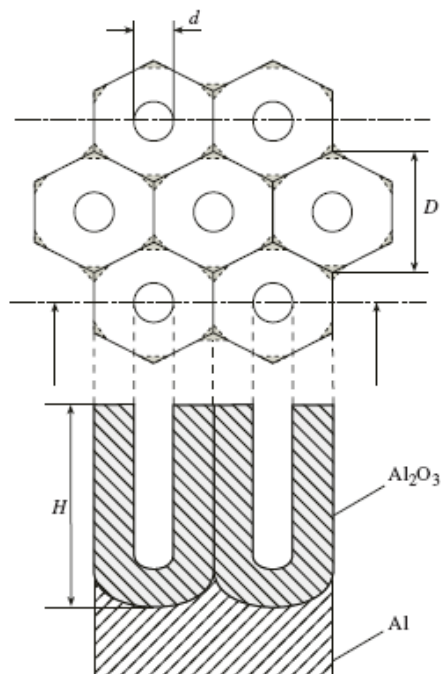
Figure 1-1 Diagrammatic representation of the surface and a cross section of a porous AAO [6].

1.2 Motivation

Different class of nanostructures, such as nanorod arrays and nanotubes has been successfully synthesized by using AAO membrane as growth templates. Nanostructure array fabrication process is, however, critically dependent on vertical pore channel. Several such factors as AAO/ nanostructure interfaced adhesion, interface condition and AAO conductivity are required to be taken into consideration in nanosructure synthesis, as shown in Fig 1-2. Presented below is a novel concept approach to fabricate ordered nanostructure arrays by templates with anodic aluminum oxides (AAO).

Ordered tip structure has attracted considerable attention due to the unique structure of small tip radius, high aspect ratio, unique physical properties and evident stabilities. It is well known that strcutured nanotips have excellent field emission characteristics and it is believed that the superior field emission properties are attributed to the large electric field enhancement due to the high aspect ratio at tips. One promising application of nanostructure is the electron emitter for field emission display and various vacuum microelectronic devices.

Proposed in this study is a reproducible and cheap method by employing nanoporous AAO films as templates for local anodic oxidation of metal films to fabricate ordered arrays of nanostructured metal oxides. The self-organized nanodot array of titanium oxide (TiO_X) in use is prepared from TiN/Al film on the silicon substrate by electrochemical anodization. This novel method can not only reveal highly ordered nanostructures but also overcome lithography limitation. TiO_X nanodots were then used as nanomasks to etch TiN layers and the underlying layers in an inductively coupled plasma reactive ion etch (ICP-RIE) system. The ICP-RIE is a plasma-based dry etching technique characterized by a combination of physical sputtering and chemical activity of reactive species. Owing to the well-controlled etching depth and profile for nanostructures, TiO_x nanodots were used as nanomasks to fabricate well

3

ordered Si nanocone field emitter arrays. Also used are TiO_x nanodots as nanomasks for the fabrication of TiN nanorod arrays and to study field emission characteristics of TiN emitters. In order to obtain thermally stable field emitters with high field-emission efficiency, IrO_2 nanoparticles were deposited on Si nanotips by bipolar pulse electrodeposition.
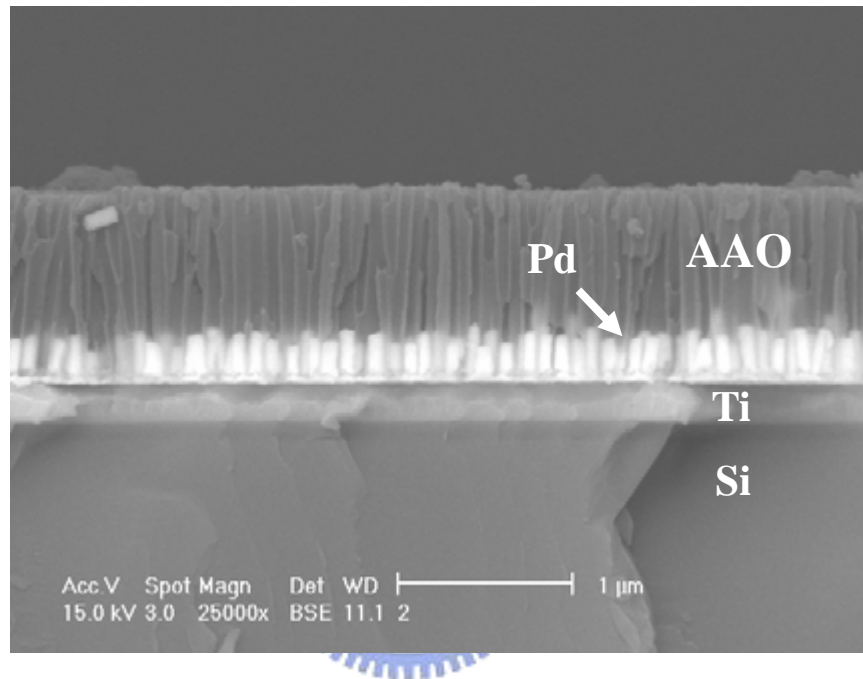
Figure 1-2. Cross-sectional SEM image of Pd nanowires grown in AAO template [10].

Chapter 2 Literature Review

2.1 Porous anodic aluminum oxide (AAO)

Porous alumina films formed by anodic oxidation of aluminum have been intensively studied for employment as molds to develop nanostructured materials. While the technology of porous alumina and its usage as an anodic oxide coating in tools has a long history, basic research on self organization of nanostructures via porous alumina templates began much more recently, namely in the mid-1990s. In 1998, O. Jessensky, et al. presented a theory based on mechanical stress to explain the naturally self-organized ordered structure. It suggested that the repulsive forces between neighboring pores caused by mechanical stress at the metal/oxide interface promote the formation of hexagonally ordered pore arrangement [11, 12]. A possible origin of the repulsive forces between neighboring pores is the mechanical stress, which is associated with the volume expansion during oxide formation at the metal/oxide interface. When Al is oxidized to alumina, the volume expands by approximately 2 times because the atomic density in alumina is 2 times lower than that in metallic aluminum, as shown in Fig. 2-1. But under experiment conditions, the expansion during oxidation is below twice the origin volume.
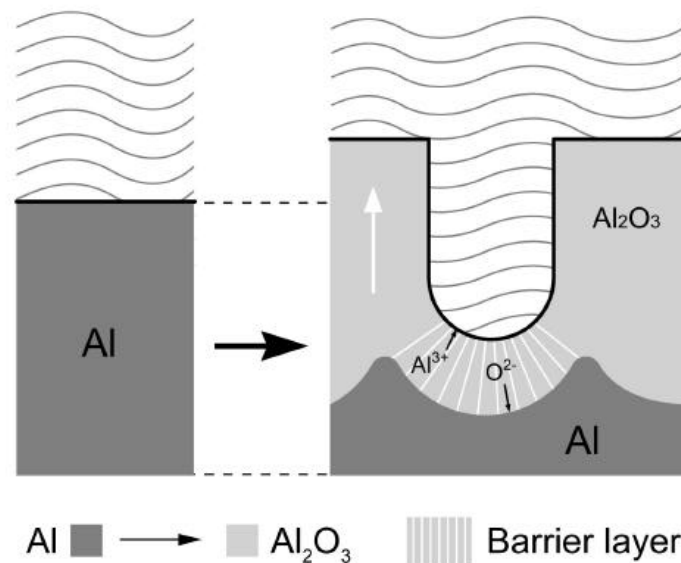
Figure 2-1 Expansion of aluminum during anodic oxide [11].

2.1.1 Principle of AAO formation

Because dissolved Al^{3+} ions are mobile in oxides under electric fields, the partially dissolved ions do not contribute to oxide formation. Although oxidation parameters, e.g., voltage, temperature and electrolyte are quite different for samples anodized in the three types of anodic acids (sulfuric, oxalic and phosphoric acid), the factor is chosen as 1.4 in order to obtain ordered pore arrangements regardless of electrolytes involved [12]. The chemical reaction of anodic alumina film is as followed [13]:

(1) Al^{3+} ions are formed at the metal/oxide interface and migrate into the oxide layer.

$$Al(s) \rightarrow Al^{3+} (oxide) + 3e- \qquad\qquad (2.1)$$

(2) At the oxide/electrolyte interface, the water-splitting reaction occurs. O^{2-} (oxide) ions migrate, due to the electric field, within the oxide from the oxide/electrolyte interface toward the metal/oxide interface to form Al_2O_3, as shown in Fig. 2-2. The oxide formation rate is controlled by Eq. 2.1 or 2.2, whichever is diffusion-controlled and slower.

$$3/2 H_2O_{(l)} \rightarrow 3 H^+_{(aq)} + 3/2 O^{2-}_{(oxide)} \qquad\qquad (2.2)$$

(3) Protons can locally dissolve oxides. The oxide dissolution rate must equal the rate of Eq. 2.3. About 30% of the current produced dissolved species, and the other 70% produced solid oxides.

$$1/2 Al_2O_{3(s)} +3H^+_{(aq)} \rightarrow Al^{3+}_{(aq)} + 3/2H_2O_{(l)} \qquad\qquad (2.3)$$
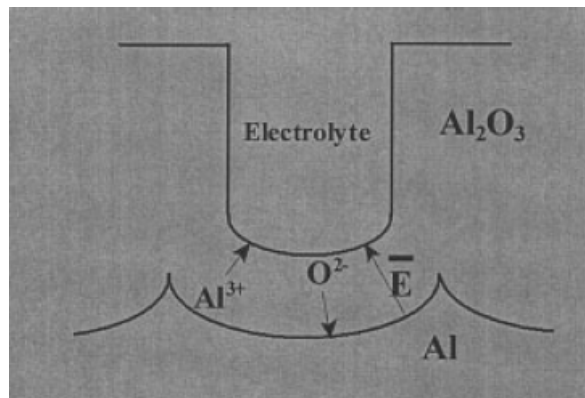
Figure 2-2 Movement of Al^{3+} ions through the oxide layer into electrolyte and movement of O^{2-} to pore bottom [14].

(4) Hydronium ions can also migrate toward the cathode, where they leave the electrolysis cell as H_2 gas and complete a circuit.

$$3H^+_{(aq)} + 3e^- \rightarrow 1/2\ H_{2(g)} \tag{2.4}$$

(5) At the bottom of pores, some possible competition between the water-splitting reaction (Eq. 2.2) and the acid dissociation may take place to form conjugate base anions to replace O^{2-} in oxides as substitution or contamination impurities within some depth, as indicated by the UMIST group [15,13].

$$HSO^{4-}_{(aq)} \rightarrow SO_4^{2-}{}_{(oxide)} + H^+_{(aq)} \tag{2.5}$$

$$H_2PO^{4-(aq)} \rightarrow HPO_4^{2-}{}_{(oxide)} + H^+_{(aq)} \tag{2.6}$$

$$HC_2O_4^-{}_{(aq)} \rightarrow C_2O_4^{2-}{}_{(oxide)} + H^+_{(aq)} \tag{2.7}$$
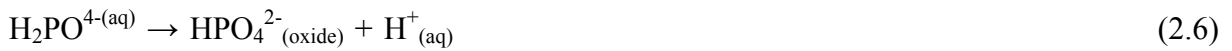
Porous oxide growth consists of several stages that can be observed from the characteristic behavior of current versus time for potentiostatic anodization or potential versus time for galavanostatic anodization. These stages of pore formation are schematically shown in Fig.2-3. When an anodic voltage is applied, a barrier layer of aluminum oxide forms on the surface of aluminum (stage I). Tiny cracks appear at the oxide/electrolyte interface and expand to form pores (stage II). Further anodization causes pores to accelerate and attain a constant dissolution speed (stage III). Such a well-developed pore structure consists of closely packed hexagonal cells each containing a long pore separated from the aluminum metal by a layer of scalloped oxide [16]. The geometric dimension and size of these pores are related to the anodizing conditions (applied voltage, acid concentration of the electrolyte and temperature).

Figure 2-4 plots the linear relationship between the interpore distance (or pore cell size) and the applied voltage in three types of electrolytes[19]. The best self-organized ordered structures occur at 25V in sulfuric acid, 40V in oxalic acid and 195V in phosphoric acid [15,17,18] , corresponding to cell sizes of 65, 100 and 500 nm, as shown in Fig. 2-5.
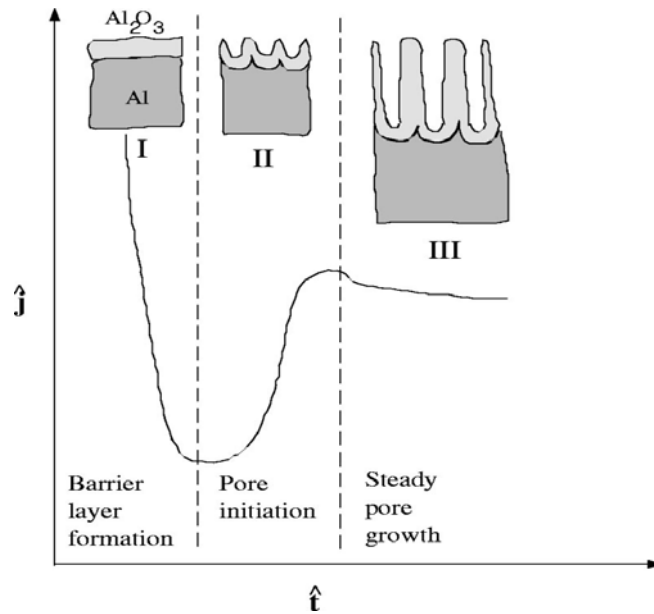
Figure 2-3 Schematic diagram showing the characteristic current density versus time
for a constant voltage anodization of aluminum in an acidic electrolyte [16].

The barrier thickness is in proportional to the applied voltage, and the relation of wall
diameter is: phosphoric acid > chromic acid > oxalic acid > sulfuric acid. The lower anodizing
voltage in sulfuric acid results in the formation of a thinner undesired barrier layer and higher
pore-density AAO.
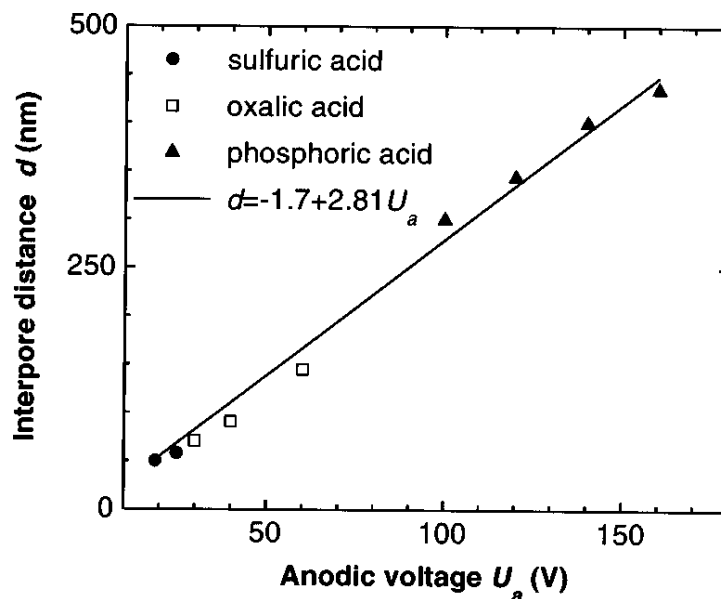
Figure 2-4 Interpore distance *d* in self-organized porous alumina vs anodic voltage *Ua*
for sulfuric, oxalic, and phosphoric acid solutions [19].

8
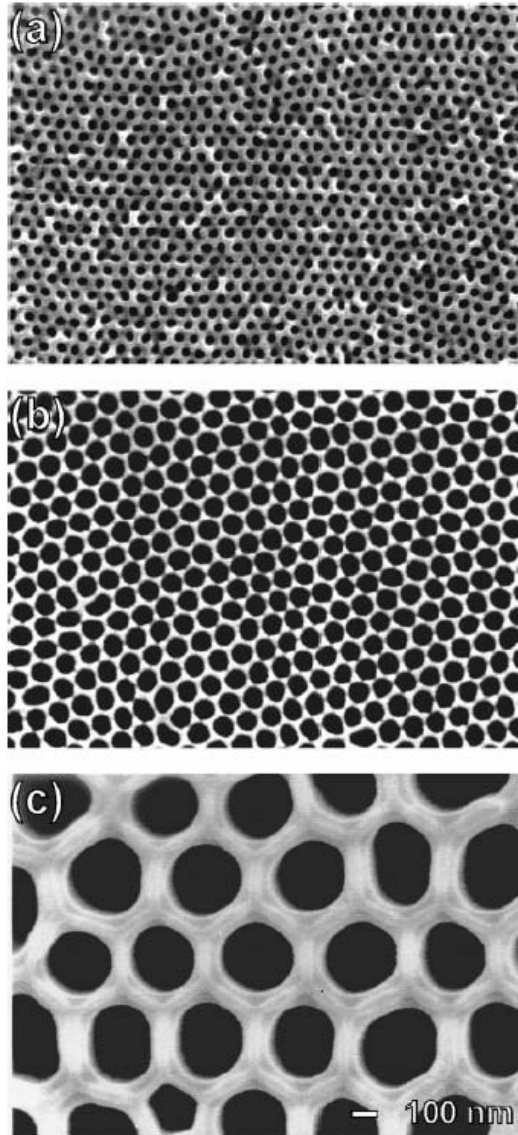
Figure 2-5 SEM micrographs of the bottom view of anodic alumina layers. Anodization was conducted in (a) 0.3 M (1.7 wt %) sulfuric acid at 10 °C and 25 V , (b) 0.3 M (2.7 wt %) oxalic acid at 1 °C and 40 V and (c) 10 wt % phosphoric acid at 3 °C and 160 V. Pore opening was carried out in 5 wt % phosphoric acid (a) at 30 °C for 30 min, (b) at 35 °C for 30 min   and (c) at 45 °C for 30 min. The thickness of oxide films was approximately 120 mm [19].

2.1.2 AAO application

AAO templates have been widely used to construct highly ordered, purposefully designed and massively parallel nanotubes[20, 21], nanofibres[22], nanowires[23, 24, 25], nanorods[26,27] and nanodots[28, 29] of metals, semiconductors, carbons, polymers and

other solid materials. Nanopores filled with desired materials by electrochemical[30, 31] and electroless [32] depositions, sol-gel deposition[33], hydrolysis process[34, 35], physical vapor deposition (PVD)[36] and chemical vapor deposition (CVD)[37, 38, 39] are major template synthetic approaches.
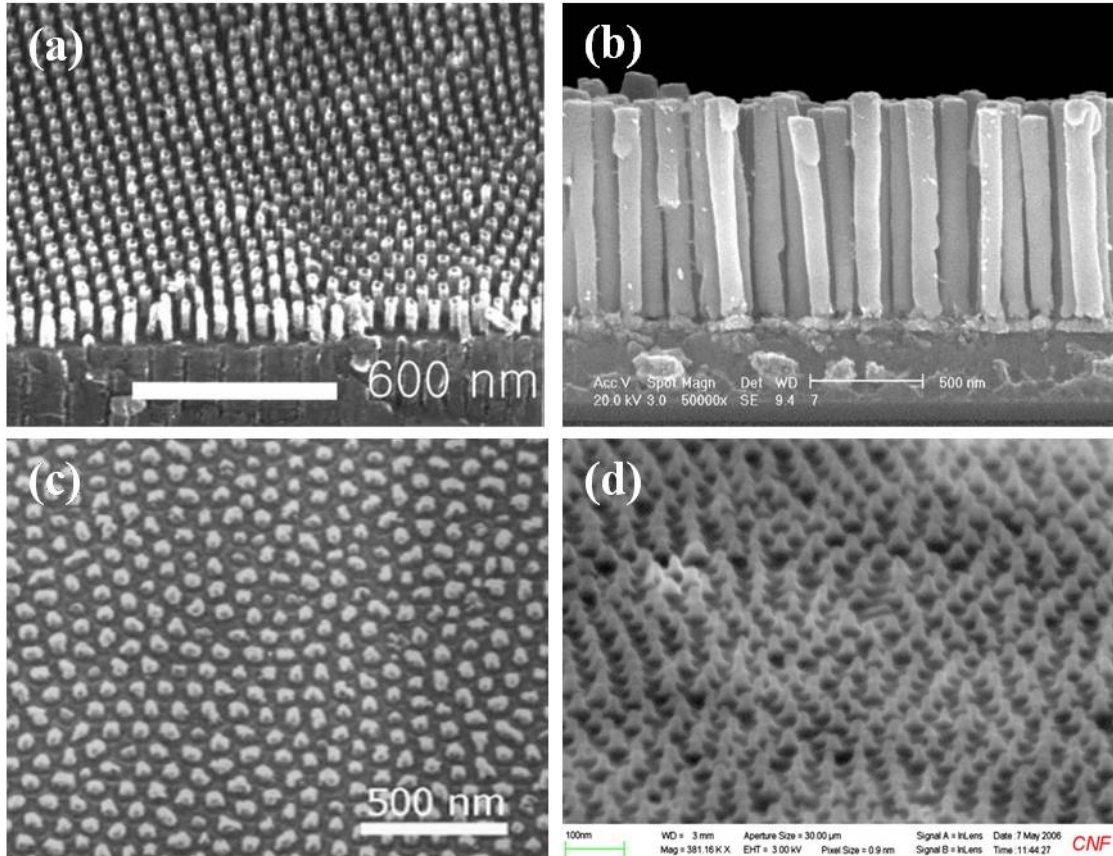
Figure2-6 (a) CNTs grown by pyrolysis of acetylene into cobalt-embedded AAO templates
(b) Pd nanowires standing freely on substrates after removing AAO templates
(c) Titanium oxide nanodot arrays after removing nanoporous AAO templates
(d) CdTe QD arrays after removing nanoporous AAO templates [20,26,28,29]

2.2 Field Emission Theory

Electron field emission is a quantum-mechanical tunneling phenomenon of electrons extracted from a conductive solid surface, such as a metal or semiconductor, into vacuum in response to a very high electric field. Under the influence of a field, these conduction electrons can be induced to tunnel through the barrier into vacuum and produce a

field-induced electron emission from the metal surface. The presence of the electric field makes the width of the potential barrier finite and therefore permeable to electrons. Fig. 2-7 presents such a diagram of the electron potential energy at the surface of a metal. Fowler and Nordheim further assumed that the surface barrier can be approximated with a one dimensional energy function without losing significant accuracy. The dashed line in Fig. 2-7 shows the shape of the barrier in the absence of an external electric field. The height of the barrier is equal to the work function of the metal, ϕ, which is defined as the energy required to remove an electron from the Fermi level, E_F, of the metal to a rest position just outside the material (the vacuum level). The solid line in Fig. 2-7 corresponds to the shape of the barrier in the presence of the external electric field.
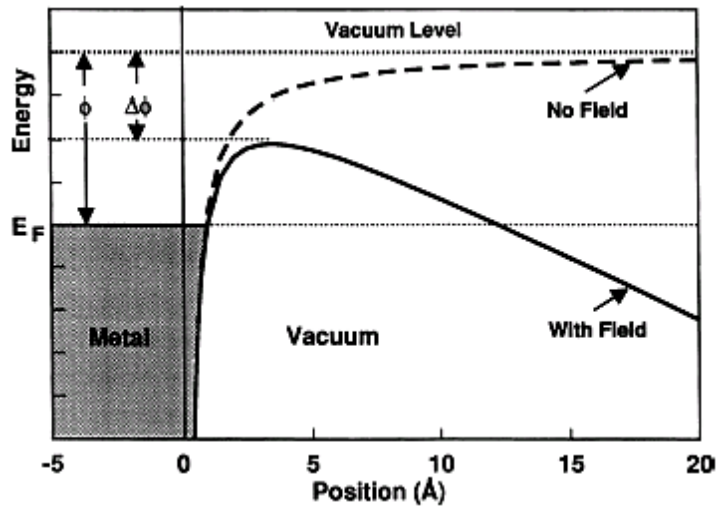
Figure 2-7 Potential-energy diagram illustrating the effect of an external electric field on the energy barrier for electrons at the metal surface [40].

In addition to that the barrier becomes triangular in shape, the height of the barrier in the presence of the electric field E becomes smaller by a magnitude given by [41]

$$\Delta\phi = \left(\frac{eE}{4\pi\varepsilon_0} \right)^{1/2} \tag{2.8}$$

where e is the elementary charge and ε_0 is the permittivity of vacuum. The probability of an electron with a given energy tunneling through the barrier can be calculated by energy barrier shape. Integrating the probability function multiplied by an electron supply function in the available range of electron energies brings about an expression for the tunneling current density J as a function of the external electric field E. The tunneling current density can be expressed by Eq. (2-9) which is often referred as the Fowler-Nordheim equation [42]

$$ J = \frac{AE^2}{\phi t^2(y)} \exp\left[-\frac{B\phi^{3/2} v(y)}{E} \right] \tag{2.9} $$

where $A = 1.54 \times 10^{-10}$ (A V^{-2} eV), $B = 6.83 \times 10^9$ (V eV$^{-3/2}$ m^{-1}), $y = 3.7947 \times 10^{-4} E^{1/2} / \phi$, $t^2(y) \sim 1.1$, and $v(y)$ can be approximated by

$$ v(y) = \cos(0.5\pi \ y) \text{ or } v(y) = 0.95 - y^2 \tag{2.10} $$

In general, the field emission current (I) is measured as a function of the applied voltage (V). Substituting relationships of $J = I/\alpha$ and $E = \beta V/d$ into Eq. 2.9, where α is the emitting area, β is the local field enhancement factor at the emitting surface and d is the distance between cathode and anode, following equation can be obtained:

$$ I = \frac{A\alpha\beta^2 V^2}{d^2 \phi t^2(y)} \exp\left[-\frac{Bd\phi^{3/2} v(y)}{\beta V} \right] \tag{2.11} $$

In addition, the Napierian logarithm form of Eq. 2.11 can be expressed as

$$ \ln\left(\frac{I}{V^2}\right) = \ln\left[\frac{A\alpha\beta^2}{d^2 \phi t^2(y)}\right] - \frac{Bd\phi^{3/2} v(y)}{\beta V} \tag{2.12} $$

By using $v(y) \sim 1$ in Eq. (2.10), it gives

$$\ln\left(\frac{I}{V^2}\right) = \ln\left[\frac{A\alpha\beta^2}{d^2\phi t^2(y)}\right] - \frac{Bd\phi^{3/2}}{\beta V}$$

(2.13)

Here, a plot of $\ln(I/V^2)$ versus $1/V$ yields a linear curve. This plot is the well known F-N plot. From Eq. (2.13), the slope (S) of the F-N plot is given by

$$S = -\frac{Bd\phi^{3/2}}{\beta}$$

(2.14)

The value of field enhancement factor can be estimated from the slope of the measured F-N curve if the work function of emitter is known. All the field emission sources rely on the field enhancement due to sharp tips or high aspect ratio of protrusions, so emitters tend to have smaller virtual source sizes because of the primary role of the β factor. Smith et al.[43] demonstrated that for low separation (D) of anode to cathode, β is a function of D, h (height of the protrusion) and r (hemispherical cap of radius), but for high D, β is a function of h and r only.

In normal cases, the field emission current does not achieve the predicted value since nanostructures are usually synthesized with massive units. In fact, for high density films, screening effects reduce the field enhancement and the emitted current. For films of medium density, there is an ideal compromise between the emitter density and the inter-emitter distance, which is sufficiently large to avoid screening effects. A better control of density and morphology (β factors) of films is undoubtedly required for future applications.

Previous report revealed that the field emission property of carbon nanotubes could be affected by the field-screening effect provoked by the proximity of neighboring tubes. According to the prediction of Nilsson et al.[44], field emission maximum when the height of CNTs is about one half the intertube distance, as shown by Fig. 2-8. AAO films have been

extensively used in past few years as templates to avoid field-screening [45].
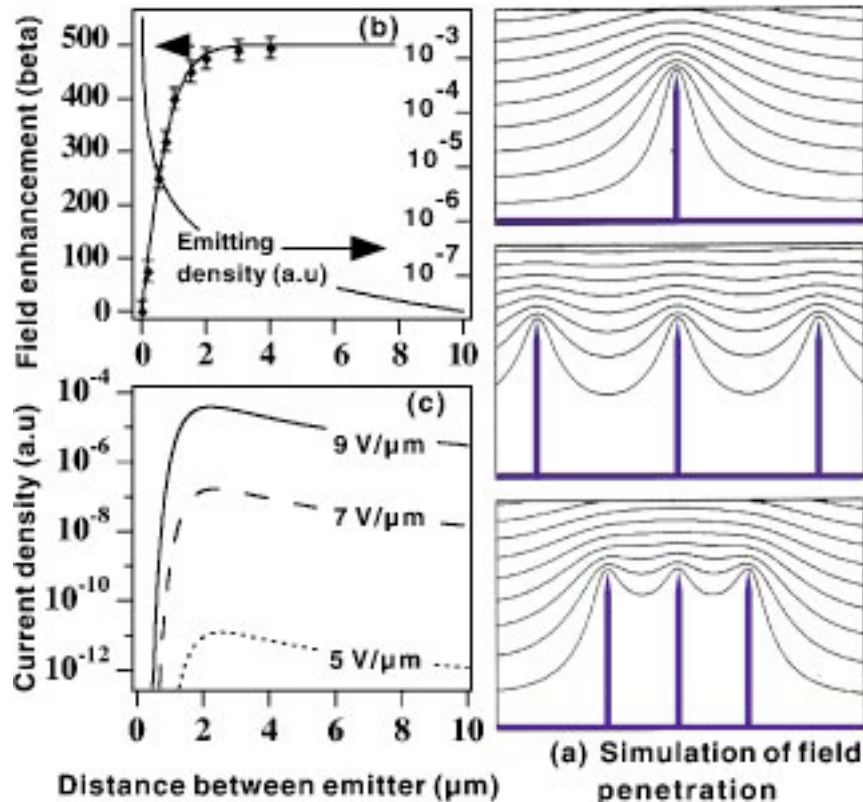
Figure 2-8 (Color) (a) Simulation of equipotential lines of the electrostatic field for tubes of 1 mm height, 2 nm radius and tube separation distances of 4, 1 and 0.5 mm along with the corresponding changes of the field enhancement factor β (b) emitter density and (c) current density as functions of the distance [44].

2.3 Field Emitter materials

Properties preferred for field emitter materials include a stable surface work function, excellent thermal mechanical properties and the capability to achieve high aspect structures to enable operation at low applied fields. In addition, the emitter material should be low in chemical reactivity and permit long term device operation in sealed vacuum packages.

2.3.1 Si nanotip emitter

Crystalline Si has long been applied as the starting material to fabricate Spindt-type field

emitters because of the excellent electronic mechanical properties and well-developed microfabrication processes, as shown in Fig. 2-9. There are many approaches developed to fabricate Si nanotips. Lithographical technique is normally employed to produce silicon tip arrays with tip sizes even below 10 nm in diameter [47,48]. Chen *et al*.[49] and Bai *et al*.[50] synthesized high-density cone-shaped silicon by a plasma-assisted hot-filament chemical vapor deposition process with gas mixture of hydrogen, nitrogen and methane. Hsu *et al*.[51] presented the one-step and self-masked dry etching procedure to fabricate uniform and high-density nanotip arrays over a large area in a high-density electron cyclotron resonance (ECR) plasma reactor. Reactive gases comprised argon (Ar), H_2, methane (CH_4) and silane (SiH_4) with 10% dilution in helium. Johnson *et al*.[52] prepared silicon nanostructure arrays on *n*- and *p*-type silicon (100) substrates by electron beam rapid thermal annealing. Arrays of nanostructures with an average height of 8 nm were formed by substrate annealing at 1100 °C for 15 seconds. Shimizu *et al*.[53] utilized an anodic aluminum oxide template with vertical nanopores to grow epitaxial Si(100) nanowires on a Si(100) substrate. Nanowires were grown by the vapor – liquid – solid (VLS) technique. Zorba *et al*.[54, 55] studied duration pulsed laser formation of self-organized Si spikes formed in the SF_6 atmosphere. The irradiating laser source was constituted by a distributed-feedback dye-laser-based KrF system. This is a simple one-step production method of quasiperiodical microtip arrays. Seeger *et al*.[56] demonstrated that reactive ion etching mixture of SF_6 and CF_4 gases led to anisotropic etching arising from the polymer deposition on sidewalls of pillars and inhibited undercut of the rough silver film masks. Fung *et al*.[57] fabricated highly dense silicon field emitter with random distribution in KOH and IPA solutions without any masking. Huang *et al*.[58] used Si-based porous anodic alumina membrane as a mask to pattern Si substrate. The Si nanotip array was obtained from removing SiO_2 nanoislands formed during the anodization of the Al/Si interface. However, preparation methods without photomasking do not usually provide a growth process to regulate the arrangement of nanosized field emitters. In this study, TiO_x

nanodots were prepared with porous anodic aluminum oxides as templates and were used as
masks to fabricate highly ordered Si nanotips.
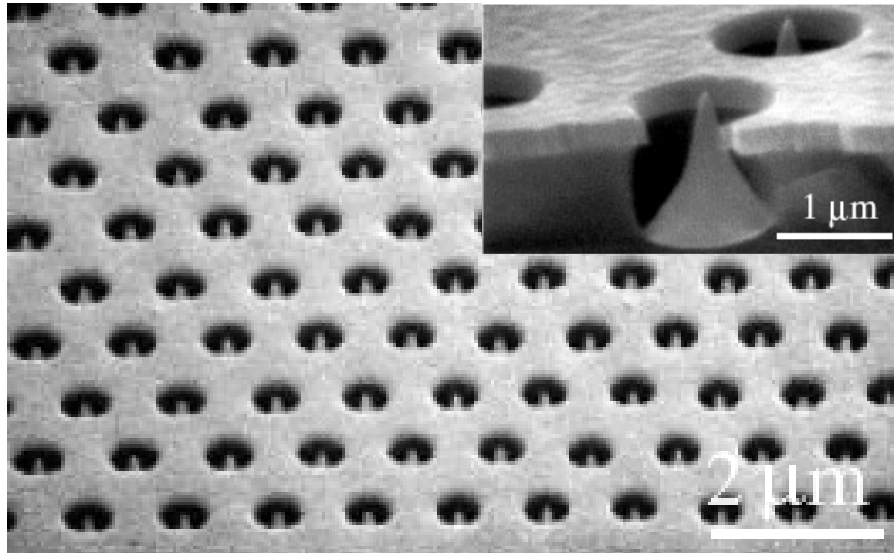
Figure 2-9 Scanning electron micrographs of Spindt cathodes: (a) a portion of a 50 000- tip
array with a tip packing density of 10^8 tips/cm^2 and (b) a cross-sectional view of
a single molybdenum Spindt emitter [46].

2.3.2 TiO$_2$ and TiN emitter

2.3.2.1 Titanium oxides (TiO$_2$)

TiO$_2$ have been intensively studied because of the large surface area and quantum size effects which result in novel chemical, optical and electrical properties. Most previous studies used sol-gel [59], hydrolysis process [60], thermal deposition method [61] and electrochemical anodization of TiN layers [62] to prepare TiO$_2$ nanostructures.

Phase transformation of TiO$_2$ has been widely surveyed owing to both scientific interest and technological applications. TiO$_2$ has three crystalline phases, i.e., rutile, anatase and brookite. Rutile is the thermodynamically stable phase in all temperatures and pressures, while anatase and brookite are metastable phases [63]. Anatase is the TiO$_2$ phase of greatest commercial interest although seldom found in natural. However, when the crystal size decreases below a certain size, anatase phase becomes more stable than rutile [64]. It is well known that as the size of a particle decreases, surface/volume ratio increases. For the phase transformation of nanocrystalline anatase to rutile, the change of molar standard free energy (ΔG^o) (J/mol) can be described as [65]

$$\Delta G^0 (J/mol) = -6140.9047 + \frac{87921.012}{D} \tag{2.15}$$

where D is in nm. Figure 2-10 shows the variation of ΔG^o with D at 300 K. Particle sizes crucially determine the thermodynamic phase stability at ultrafine sizes. According to the calculated results, when particle size decrease below *ca.* 14 nm, the total free energy of rutile is higher than that of anatase and anatase becomes the thermodynamically stable phase because the relative phase stability of anatase and rutile reverse. This is the consequence that rutile has a higher surface energy than anatase, and thus the relative phase stabilities of anatase and rutile reverse as the particle size is reduced to a critical value.
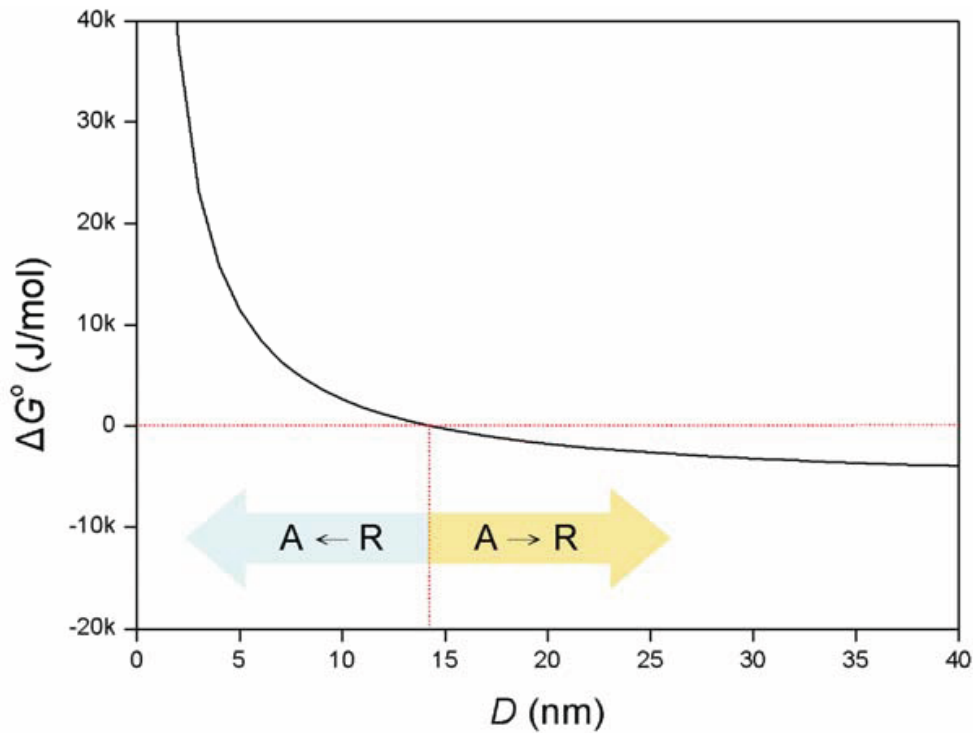
Figure 2-10 Variation of the free energy difference between nanocrystalline rutile and anatase with particle diameter at 300 K.

2.3.2.2 Titanium nitride emitter

The color of TiN coatings is important for decorative applications and is also an indication for other properties, such as hardness and resistivity [66-68]. In general, TiN in gold color has a dense structure with superior properties of hardness and resistivity compared to brown colored TiN. Figure 2-11 shows cross-sectional images of TiN coatings observed by FESEM. Both gold and brown coatings are columnar in structure but the wider column widths of brown coatings (200–230 and 280–320 nm) point out the denser structure of gold TiN (160–170 nm). The column width and the surface roughness are found to increase with the darkness of the color. TEM micrographs of TiN coatings in Fig.2-12 also tell that gold TiN has a densely packed structure with the grain size of about 50 nm [Fig. 2-12(a)], while brown TiN is open and porous in structure. Grain sizes of brown TiN increase from 100 to 200 nm

[Figs. 2-12 (b) and (c)]. The low hardness and elastic modulus values of brown TiN can be explained by the microstructure of coatings. Fig. 2-11 indicates the rougher surface of the brown TiN than the gold TiN.

TiN with gold color is high in both thermal conductivity and melting point (2950 °C) [71], stable in electron emission but low in work function (3.7 eV) [72]. TiN emitters have been successfully used to fabricate TiN-coated Si field emission arrays by sputtering system [73].
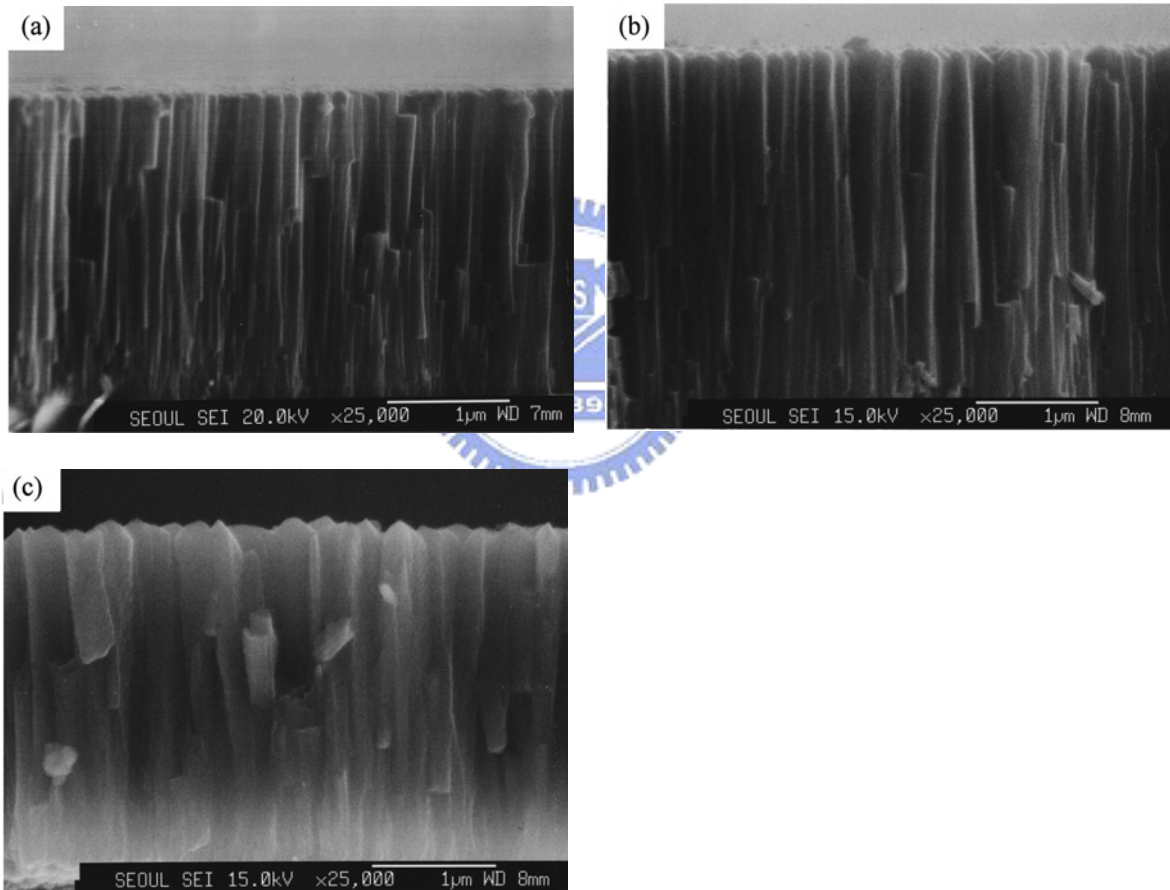
Figure 2-11 Cross-sectional FESEM images of different colored coatings. (a) gold, (b) light brown and (c) dark brown [69]
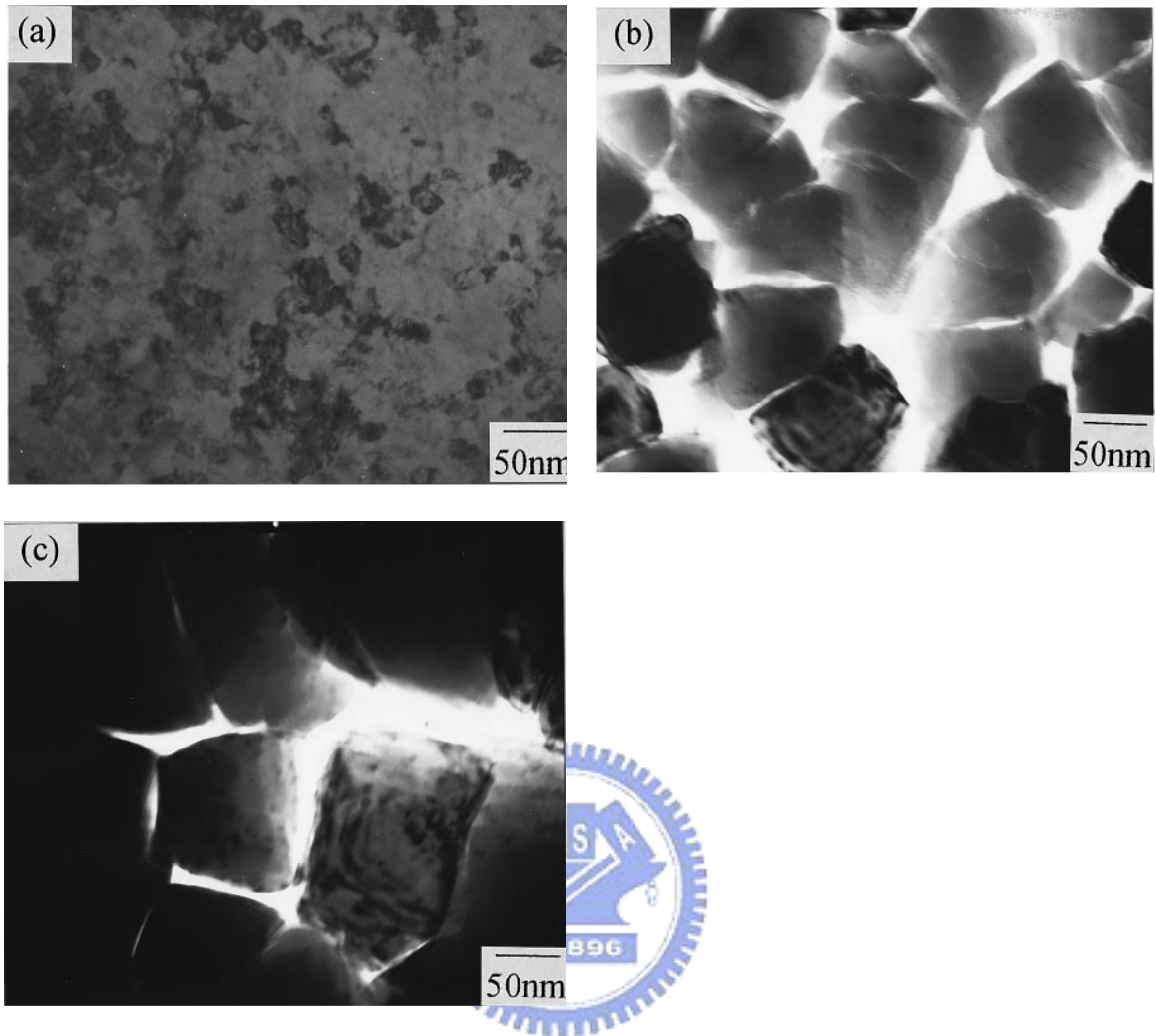
Figure 2-12 Plan-view TEM images of different colored coatings. (a) gold, (b) light brown and (c) dark brown [69].

2.3.3 Carbon base emitter

In order to stabilize and enhance the emission behavior, surface treatment with Si tip coating by diamond or diamond-like carbon (DLC) as shown in Fig 2-13 has been intensely investigated [74-81]. Diamond thin film is a suitable material for field emitter arrays. Owing to its unique material properties, such as negative electron affinity, high thermal conductivity, hardness and chemical inertness, diamond coated field emitter arrays can be operated at reduced field to produce more stable and higher emission current. High vacuum for reliable

operation is no longer unnecessary. Diamond is a wide band gap semiconductor with a gap of 5.5 eV. Since grain boundaries in CVD diamond are mainly *sp3* bonded, the work function of the crystal structure shown in Fig 2-14 [82, 83] is close to 4.7 eV of graphite. DLC with a similar local bonding configuration to the diamond surface should also have a relatively low electron affinity. DLC is amorphous carbon (*a*-C) or hydrogenated amorphous carbon (*a*-C:H) with a fraction of *sp2* and *sp3* bondings, as shown in Fig. 2-15 [84]. It is a semiconductor with a band gap which can be varied from 1 to nearly 4 eV according to the fraction of *sp3* bonding [85].

Both diamond and diamond-like carbon (DLC) films have been grown on flat substrates and sharpened silicon tip arrays [86, 87]. Although low turn-on field for electron emission has been achieved, emission from a flat surface is nonuniform due to the lack of control on emission sites. Sharpened emitter arrays are under higher control on emission sites due to the field enhancement at tips [88]. Nucleation of diamond on delicate emitter tips cannot be achieved with conventional diamond paste abrasion. Bias enhanced nucleation does not provide the desired nucleation density for a thin uniform coating on emitter tip arrays. Generally, a thick diamond coating is required to coat the emitter array uniformly and to reduce the sharpness of the tip and to block the electron transport to the surface [89]. Though thin DLC coating is available, its emission is not stable and tends to decay rapidly with time [90.] Field emission from hydrogen-free DLC films was found to be more stable than from hydrogenated DLC materials [91-93]. Emission was also found to improve with increasing nitrogen content in a-C:H film [94, 95].

EHT-20.29 kV   WD- 11 mm   Mag- 29.02 K X
100nm ├─┤   Photo No.-17 Detector= SE1
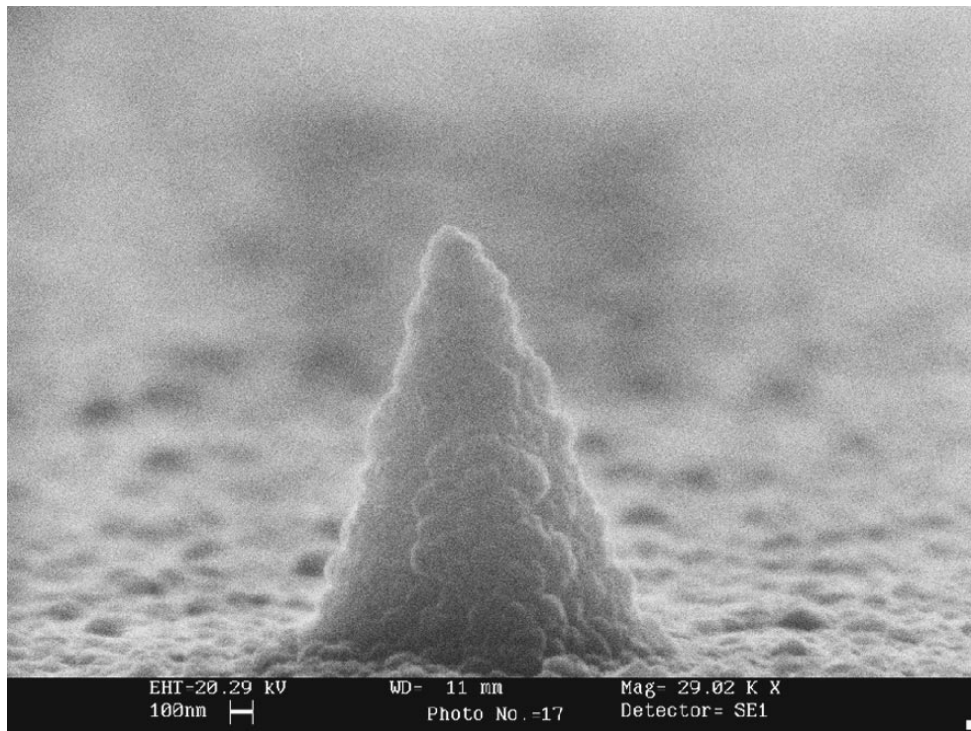
Figure 2-13 Diamond coated field emitter tip. The scale bar is 100 nm [74].
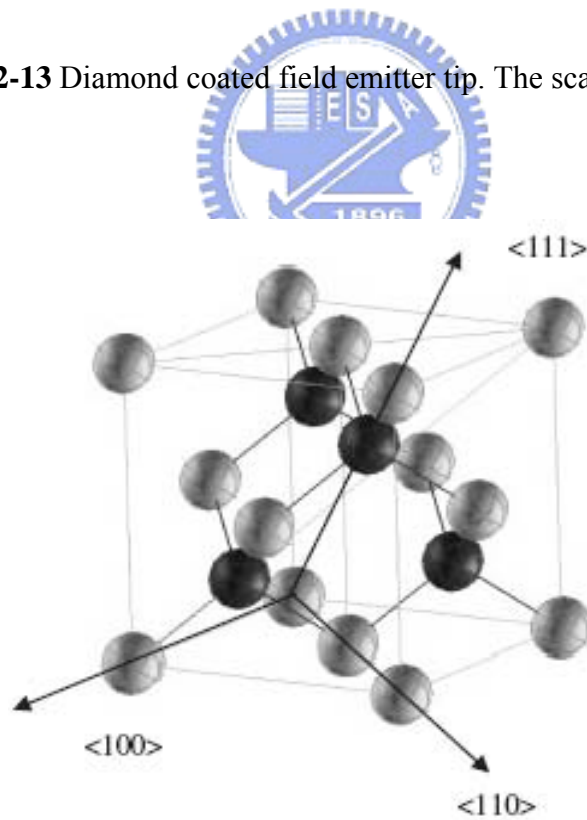
Figure 2-14 The Diamond structure of spheres [83]**.**
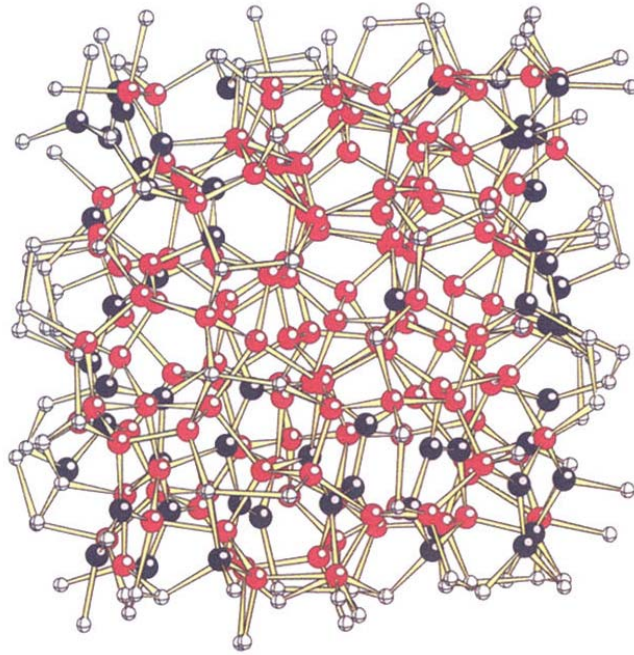
Figure 2-15 The diamondlike a-C mixture of sp3 and sp2 bonds. Different colors represent different coordinations for atomic sites (threeford: black; fordfold: red) [84].

2.3.4 Iridium dioxide emitter

Iridium oxides show considerable potential for many applications such as electrochromic display [96], electrocatalytic water oxidation anode [97], pH sensors [98] and field emission [99, 100] etc. Approaches under development to fabricate iridium oxides include anodic electrodeposition by Yamanaka [101] and Petit [102], spray pyrolysis by Kawar [103], thermal preparation by Chalamala [99], reactive sputtering by Liao [104] and metal-organic chemical vapour deposition by Chen [105]. IrO_2 film is reported to be thermally stable to maintain its phase up to 600^0C under ambient oxygen at atmospheric pressure [106] and is a conductive oxide with a bulk resistivity of about $39\mu\Omega\cdot$cm [107]. Its crystal has a rutile structure shown in Fig.2-16. Such metal oxides as IrO2 with comparable conductivities to metal Ir can be applied as an alternative choice for emitter materials. Stable oxides can minimize oxygen effects while metals like Mo are susceptible to oxidation and lead to unexpected current degradation [99].
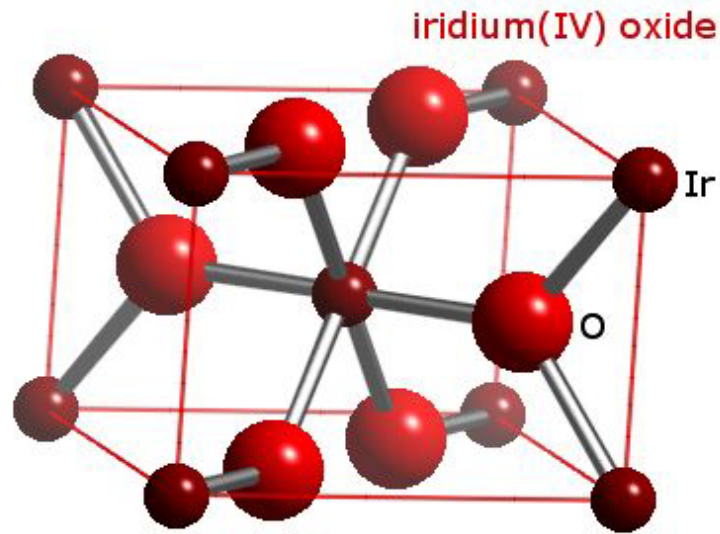
Figure 2-16 Iridium(IV) oxide tetragonal rutile structure [108].

Chen and coworkers [100] grew IrO_2 nanorods on titanium coated Si [100] substrates by metalorganic chemical vapor deposition (MOCVD) with (Methylcyclopentadienyl) (1,5-cyclooctadiene) as Iridium sources and deposited the vertical alignment of IrO_2 nanorods shown in Fig. 2-17. Emitter cones with higher aspect ratio usually result in the operational voltage reduction due to the improved field enhancement. Figure 2-18 is the TEM micrograph focused on the tip of IrO_2 nanorods and reveals that the size of tip end (*r*) with high aspect ratio is about 2–4 nmt. The inset in Fig. 2-18 confirms the formation of IrO_2 tetragonal rutile structure in these rod-like crystals. Chalamala and co-workers have demonstrated the potential of IrO_2 as an emitter material or as a protective coating on field emitter arrays made with metals against oxygen containing gases [99]. Their results also show that the formation of conductive IrO_2 from the Ir film by thermal oxidation results in a reduced surface work function.
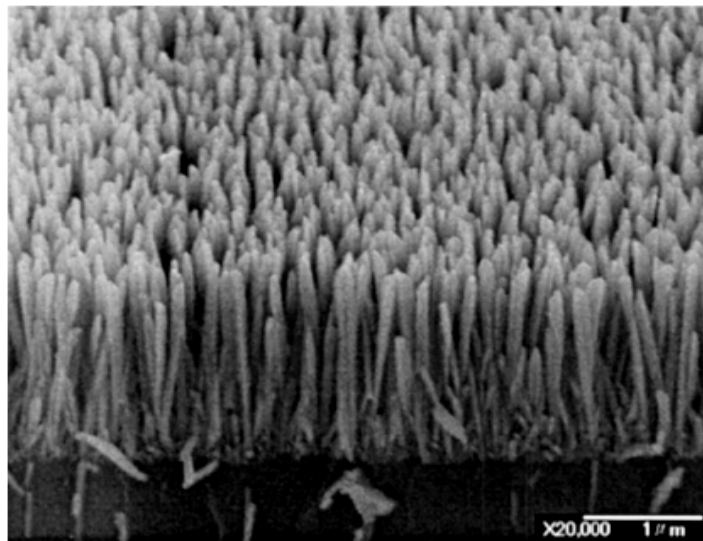
Figure 2-17 FESEM image of the vertically aligned IrO$_2$ nanorods grown on Ti-coated Si [100] substrate [100].
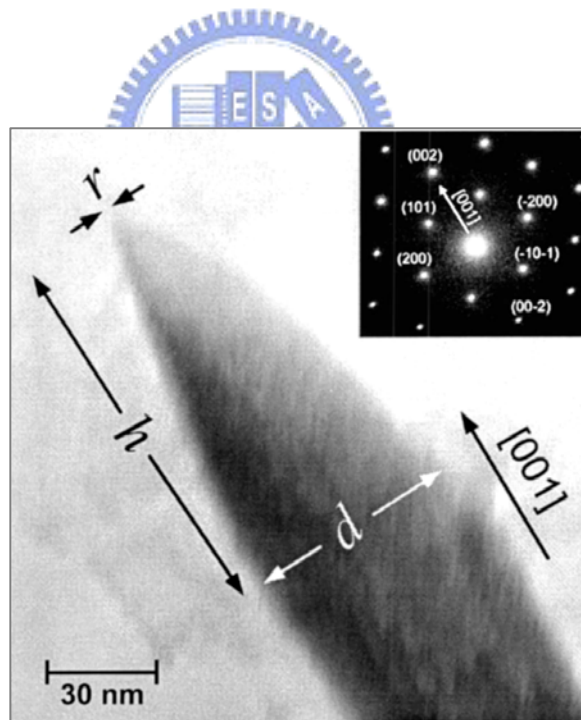
Figure 2-18 TEM image focused on the frond end of a typical IrO$_2$ nanorod with nanosized sharp tip. The inset shows the electron diffraction pattern taken along the [010] zone axis for IrO$_2$ nanorod with crystalline quality and preferred *c*-axis growth direction [100].

Figure 2-19 shows the current–voltage characteristics of Ir field emitter tips before and after *in situ* thermal oxidation. Several IrO$_2$ tips were operated under ultrahigh vacuum for extended periods of time. After 50 h of operation under a continuously applied field at a pressure of 5×10^{-9} Torr, IrO$_2$ tips showed very little degradation, as shown in Fig 2-20.
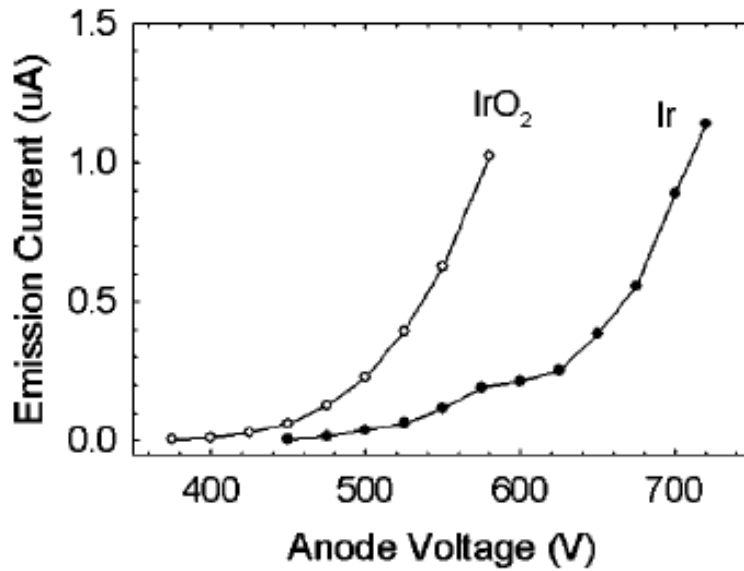
Figure 2-19 Current–voltage characteristics of Ir field emitter tips before and after *in situ* thermal oxidation [99].
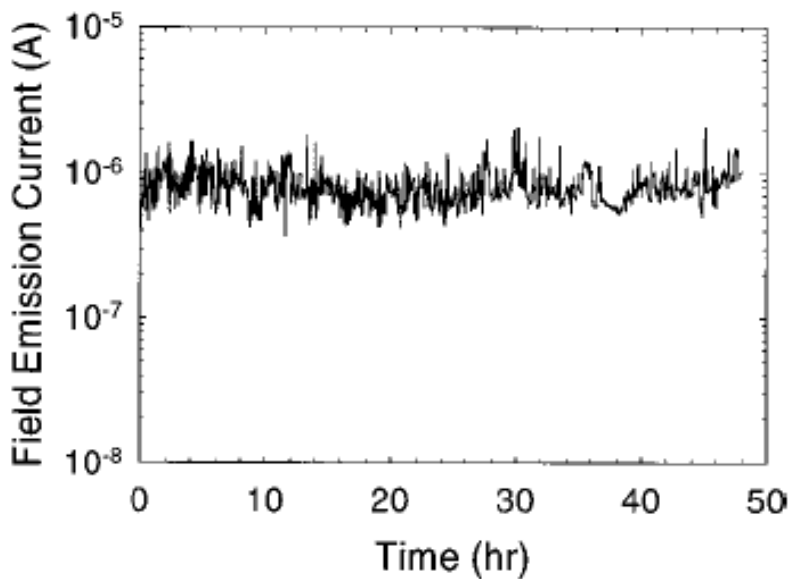
Figure 2-20 Emission current stability of IrO2 tips under ultrahigh vacuum. The tip was operated at an anode voltage of 580 V [99].

2.4 Electrochemical deposition principle

In general, for any growth process the growth mechanism and the structure of the deposited film are determined by the relative rates of the particle flux and the surface diffusion. Three different growth modes can be identified as layer growth (Frank–van der Merwe growth), island growth (Volmer–Weber growth) and mixed growth (Stranski–Krastanov growth), as shown in Fig. 2-21. In many cases, deposition of metals onto semiconductors follows island formation mechanism of growth due to the weak interaction energy between the adsorbed metal atom and the semiconductor. The relative deposition rates on substrates and deposits determine the morphology of deposits.
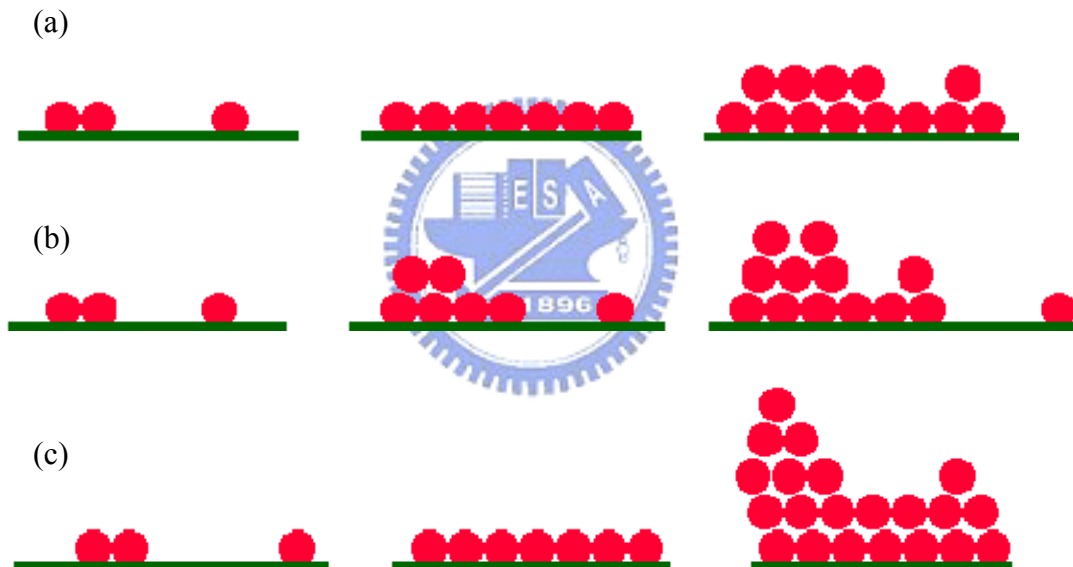
Figure 2-21 Cross-section views of the three primary modes of thin film growth including (a) layer growth (Frank–van der Merwe growth), (b) island growth (Volmer–Weber growth) and (c) mixed growth (Stranski–Krastanov growth) [109].

2.4.1. Mechanisms of nucleation and growth

Models for electrochemical deposition onto an external substrate usually assume that nucleation occurs at certain specific sites on the surface [110, 111] and the nucleation

mechanism is generally described in terms of either of instantaneous or progressive nucleation. If the rate of nucleation is fast in comparison with the subsequent rate of growth, nuclei are formed at all possible growth sites within very short time and nucleation is considered instantaneous. Conversely, if the rate of nucleation is slow, nucleation will continue to occur at the surface while other clusters are growing and nucleation is considered progressive. For the simple case of first-order nucleation kinetics, the number of nuclei increases linearly with time.

2.4.2 The potential dependence of nucleation

For 3D island growth, electrochemical deposition of metals onto either semiconductor or metal surfaces proceeds through nucleation of metal clusters and subsequent growth of films [112]. In both cases, the formation of thermodynamically stable nuclei occurs in the supersaturation regime. For electrochemical nucleation, the supersaturation can be described in terms of the difference between the electrochemical potentials of the solid metal, $\mu_{M(s)}$, and the dissolved metal ions in solution, $\mu_M{}^{n+}{}_{(aq)}$. Experimentally, $\triangle\mu$ can be directly controlled by the applied potential and the following relation holds:

$$\Delta\mu = \mu_{M(S)} - \mu_M{}^{n+}{}_{(aq)} = -ze\left|\eta\right| \tag{2.16}$$

where z is the number of charges involved in the electrochemical process and $\left|\eta\right|$ is the absolute overpotential. Note that η is negative for (overpotential) metal deposition. For semiconductor electrodes, the term overpotential is generally not available since the applied potential is partitioned across the space charge layer and the Helmholtz layer. In general, a nucleus needs to attain a critical size so that further growth is energetically more favorable than dissolution. The Gibbs free energy for the formation of a cluster of N atoms, $\triangle G(N)$ is

given by

$$\Delta G(N) = N\Delta\mu + \Phi(N) \tag{2.17}$$

where $\Phi(N)$ is the excess energy term associated with the formation of new interfaces and depends on the surface energies of the substrate and the cluster. $\Phi(N)$ may also contain terms associated with internal strain due to the lattice mismatch between the substrate and the cluster. Both terms in Eq. 2.17 are functions of the number of atoms in the cluster. For small clusters, $\Phi(N)$ usually dominates and, as a consequence, $\Delta G(N)$ increases with increasing N. The formation of a cluster can, therefore, only take place through thermal fluctuations. As the cluster size increases, $N\Delta\mu$ dominates so that the slope of the $\Delta G(N)$ versus N curve becomes negative and the cluster will grow spontaneously. The critical cluster size, N_{crit}, is defined such that d$\Delta G(N)$/dN=0. Assuming that $\Phi(N)$ is determined by the surface energy terms and considering an rbitrary three-dimensional geometrical form, Eq. 2.17 can be differentiated with respect to N. The overpotential dependence of the critical cluster size, N_{crit}, for a single-electron-transfer deposition process is given by the following relation [112]:

$$N_{crit} = \frac{8BV_m^2\sigma^3}{27(e|\eta|)^3} \tag{2.18}$$

where B is a geometrical factor (36π for a sphere, σ^3 for a cube), V_m is the atomic volume and σ is the average specific surface energy. The associated critical energy for growth of a nucleus, ΔG_{crit}, is given by

$$\Delta G_{crit} = \frac{4BV_m^2\sigma^3}{27(e|\eta|)^2} \tag{2.19}$$

Various experimental studies have been engaged to determine the size of the critical

nucleus for the deposition of metals onto metals [113–116] and for the deposition of a few metals onto semiconductors [117,118].

2.4.3 The time dependence of nucleation and growth

The nucleation mechanism and its rate are usually determined by current transient techniques. Upon applying a potential step from an initial potential at which the rate of nucleation is negligible to a fixed overpotential, the formation of stable nuclei and their growth can be observed directly by monitoring the current [119]. From the shape of the resulting transient current, nucleation rate, nucleiand density and growth mechanism can be obtained.

In general, nucleation of a metal on an external substrate is assumed to take place at active sites on the surface, such as steps, kinks or other surface defects. The density of active sites, N_0, represents the total number of possible sites for nucleation and may be potential dependent. The density of nuclei as a function of time, N(t), is usually described in terms of a linear growth law with a nucleation rate constant, A:

$$N(t) = N_\infty \left[1 - \exp(-At) \right] \qquad (2.20)$$

where N_∞ is the final density of nuclei (the total density of utilized active sites) under the experiment conditions. From these definitions, $N_\infty \leq N_0$ at any given potential. From Eq. 2.20 two limiting cases can be identified. If A is large and At $>>1$ in short period, N(t) equals N_∞ immediately after the pulse. Conversely, if A is small and $At <<1$ in short period, N(t) equals $AN_\infty t$ and the density of nuclei increases linearly with time. These two cases correspond to instantaneous nucleation and progressive nucleation, respectively.

The growth of nuclei can be kinetically limited, diffusion limited or under mixed control.

In many cases, the overpotential used for nucleation and growth is relatively large, so that diffusion of metal ions to the surface is often rate limiting [120-127]. In very short period, growth may be kinetically limited due to the large diffusion flux to small nuclei [128]. As the growth becomes diffusion limited, the diffusion zones around individual nuclei will start to overlap and linear diffusion to the surface may occur before nuclei impinge on each other. If the nucleation is progressive, the development of diffusion fields may block active sites for nucleation and result in the situation of $N_\infty < N_0$. In addition to the potential dependence of N_0, N_∞ is likely to be a function of the potential. In general, the density of nuclei increases with increasing overpotential due to the consequence of these two effects.

2.4.4 Deposition of continuous films onto semiconductor

The deposition of continuous metal films onto semiconductor surfaces can follow the 3D island growth mechanism. In order to obtain a continuous film, the density of nuclei must be high enough for islands to coalesce during further deposition of the metal. If the growth process is diffusion limited, however, any instability will lead to rough morphologies. Hence, deposition of a continuous metal film requires a high density of nuclei followed by the growth under kinetic or mixed control. For the deposition of continuous metal films onto n-type semiconductors, the electron transfer step may be faster at metal nuclei and further film growth may be expected to occur preferentially at pre-existing metal islands. For the deposition of continuous films onto p-type semiconductors through charge transfer via the conduction band, a high intensity of light may be required to obtain a sufficiently high surface electron density both for the nucleation and for growth processes. Note that deposition of thicker films onto p-type surfaces under illumination is complicated by the reflection from the deposited metal layer. As a result, strategies for the deposition of continuous metal films onto semiconductor surfaces generally include an initial potential step involving the formation of a

high density of nuclei, followed by growth at low overpotential under such conditions that the flux of metal ions to the surface is not rate limiting.

2.4.5 Deposition of metals onto semiconductor/metal films

During deposition of metals onto semiconductor surfaces under conditions where the density of nuclei is sufficiently high, coalescence of the nuclei will result in the formation of a continuous film. In this case the semiconductor is isolated from the solution and subsequent growth is dependent on the properties of the metal film and the potential distribution across the interfaces. Figure 2-22 (a) illustrates the steps involved in electrochemical deposition of a metal onto the semiconductor surface. Initially a metal ion reaches the surface and accepts electrons from the semiconductor. Adsorbed metal atoms then diffuse along the surface before incorporated into a nucleus. Figure 2-22 (b) shows the steps involved for deposition of a metal onto an existing continuous metal film. In this case, energetics and kinetics of the deposition reaction are different because the semiconductor surface is no longer involved in the process. As soon as metal nuclei are deposited onto a semiconductor surface, energetics and kinetics of the system may change dramatically, depending on the nature of the semiconductor/metal contact. For example, if the surface coverage of the metal on the semiconductor is low, the band bending may be spatially inhomogeneous [130,131]. If the semiconductor/metal film results in the formation of a Schottky barrier, electrochemical stripping of the metal layer from an n-type semiconductor is not possible since electrons in the metal film have to be excited to the conduction band for dissolution to occur. In the case of deposition of metals onto p-type semiconductors, a stripping peak is usually observed due to the transfer of valence band holes, which are the majority carriers, to the metal at sufficiently positive potentials [132]. In addition to these energetic considerations, kinetics of reactions at metal islands and semiconductor surfaces usually differ considerably, and lead to a spatial dependence of rates

of reaction at surfaces covered with metal nuclei. The above discussion may conclude that energetics and kinetics of redox reactions at metallized semiconductor surfaces are very complicated [133,134] and the presence of two interfaces has important consequences. Under equilibrium conditions, Fermi energies of the semiconductor, metal and redox couple in the solution are the same. The metal layer is not directly connected to the external circuit and, consequently, upon applying a potential the Fermi level of the metal layer can remain aligned with that of the semiconductor or with that of the redox couple, or it can be at some intermediate position. Kinetically, this can be viewed as being dependent on the rates of charge transfer between either the solution and the metal or the semiconductor and the metal.
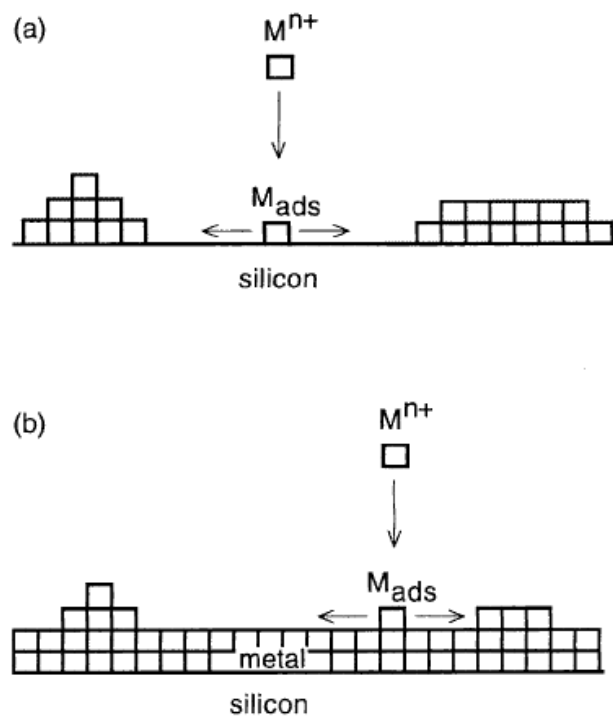
Figure 2-22 Schematic illustrations showing (a) the initial stages of Volmer–Weber growth of a metal on silicon and (b) deposition of a metal onto silicon at later stages when a continuous metal film is deposited [129].

Chapter 3 Experiment Methods

3.1 Introduction

Fig. 3-1 illustrates the experiment flowchart of fabrications and analyses of anodic aluminum oxide (AAO) template assisted arrays of TiN nanorods, Si nanotip coated α-carbons and Si nanotip coated IrO_2 arrays. Arrows of different colors stand for different experiment purposes. Anodic oxidation of Al films can yield highly ordered pore channels. Partial anodic oxidization may take place for underlying TiN films when the Al anodization was completed and thereby form TiO_x nanopillars under the bottom of AAO pore channels. The microstructure of TiO_x nanopillars was studied by scanning electron microscopy (SEM). TiO_x nanodots were then used as nanomasks to etch the TiN layer and the underlying Si substrate in an inductively coupled plasma reactive ion etch (ICP-RIE) system. Field emitter microstructure, bonding structure and chemical composition were analyzed by SEM, transition electron microscopy (TEM), Raman spectroscopy, Auger electron spectroscopy (AES), X-ray photoelectron spectroscopy (XPS) and X-ray diffraction (XRD), etc. Field emission measurements (J-E) of specimens were conducted by the simple diode configuration and performed in high vacuum.

3.2 Deposition of TiN and Al films

Titanium nitride (TiN) films were deposited on a (100)-oriented p-silicon wafer in a ultrahigh vacuum reactive dc magnetron sputtering system. The titanium target used was 99.9999% pure. TiN films were prepared in a gas mixture of argon and nitrogen. During the deposition, the dc power was set at 8 kW and followed by the deposition of an Al film in 3μm thickness on the TiN layer by a high vacuum thermal evaporator with the base pressure of 5×10^{-6} Torr. Aluminum ingots with a purity of 99.999% were used as the aluminum source.

Tungsten boats were used to melt and evaporate aluminum ingots.
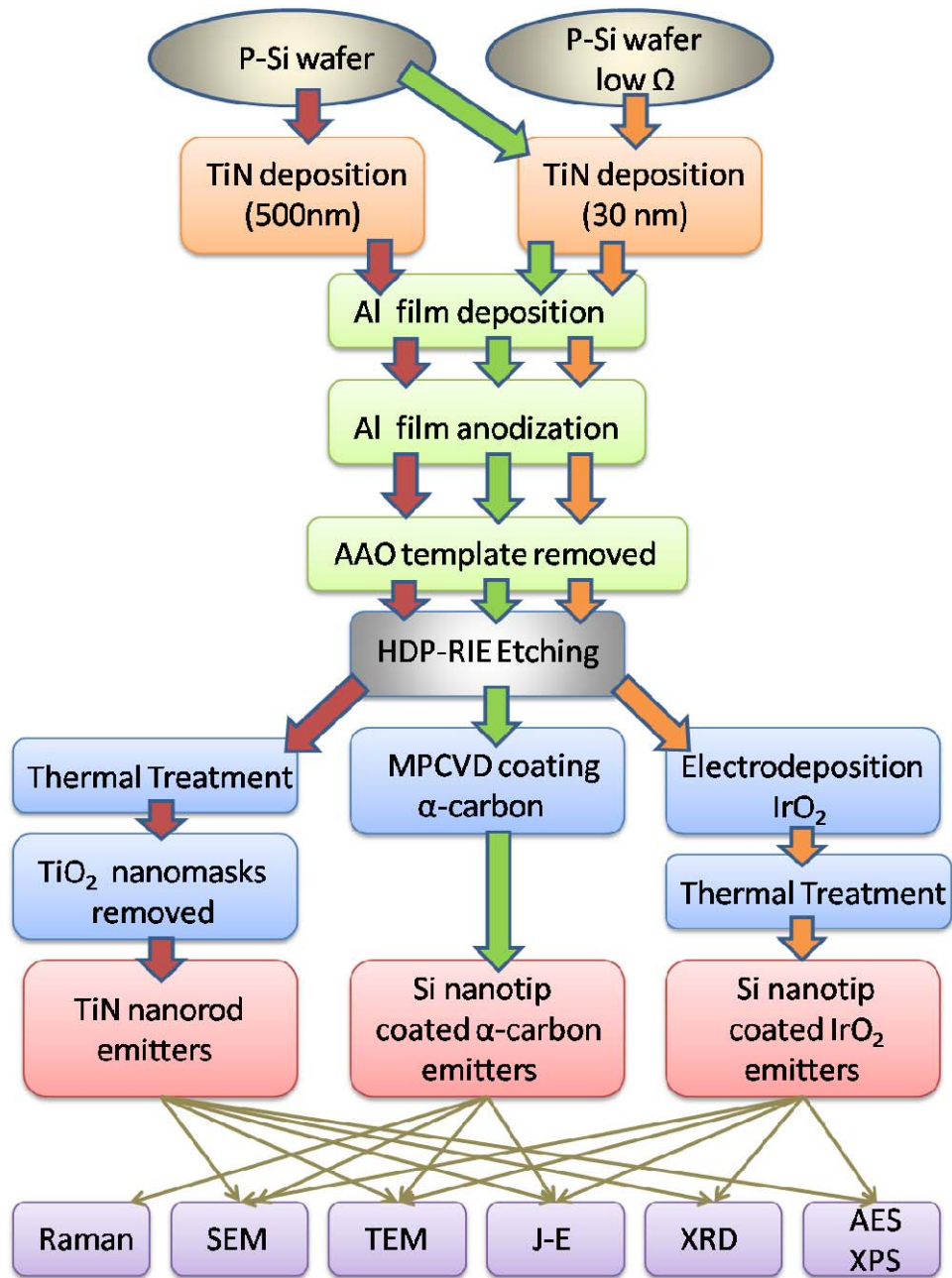
Figure 3-1 Experiment flowchart of fabrications and analyses of AAO templated TiN nanorods, Si nanotip coated α-carbon emitters and Si nanotip coated IrO$_2$ arrays.

3.3 Anodic Aluminum Oxide

The anode was the aluminum film specimen and a platinum foil was used as the cathode. The O-ring was clipped between the specimen and the tank fixed by a jig. Anodic oxidation of the Al film was carried out in 0.3M oxalic acid ($H_2C_2O_4$) at 25 ^{o}C under a constant polarization voltage of 40V. The anodic current was measured by a source -measure unit (Keithley Model 2400). Labview for GPIB interface with Keithley 2400 was employed to force voltage and measure current simultaneously. The program could also set up the anodic oxidation of Al film end current point.
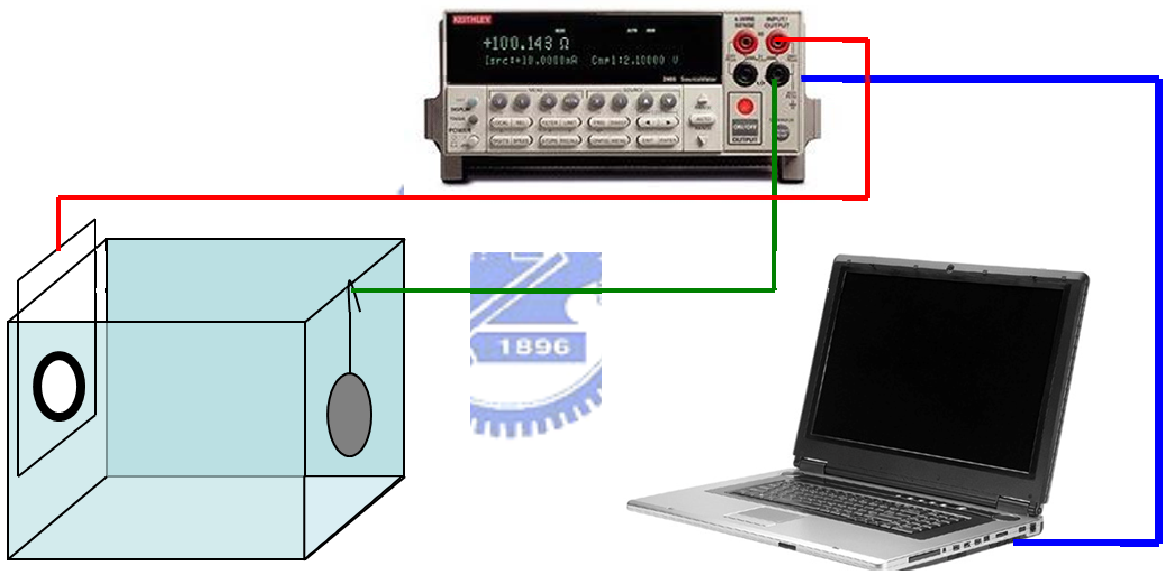
Figure 3-2 Schematic diagram of experiment setup for aluminum anodization.

3.4 Reactive Ionic Etching system

TiO$_x$ nanodots were then used as nanomasks to etch the TiN layer and the underlying Si substrate in an inductively coupled plasma reactive ion etch (ICP-RIE) system (Duratek). An inductively coupled plasma source is also called a transformer-coupled plasma source because of its similar mechanism to a transformer. The inductive coils serve just like the initial coils of

a transformer. When an RF current flows in the coils, it generates a changing magnetic field, which in turn generates a changing electric field through inductive coupling. The inductively coupled electric field accelerates electrons and initiates ionization collisions. Since the electric field is in the angular direction, electrons are accelerated in the angular direction and travel a long distance without collision with the chamber wall or electrode. This is why an ICP system can generate high-density plasma at low pressure (a few 10 mTorr). The ICP design that includes high-density plasma (HDP) dielectric CVD system, silicon, metal, and dielectric HDP etching system, native oxide sputtering clean system and ionized metal plasma PVD system is very popular in the semiconductor industry. A bias RF system is added to the ICP chamber to generate self-bias and to control ion bombardment energy. Since ion bombardment from high-density plasma generates a lot of heat, a helium back-side cooling system with E-chuck is required for better wafer temperature control. In the ICP system, ion flux, manly determined by the plasma density, is controlled by the source RF power and ion bombardment energy is controlled by the bias RF power.
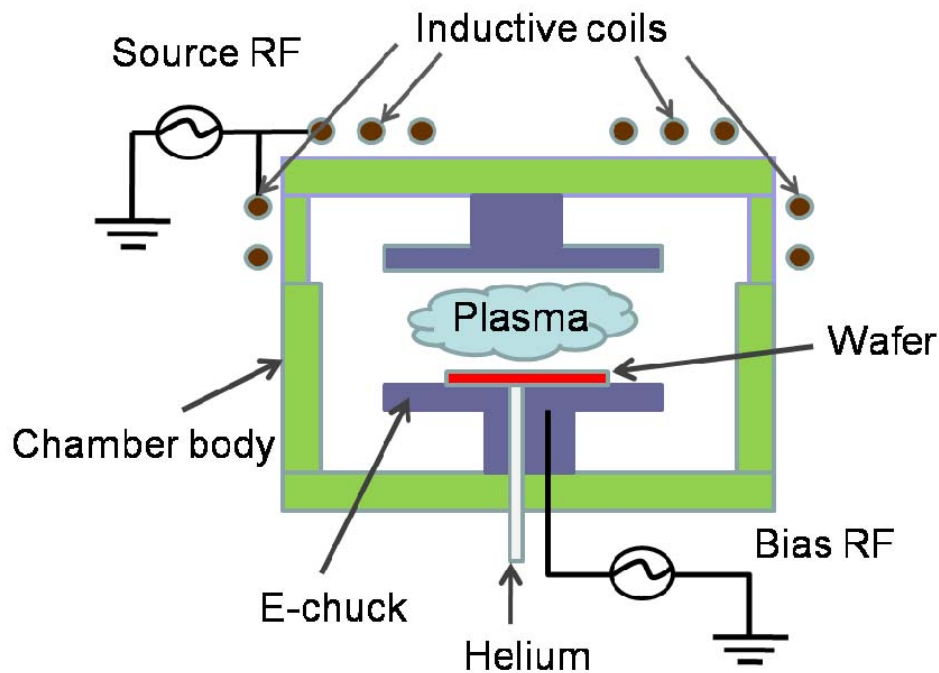
Figure 3-3 schematic of ICP chamber

3.5 Microwave Plasma Chemical Vapor Deposition system

Fabrication of α-C coated Si nanotips was then carried out in a microwave plasma CVD (MPCVD) system. Fig.3-4 schematically depicts the layout of the MPCVD system. A quartz tube is vertically attached to a rectangular waveguide used as deposition chamber. The microwave from a magnetron source (model IMG 2502-S, IDX Tokyo, Japan) is supplied to the quartz tube through an isolator and a power meter. Then the microwave power is coupled to the quartz tube through an aluminum waveguide with a hole drilled through from top to bottom face. Aluminum tubes extend out from both holes. Tube extensions are water-cooled as well. A sliding short circuit is then attached at the end of the waveguide. The lower position of the quartz tube is connected with a stainless steel multi-port chamber equipped with a rotary pump. Substrates are positioned in the middle of the quartz tube waveguide intersection and held vertically by a substrate holder of 20mm in diameter and made of molybdenum.
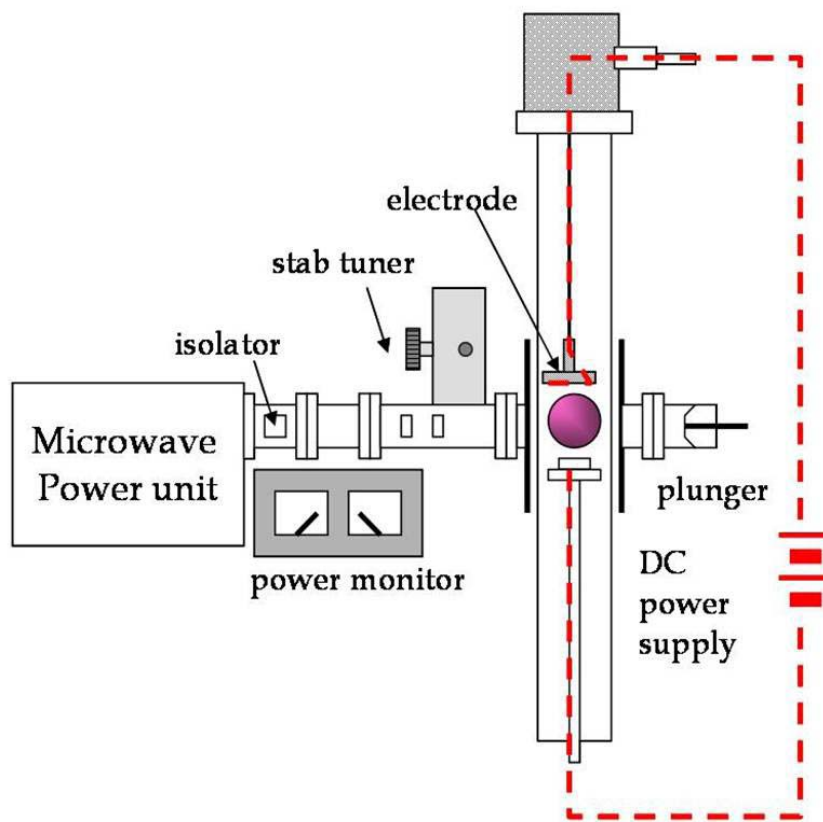
Figure 3-4 Schematic diagram of the bias assisted microwave plasma chemical vapor deposition system.

3.6 Electrochemical deposition

Electrochemical deposition of IrO_2 nanaoparticles on Si nanotips were performed by bipolar galvanostatic pulse electrodeposition in a three electrode cell system (Jiehan 5000 Electrochemical Workstation) with Si nanotips as the working electrode, a thin platinum plate as the counter electrode and the saturated calomel electrode (SCE) as reference electrode. The electrodeposition solution was an aqueous solution of $IrCl_4 \cdot H_2O$ (0.3 g in 200 ml H_2O), oxalic acid $H_2C_2O_4 \cdot 2H_2O$ (1g) and H_2O_2 (2 ml). The pH of the solution was adjusted to ~10.5 by the addition of K_2CO_3 [20]. Before the electrodeposition onto Si nanotips, the solution was aged for two days.
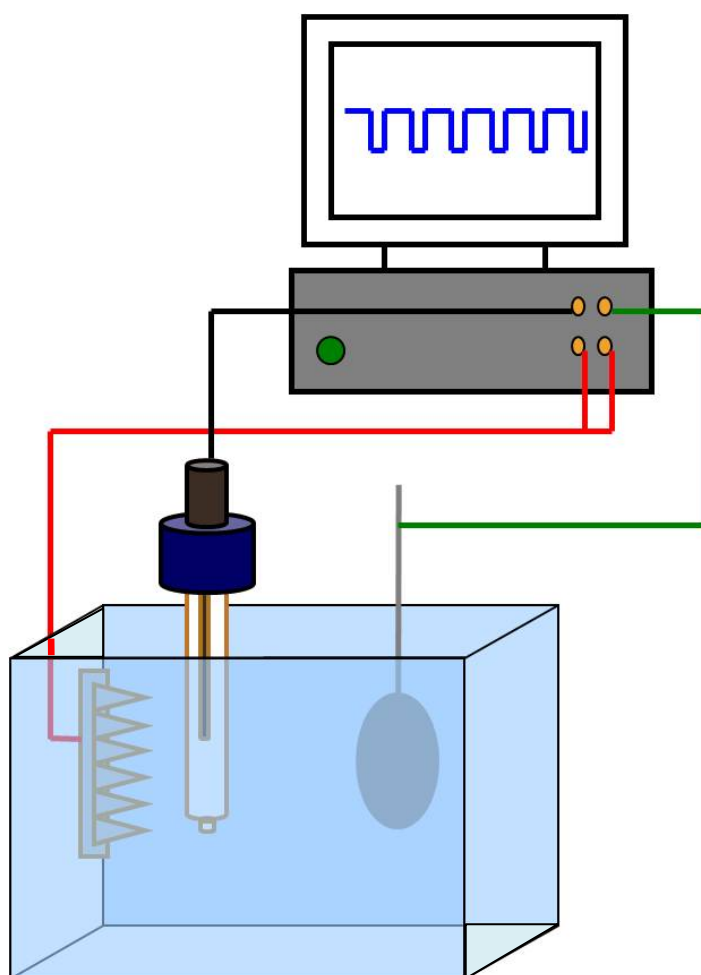
Figure 3-5 Schematic diagram of the electrochemical deposition setup.

3.7 Material analysis methods

3.7.1 Raman spectroscopy:

While photons illuminate molecules or crystals, reaction between photons and atoms is always accompanied with momentum change or energy exchange. By collecting the scatter photons, sequence of spectrum, including Raman scattering (inelastic scattering) and Reyleigh scattering (elastic scattering) can be obtained. Photons of Raman scattering can be classified into two kinds, the Stoke side where photons loss energy or molecules gain energy and the anti-Stoke side where photons gain energy or molecules loss energy. Stoke side is generally used to characterize the material. As Raman spectrum provides the information of crystallinity and bonding, it has become the most direct and convenient way to identify carbon related materials. The Raman spectrum peak of sp^3 and sp^2 bonds in crystalline graphite are 1380 (D peak) and 1580 cm^{-1}(G-peak), respectively. The instrument in operation is a Renishaw Raman microscope, Model 2000. The source available is He-Ne laser with the wavelength of 632.82nm and the power of 200mW. The spectral slit width is 0.4cm^{-1}.

3.7.2 SEM

Scanning electron microscopy is used to observe the object surface morphology in wide range. It has the advantage of easy sample preparation, high image resolution, large field depth and high magnification. A common SEM is equipped with an electron gun to generate electron beams to be accelerated under 0.4-40kV voltage. By deflecting the incident beams with focusing coils, a two dimensional image can be obtained by detecting the reflected secondary electrons and the backscatter electrons.

The model mainly engaged is field emission type SEM JEOL-6500. Accelerating voltage is 15kV with current of 10μA. Working distance is 10mm under 9.63x10^{-5}Pa.

3.7.3 XRD

XRD is a useful tool to analyze the crystallography of specimen and to determine the mean particle size of particles. When X-ray radiation passes through matter, the radiation interacts with electrons in atoms and brings about scattering of the radiation. If atoms are organized in planes and atom distances are of the same magnitude as the wavelength of the X-rays, constructive and destructive interference will occur. This results in diffraction where X-rays are emitted at characteristic angles according to the atom spaces organized in crystalline structures called planes. Most crystals have many sets of planes passing through atoms. Each set of planes has a specific interplanar distance and will give rise to a characteristic angle of diffracted X-rays. The relationship among wavelength, atomic spacing (d) and angle is solved by the Bragg Equation. If the illuminating wavelengh is known and the angle can be measured, the interplanar distance can be calculated from the Bragg equation: $n\lambda = 2d\sin\theta$. A set of 'd-spaces' obtained from a single compound will represent the set of planes that can pass through atoms and can be used for comparison with sets of d-spaces obtained from standard compounds.
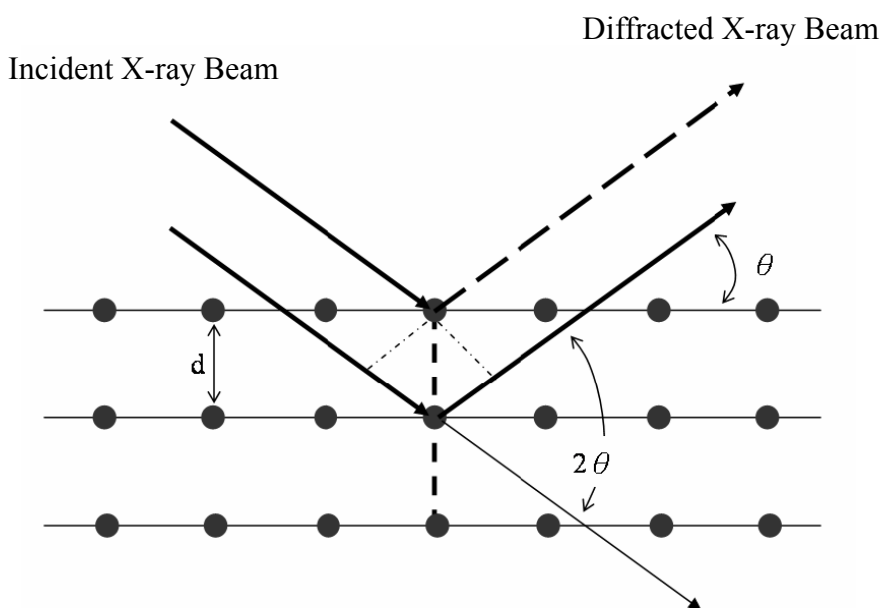
Figure 3-6 Schematic diagram of Bragg's law.

3.7.4 TEM

Transmission electron microscopy (TEM) (JEOL JEM-2010F) is operating at 200 kV accelerating voltage. This is the most important instrument to study defects in detail. Transmitted and diffracted electrons are recombined by objective lens to form a diffraction pattern in the back focal plane of that lens and a magnified image of the sample in its image plane. A number of intermediate lenses are used to project either the image or the diffraction pattern onto a fluorescent screen for observation. The screen is usually lifted and the image is formed on photographic film for recording. The image modes in TEM are shown in Fig. 3-7.

(a)

(b)
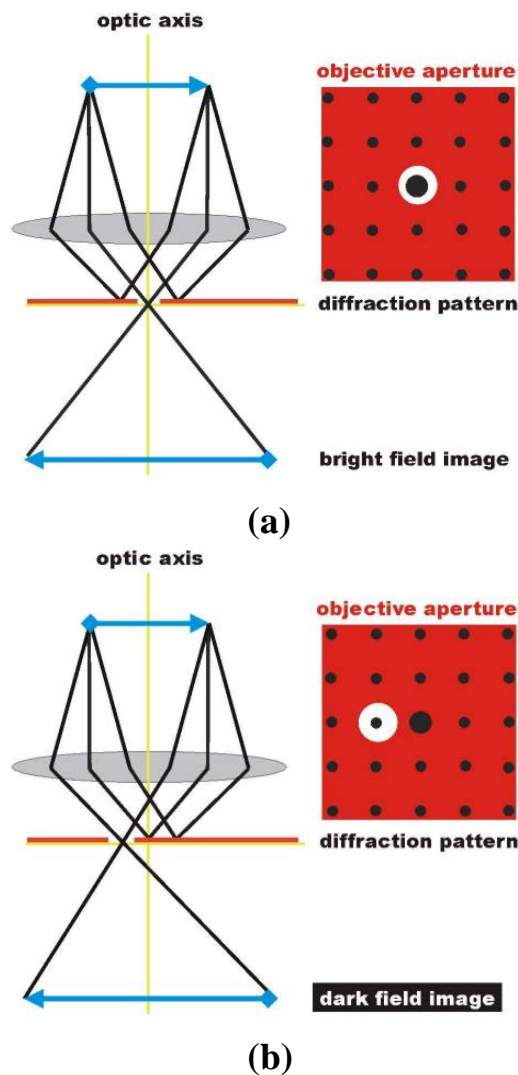
Figure 3-7 Schematic diagram of theTEM image modes (a) Brigh field image (b) Dark field image.

3.7.5 AES and XPS

AES analysis technique employs an electron beam (2-30 keV) to irradiate the specimen surface and excite Auger electrons which possess specific energy. Through assaying the kinetics energy of Auger electrons by an electron energy analyzer, the element composition and the specimen chemical state are ready to be acquired. Because incident electrons with low-energies (1-3 keV) have very short inelastic mean free paths (5-20 Å) inside the solid phase materials, AES technique is usually used to obtain the information within 50 Å from the surface. In this study, AES was employed to investigate the bonding structure of carbon nanostructures and to study the atomic composition of nanodots as a function of the time of argon ion sputtering (depth profiling). The AES analyses were performed by using a VG Microlab 310F Auger system with a Schottky field emission electron source.

Surface analysis by XPS involves irradiating a solid in vacuum with monoenergetic soft X-rays and analyzing the emitted electrons by energy. The spectrum is obtained as a plot of the number of detected electrons per energy interval versus their kinetic energy. Quantitative data can be obtained from peak heights or peak areas, and the identification of chemical states often can be made from exact measurements of peak positions and separations. In this study, XPS was used to analyze the chemical states of titanium oxide nanodots. XPS analyses were performed on a VG Microlab 310F system with Al-$K\alpha$ (1486.6 eV) excitation. X-ray emission energy was 400 W with 15 kV accelerating voltage. Argon ion with ion energy of 5 keV was used for sputter profiling.

3.8 Field emission measurement

Fig. 3-8 shows the setup of a field emission measurement facility. To ensure the precision of the gap between the cathode and the anode, spacers which are soda-lime glasses with the thickness of 150μm are directly attached onto the sample.
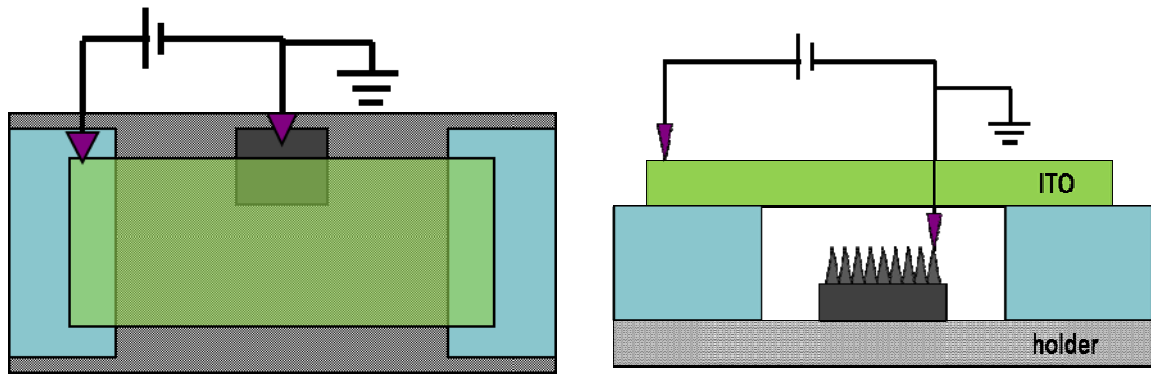
Figure 3-8 Schematic diagram of the field emission measurement setup.

The anode is an ITO conductive glass of ~1mm in thickness. The length of the field emission area is defined as the distance between the two spacers and the width is the width of the sample itself. High voltage source (Keithley-237) is connected to the anode and the cathode by physical contact. The experiment is carried out in a vacuum chamber with pressure of 1×10^{-6}Torr.

Chapter 4

Growth of self-organized TiOx nanomask arrays

4.1 Introduction

Over the past decade, there have been surges of interest in the uniform nanopore arrays of anodic aluminum oxides (AAO). AAO is particularly useful to fabricate various nanostructures for high-density sample manufacture. Since AAO is also of use to develop nanopatterns of various sizes, electron-beam lithography becomes obsolete. Oxide nanodot formations have been studied so far by using AAO template approach. Recent studies have shown that anodization under certain conditions of sputter-deposited Ta-Al[135], TaN-Al[136][137], Nb-Al[138], Si-Al[139], Ti-Al[140] and TiN-Al[141] resulted in the formation of self-organized arrays of nanostructured anodic oxides.

AAO were applied in this study as templates to prepare TiO_x nanodot arrays with hexagonally close-packed (hcp) arrangements on Si substrates. TiO_x nanodots served as masks to fabricate well ordered field emitter arrays.

4.2 Preparation of TiO_x nanomask

Figure 4-1 illustrates the technological process for the preparation of nanodot arrays of titanium oxides. Preliminary deposition of a sputtered TiN film of ~30 nm (for Si nanotip) or 500 nm (for TiN nanopillar) in thickness on the *p*-silicon (100) wafer was followed by another deposition of an aluminum film in thickness of 3 μm by thermal evaporation. The TiN film was deposited in an ultrahigh vacuum reactive dc magnetron sputtering system (MRC PRIMUS 2500TM) at a base pressure of 5×10^{-9} torr. The aluminum film was deposited in a high vacuum chamber (< 5×10-7 Torr) by using an aluminum source of 99.999% in purity. Anodization was carried out in 0.3 M oxalic acid ($H_2C_2O_4$) as electrolytes. The AAO layer

was removed by wet chemical etch in a solution of 6 wt % H_3PO_4 and 1.5wt % CrO_3 at 60^oC for 40 min.
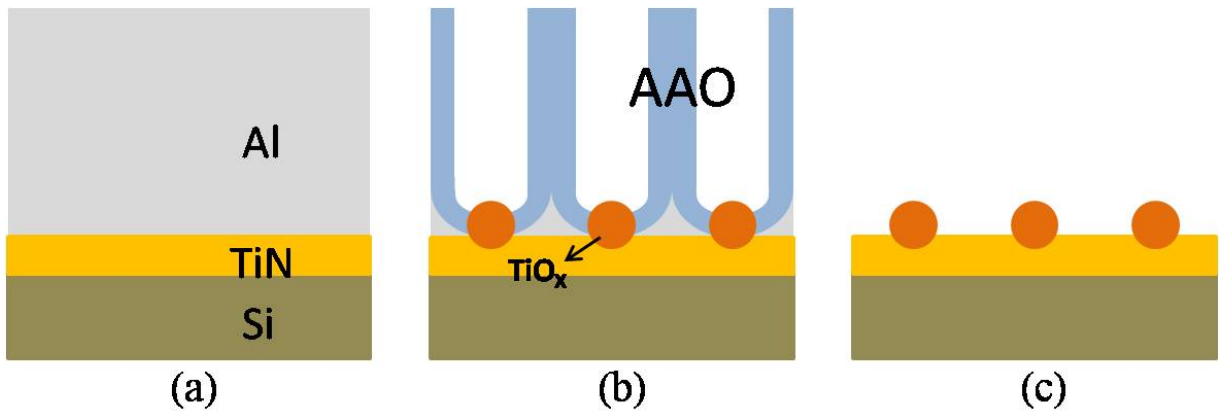
Figure 4-1 Schematic diagrams of general steps to forme titanium oxide nanodots under a porous AAO film: (a) Deposition of Al/TiN bilayered films, (b) anodic oxidation for the nanoporous AAO and TiOx nanodot formation, (c) selective removal of the overlying AAO film.

Figure 4-2 is the current-time anodization curve. The anodization behavior of the Al/TiN film stack on the silicon wafer is regarded to involve two stages. During the first stage, the upper aluminum layer was anodized to nanoporous AAO containing a scalloped hemispherical oxide barrier under each pore bottom, and the anodic current density was rather steady at about 13 mA/cm^2. In this stage, the upper aluminum layer is anodized to alumina (Al_2O_3), accompanied by simultaneous outward migration of Al^{3+} and inward diffusion of O^{2-}/OH^- ions driven by the applied electric field, leading to the vertical pore channel growth [11]. The Al_2O_3 dissolution at the Al_2O_3/electrolyte interface is in equilibrium with the Al_2O_3 growth at the Al/Al_2O_3 interface. As the downward grown pore channels reached the Al/TiN interface, the anodic current density dropped abruptly to a value$<$2.5 mA/cm^2, and the underlying TiN was oxidized by anodization as well. The anodic oxidation of TiN layer was confined in the AAO pore area and consequently led to the formation of nanodot structures with a pattern in accordance with the upper nanoporous AAO layer.
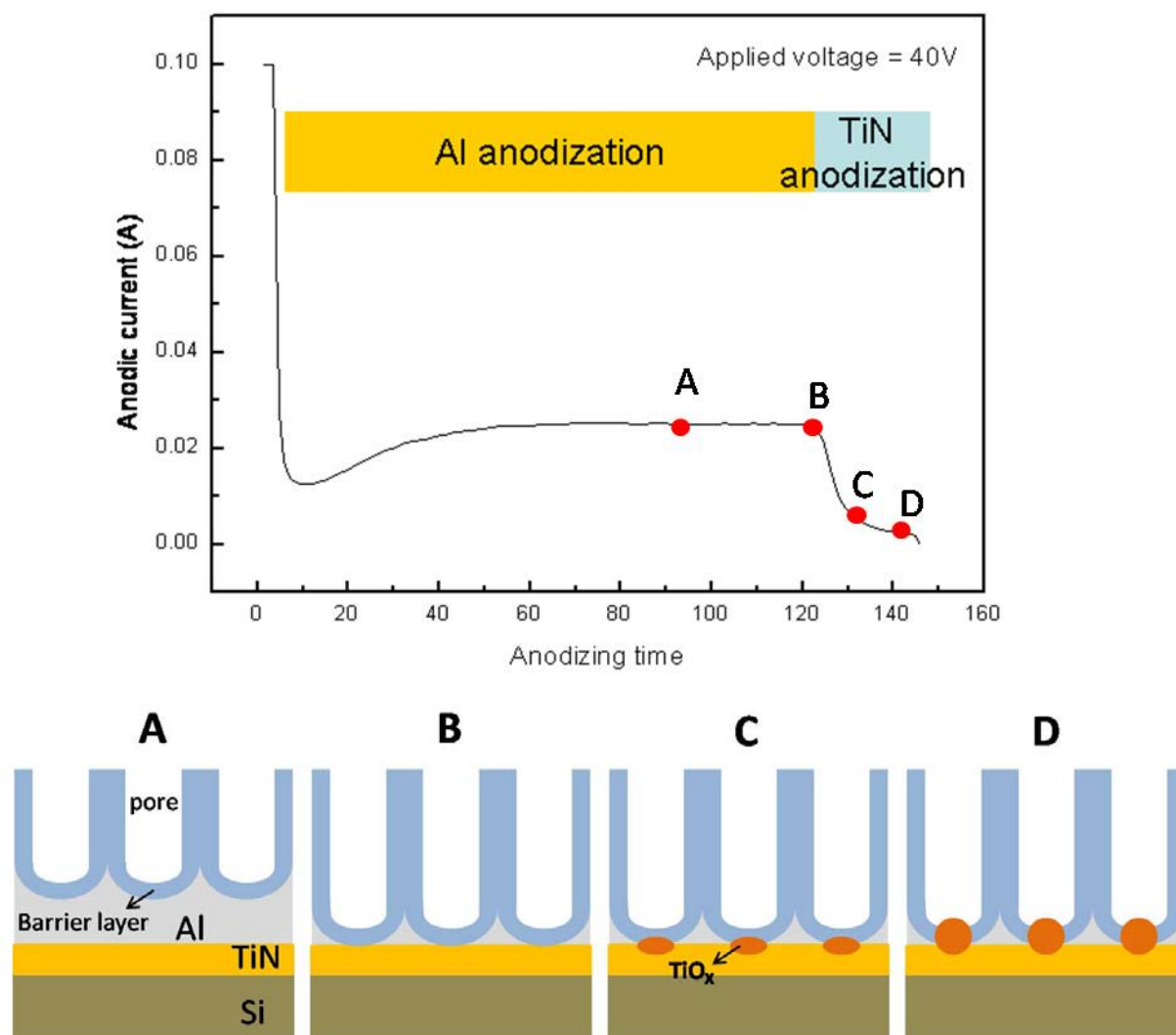
Figure 4-2 The anodic current density-anodizing time behaviors during anodizing of the Al/TiN bilayered films in 0.3 M oxalic acid electrolyte. The insets are schematic diagrams showing the anodization steps.

The anodic reaction was terminated while the exposed TiN region was fully oxidized to TiO_X. The underlying TiN can be initiated by the following anodic reaction:

$$TiN + xOH^- \rightarrow TiO_X + (1/2)N_2 + xH^+ \qquad (4\text{-}1)$$
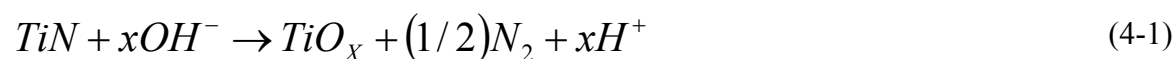
Figure 4-3(a) shows the FE-SEM images of aluminum oxide barrier layers. TiO_X nanodots with overlying porous alumina films are shown in Figure 4-3(b). Figure 4-3 (c) reveals TiO_X
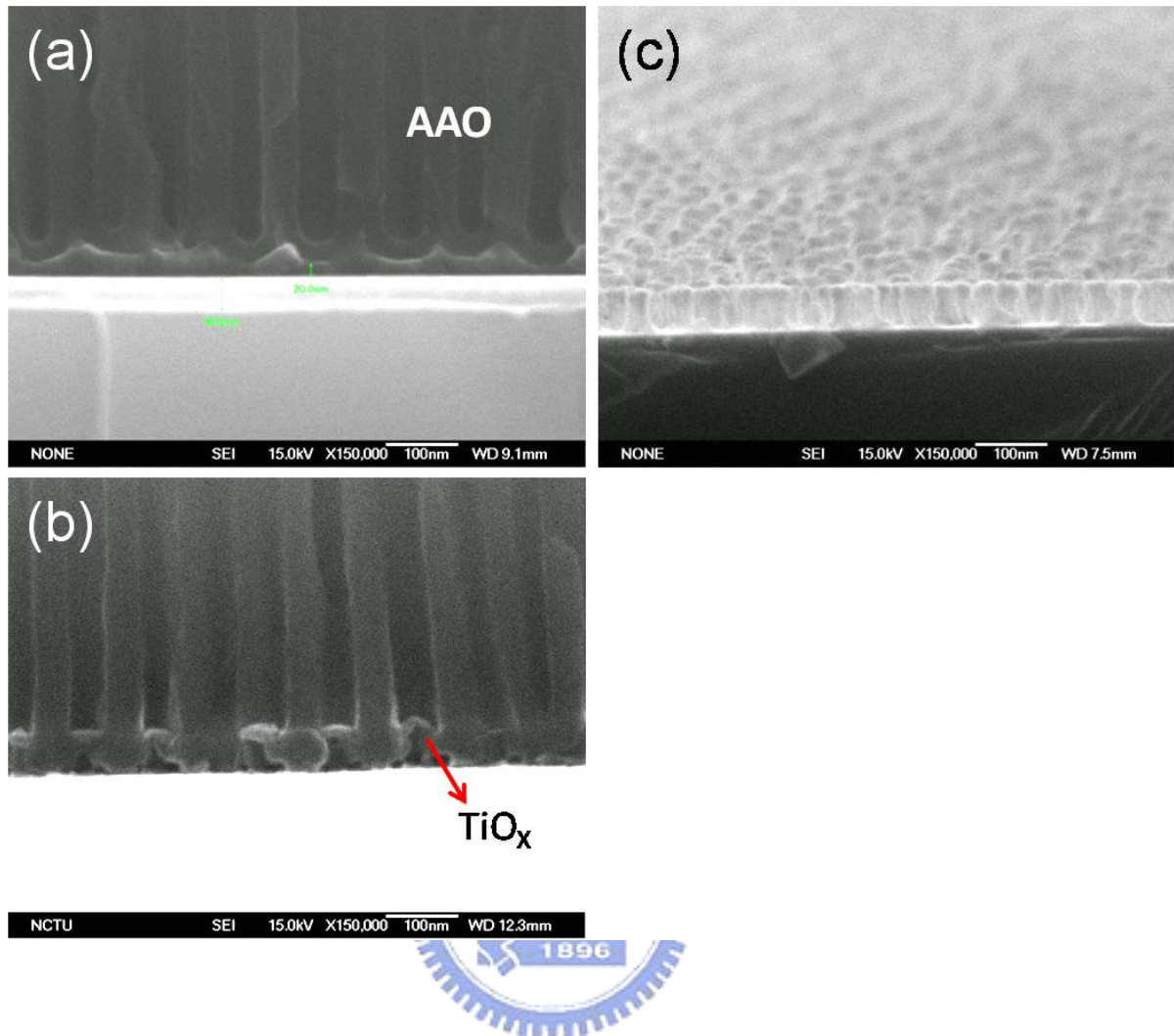
Figure 4-3 shows the cross-sectional view FE-SEM images of (a) the aluminum oxide barrier layers, (b) TiO$_X$ nanodots with overlying porous alumina films and (c) side-view view FE-SEM images of TiO$_X$ nanodot arrays.

nanodot arrays after the removal of AAO templates. Indicated in the electron spectroscopy for chemical analysis (ESCA) of Ti(2p) in Fig. 4-4 is an apparent peak at 459.4 eV of binding energy that confirms the existence of Ti^{4+}$2p_{3/2}$ bonding. Ti($2p_{3/2}$) bonding energy of TiN should appear at 455.2 eV. The 4.2 eV peak variation of the two peaks specifies bondings between partial TiN and TiOx because TiN films are oxidized to titanium oxides in the bottom of AAO during the anodization of Al layers. Anodic current density-anodizing time behaviors during the anodization of an aluminum film in a 0.3 M oxalic acid electrolyte under voltages of 20V, 30V,and 40V were shown in Figure 4-5.

48
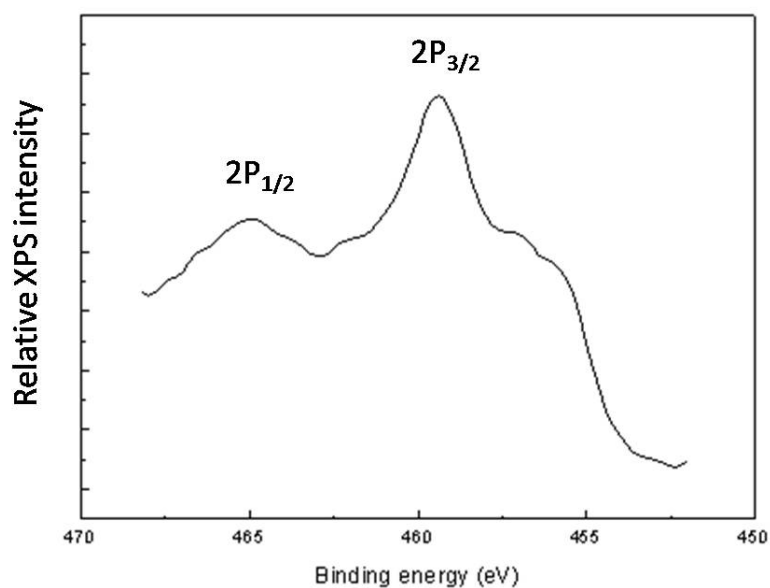
Figure 4-4 shows the XPS titanium 2*p* spectra of titanium oxide nanodot arrays after the overlying AAO template was removed by wet chemical etching.
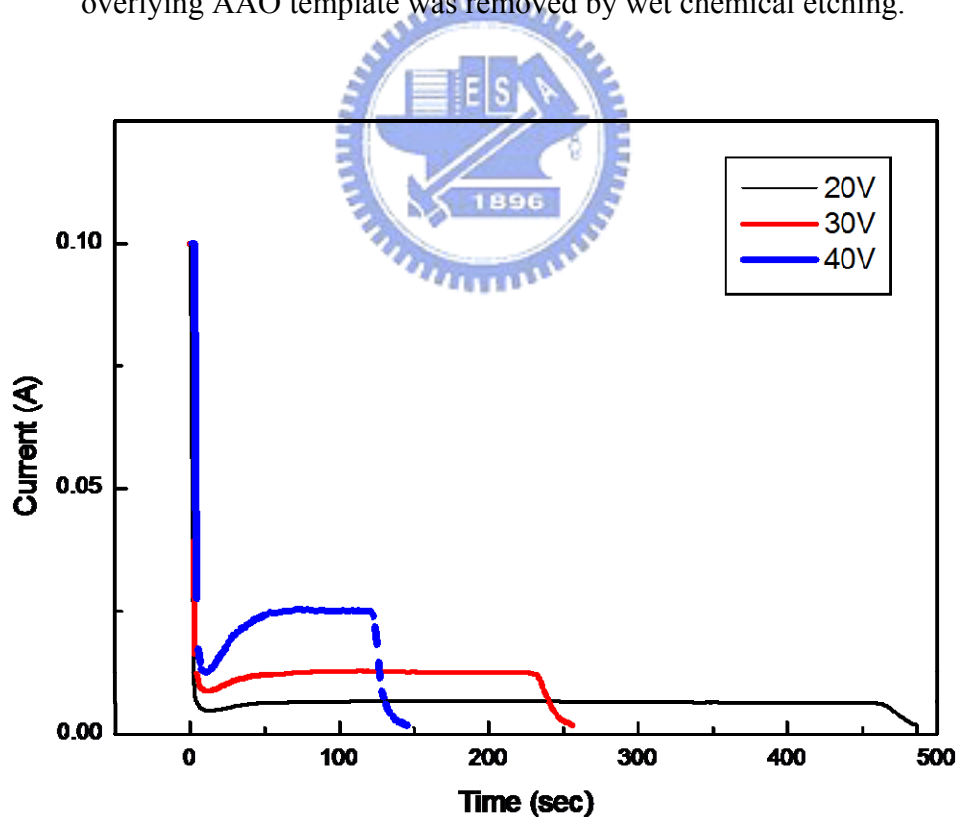
Figure 4-5   Anodic current density-anodizing time behaviors during the anodization of an aluminum film in a 0.3 M oxalic acid electrolyte under voltages of 20V, 30V, and 40V.

It is obvious that variation of applied voltages correspond to different saturate current densities and anodizing time. High applied voltages characterize high saturate current densities and shorter anodizing time. Figure 4-6(a)-(c) show the top-view FE-SEM image of nanodot arrays of titanium oxides after removing the nanoporous AAO. The self-organized nanodots have a uniform size distribution with diameters of about 30 to 60 nm and interdot distances between about 50 and 100 nm. Figure 4-6(d)-(f) demonstrate the cross-section view FE-SEM images of nanodot arrays of titanium oxides after removing the nanoporous AAO. The self-organized nanodots have a height distribution within 37 to 70 nm. The diameter of the nanodots alters as the distances of the obtained titanium oxide nanodots are plotted as a function of anodic voltages. The interdot distance increases linearly with the anodic voltage and is identical to the interpore distance of AAO nanopores, as shown in Figure 4-6(a)-(c). The dot diameter increases with increasing the anodic voltage as well. During the TiN oxidation, the strong electric field (E) resulting from the applied voltage (V) enhances the outward diffusion of metallic cations from the substrate and/or the inward diffusion of oxygen-containing anions (O^{2-}/OH^{-}) from the electrolyte across the Al_2O_3 barrier layer under AAO pore bottom. The thickness of the Al_2O_3 barrier layer (Da) crucially influences the electric field according to the formula $E = V/Da$ and the ion diffusion rates. As a consequence, the magnified electric field significantly promoted the ion diffusion and overgrow nanodots. Nanodots are grouped into domains, and within a dot array domain, ordered nanodots with hexagonal arrangements can be clearly observed. Aluminum and TiN layers give rise to non-uniform diffusion rates of O^{2-}/OH^{-} ions at the interface and thus results in irregular ion concentration distribution around the growing nanodots. Nanodots prepared from a polycrystalline Al/TiN film stack had an irregular dome shape with a coarse base structure, which is primarily a reflection of the rough interface between the aluminum and TiN layers. In addition, the polycrystalline Al/TiN interface has a higher defect density (such as grain boundary, dislocation, vacancy, etc.) that leads to a non-uniform ion transport through the

50
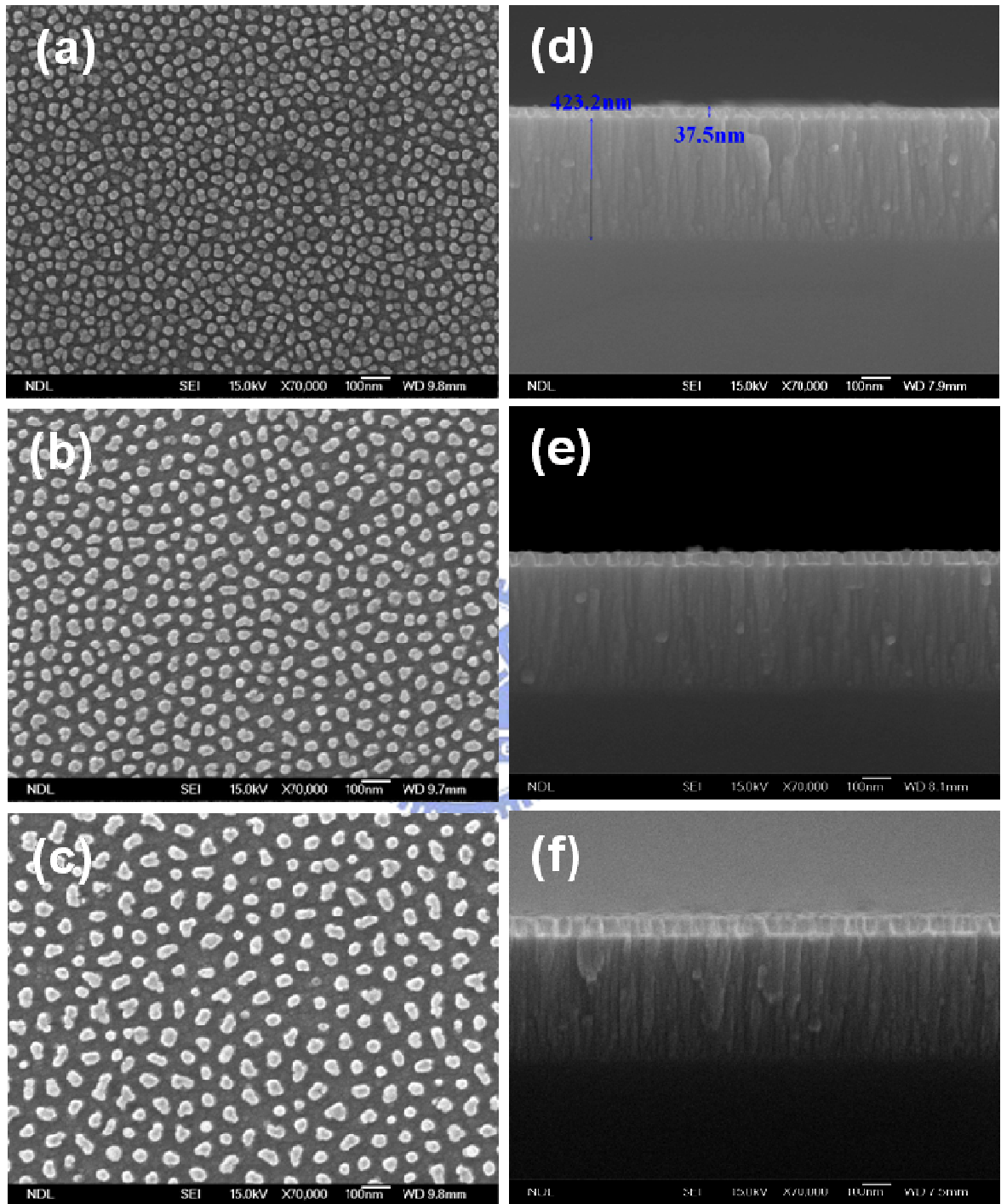
Figure 4-6 FE-SEM images of the nanodot arrays of titanium oxides after removing the nanoporous AAO under varied voltages of (a) 20V, (b) 30V and (c) 40 V for side view and (d) 20V, (e) 30V and (f) 40 V for cross-sectional view.

interface. In grain boundaries, the diffusion coefficient of oxygen species is greater than that of volume diffusion coefficient by several orders of magnitude [142]. That migration of O^{2-}/OH^- ions is faster along grain boundaries, dislocations and external surfaces than in crystal interiors results in the formation of TiOx nanodots with a rough dome structure so that duplication of the circular shape of AAO nanopores is invalid. In contrast, the smoother interface and lower defect density of the epitaxial Al/TiN film stack give rise to circular nanodots with smoother surfaces.

4.3 Summary

Highly ordered nanopore arrays of AAO films have been successfully fabricated on silicon substrates by direct anodization of thick aluminum films deposited on silicon substrates. Aluminum films were introduced to produce nanoporous AAO films with hexagonally arranged nanopores. The pore arrangements show ordered domains with diameters of a few micrometers (short-range order). The formation of the ordered hexagonal pore arrays is responsible for the volume expansion of aluminum during oxide formation that causes repulsive forces between neighboring pores and promotes the self-organization of pores. By tuning the anodic voltage, nanodots have a uniform size distribution with diameters of about 30 to 60 nm and interdot distances between about 50 and 100 nm.

Chapter 5

Field emission study on TiN nanorod arrays

5.1 Introduction

In the past decade, electron field emissions from various nanostructured materials have been comprehensively studied for their excellent field emission characteristics due to the small effective emitting area and the high aspect ratio geometry and have well been proved to be highly promising for electron field emitter applications. In addition to the wide investigation on carbon nanotubes, efforts have been laid upon field emission investigations on numerous oxide and nitride nanomaterials, such as nanowires and nanotubes of ZnO [143], IrO_2 [106], RuO_2 [144], TiO_2 [61], GaN [145] and TiN [146].

However, most nanostructured field emitters in report did not have ordered arrangements because the preparation methods did not provide growth processes to regulate the growth pattern of emitters. Arrangement disorder and field emitter density affect field emission performances adversely. Porous anodic aluminum oxides (AAO) were used in previous studies as templates to prepare titanium oxide (TiO_x) nanodot array with hexagonally close-packed (hcp) arrangements on Si substrates [28, 147]. TiO_x nanodots worked as masks to fabricate well ordered Si nanocone field emitter arrays [148]. Since TiO_x nanodots are produced by partial anodic oxidation of TiN barrier layers between Al thin films and Si substrates, direct preparation of ordered TiN nanostructures with compliant arrangements with TiO_x nanodots is consequently an easy approach. TiO_x nanomasking and reactive ion etching facilitate TiN nanorod array fabrication and studies on field emission characteristics of TiN emitters. Since the TiO_x nanomask formed on the TiN layer had a dome shape, removal of the nanomask left a concave surface on the top of the nanorod and resulted in a protruding edge and better field emission characteristics.

5.2 Fabrication of TiN nanorod arrays

The fabrication process of TiN nanorods on Si substrates is schematically illustrated in Fig. 5-1. Thin TiN films in 500 nm thickness were first sputtered and deposited at room temperature on 6-inch p-type Si (100) wafers with a resistivity of 15-25 Ω-cm, and followed by the deposition of Al films in 1.5 μm thickness on TiN layers by thermal evaporation. Anodic oxidation of the Al film was carried out in 0.3 M oxalic acid ($H_2C_2O_4$) at 25°C under a constant polarization voltage of 40V for 20 min. Under the anodization condition, the AAO template had a uniform pore size of ~70 nm - 80 nm and a pore channel depth of ~2 μm. As the Al anodization was completed, the underlying TiN film could be partially anodically oxidized as well to form TiO_x nanodots under the bottom of AAO pore channels. The AAO layer was removed by wet chemical etch in a solution of 6 wt % H_3PO_4 and 1.5wt % CrO_3 at 60°C for 40 min. TiO_x nanodots were then used as nanomasks to etch TiN layers in an inductively-coupled-plasma reactive-ion-etch (ICP-RIE) system with the gas mixture of BCl_3 and Cl_2 as plasma source. Working conditions of the RIE process were 400 W plasma power, 100 W substrate bias power, 10 mtorr working pressure and 35 sccm flow rate of the plasma gas source. After RIE etching for 50 sec., vertical TiN nanorods in ~200 nm height were formed beneath TiO_x nanomasks. TiO_x nanomasks were removed by wet etch with dilute aqueous HF solution, and TiN nanorods were then annealed at 600°C in vacuum for 3 hours.

5.3 Characterization of TiN nanorod arrays

TiO_x nanodots produced from the anodization of aluminum films in 0.3 M oxalic acid electrolyte under 40V were used as nanomasks to etch TiN layers. After the RIE etch, the side-view FE-SEM images of nanorod arrays under RIE etching time of 0, 20, 30, 40, 50, and 60 sec. are shown in Figures 5-2(a)-(f), respectively. Micrographs clearly present that hexagonal arrangements and nanorods are in accordance with nanopores of the AAO
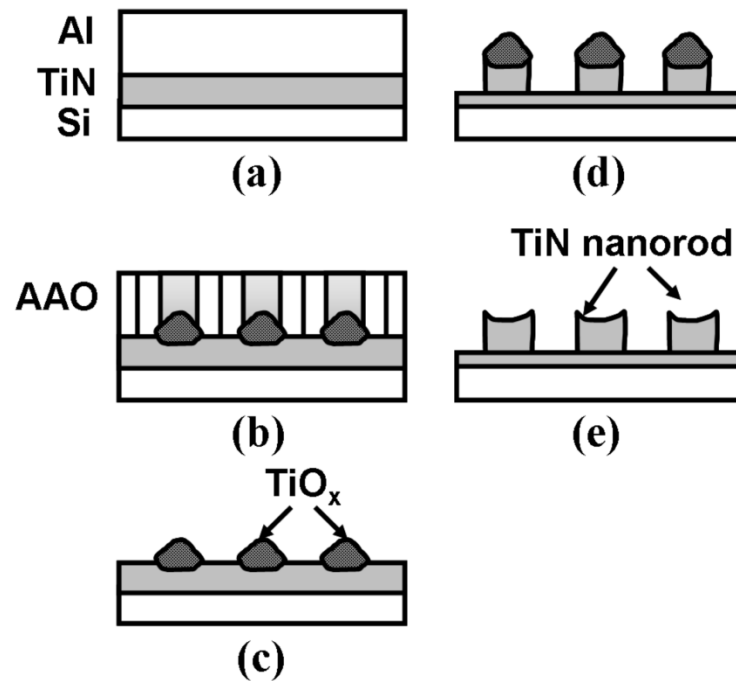
Figure 5-1 Fabrication process of TiN nanorods on Si substrates: (a) sputter deposition of TiN and Al thin films, (b) electrochemical anodization of the Al film and formation of TiO_x nanomasks, (c) removal of the AAO layer by wet etch, (d) reactive-ion-etch of the remanent TiN layer, (e) removal of TiO_x nanomasks by wet etch.

template. As etching time increases to 60 sec. TiN nanorod structure has undercut phenomenon. The FE-SEM image obviously reveals the thick upside and the thin bottom of the TiN nanorod. TiN nanorod is random in orientation. TiO_X nanomasks could endure the RIE etching time 50 sec to protect TiN nanorods in the experiment. Revealed in Figures 5-3(a)-(e) are the cross-section view FE-SEM images of TiN nanorods under RIE etching for 0, 20, 30, 40, and 60sec. Anodization was conducted in a 0.3 M oxalic acid at 40V. TiN nanorod height increased with etching time. When etched for 50 sec, the nanorod is about 200 nm in height and most nanorods had diameters ranging from ~30 nm to ~45 nm. The remaining TiN layers under nanorods exhibited a columnar feature and this is the typical grain microstructure of thin TiN films grown by sputter deposition.
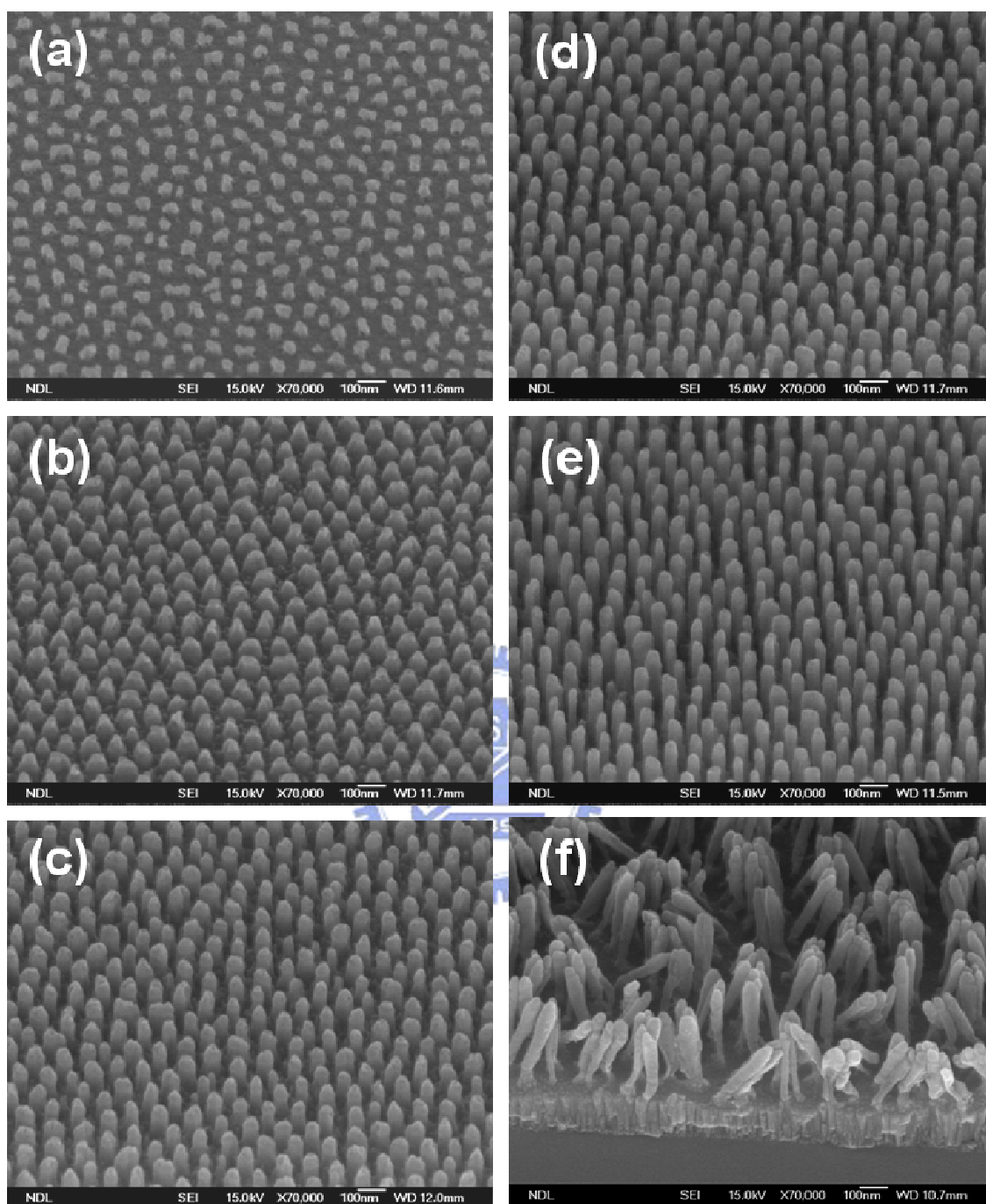
Figures 5-2 (a)-(f) show the side view FE-SEM images of TiN nanorods under RIE etching for 0, 20, 30, 40, 50, and 60 sec.. The anodization was conducted in a 0.3 M oxalic acid aqueous solution at 40V.
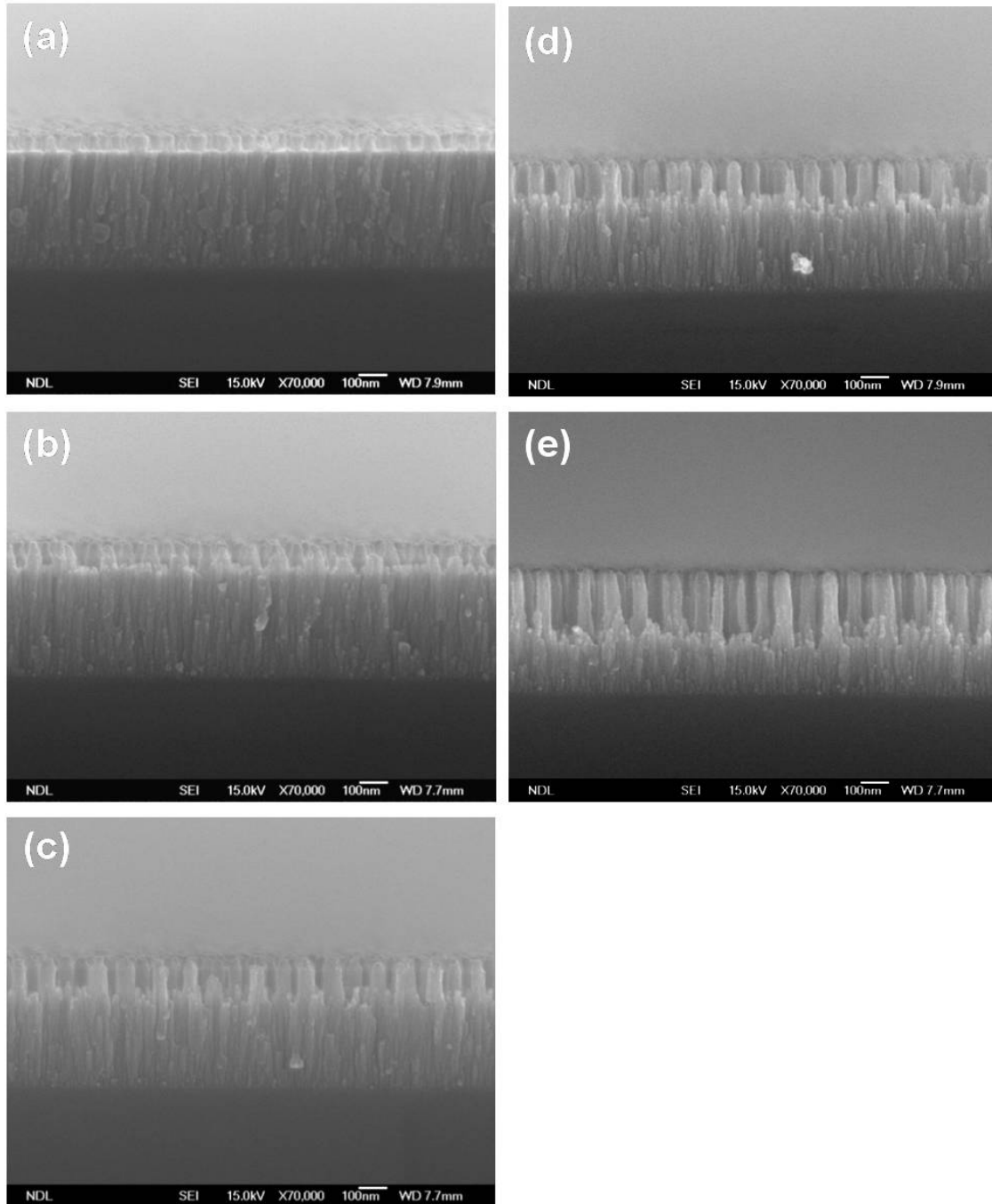
Figures 5-3 (a)-(e) show the cross-section view FE-SEM images of TiN nanorods under RIE
etching for 0, 20, 30, 40, and 50 sec.. The anodization was conducted in a 0.3 M
oxalic acid aqueous solution at 40V.

The side-view SEM image shows that the nanorod arrangement was compliant with the pore arrangement of the AAO template and had a nanorod density of ~1×10^{10} cm^{-2}.

TEM images of TiN nanorods capped with TiO$_x$ nanomasks are shown in Fig. 5-4. Fig. 5-4(a) clearly tells that TiN nanorods have columnar grain structures along the nanorod axis, and the top is capped with a TiO$_x$ nanomask of a curved interface. Because electrons suffer fewer scatterings during transporting through the columnar grain, the electrical resistance along the direction of the TiN nanorod axis should be small compared with other directions. A lower electrical resistance of the cathode will lead to a smaller voltage drop in the emitter bulk, and can thus produce a larger emission current. Figure. 5-4 (b) shows the enlarged picture of the nanorod apex. TiO$_X$ is obviously amorphous in structure. After thermal treatment at 600°C in vacuum for 3 hours, TEM images of TiN nanorods capped with TiO$_2$ nanomasks are shown in Figures 5-5. TiO$_2$ nanomask height shown in Figures 5-5 (a) is 35 nm on the nanorod apex. Figures 5-5 (b) is the enlarged picture of the nanorod apex. The two nanocrystals lattice spacings were estimated to be 2.71 Å and 3.51 Å, which corresponded to anatase (110) and (101) lattice orientations of TiO$_2$ crystals, respectively. Each grain size is smaller than 10 nm.

Particle sizes crucially determine the thermodynamic phase stability at ultrafine sizes [149]. According to the calculated results, when particle size decreases below 14 nm, the total free energy of rutile is higher than that of anatase, but the reverse are the relative phase stabilities of anatase and rutile, and anatase accordingly becomes the thermodynamically stable phase as shown in Figure 2-10. SEM images in Figures 5-6 exhibit TiN nanorods after the removal of TiO$_x$ nanomasks. Figures 5-6 (a) is the cross section view of the TiN nanorod array. After the removal of TiO$_x$ nanomasks, TiN is as high as about 200 nm and most nanorods have diameters ranging from 30 nm to 45 nm. Nanorods have a concaved top surface as shown in the enlarged image in Fig. 5-6 (b).
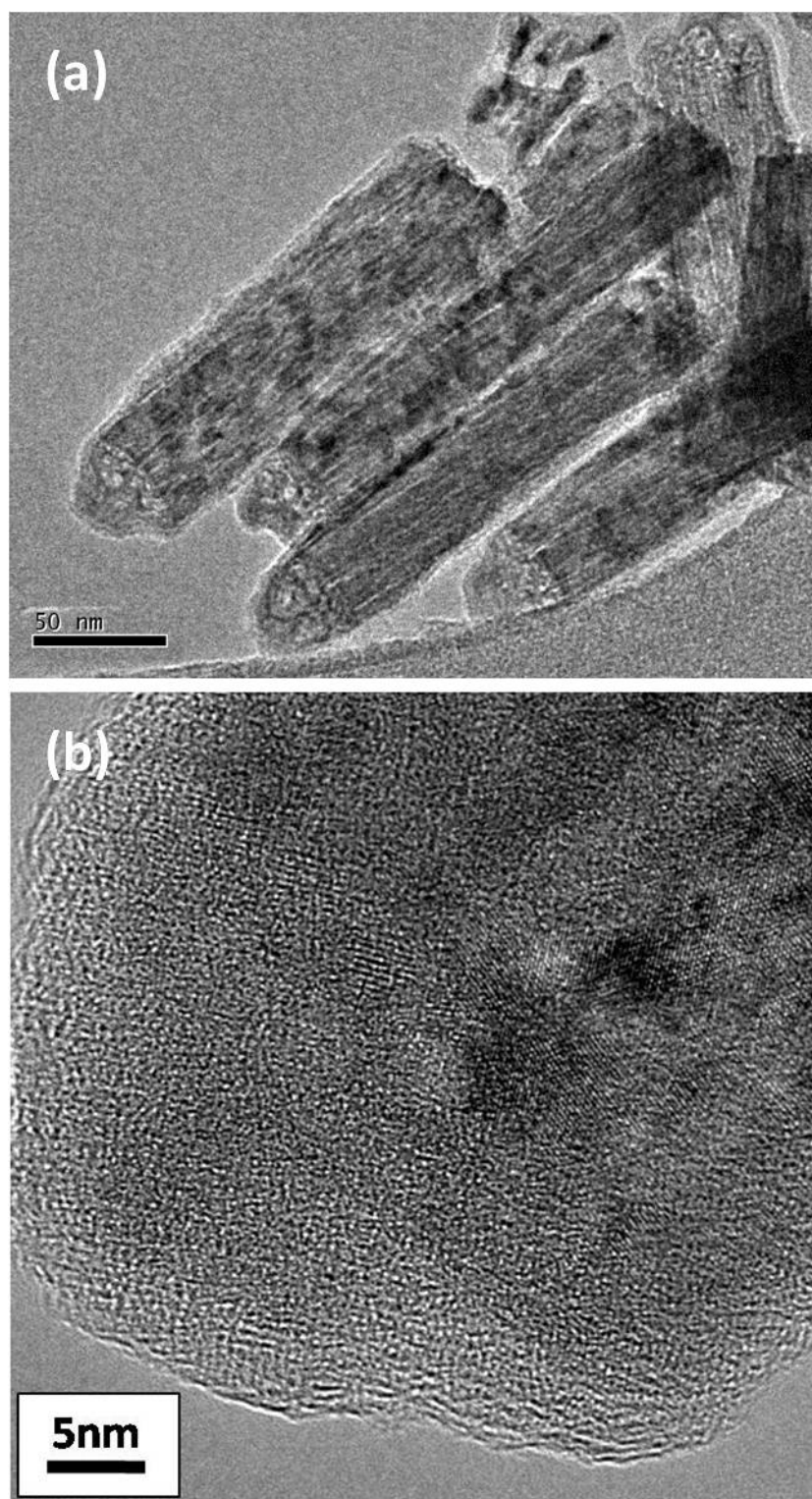
Figures 5-4 shows TEM images of TiN nanorods capped with TiO_x nanomasks. (a) is the corresponding low magnification TEM image. (b) is the enlarged picture of the nanorod apex.
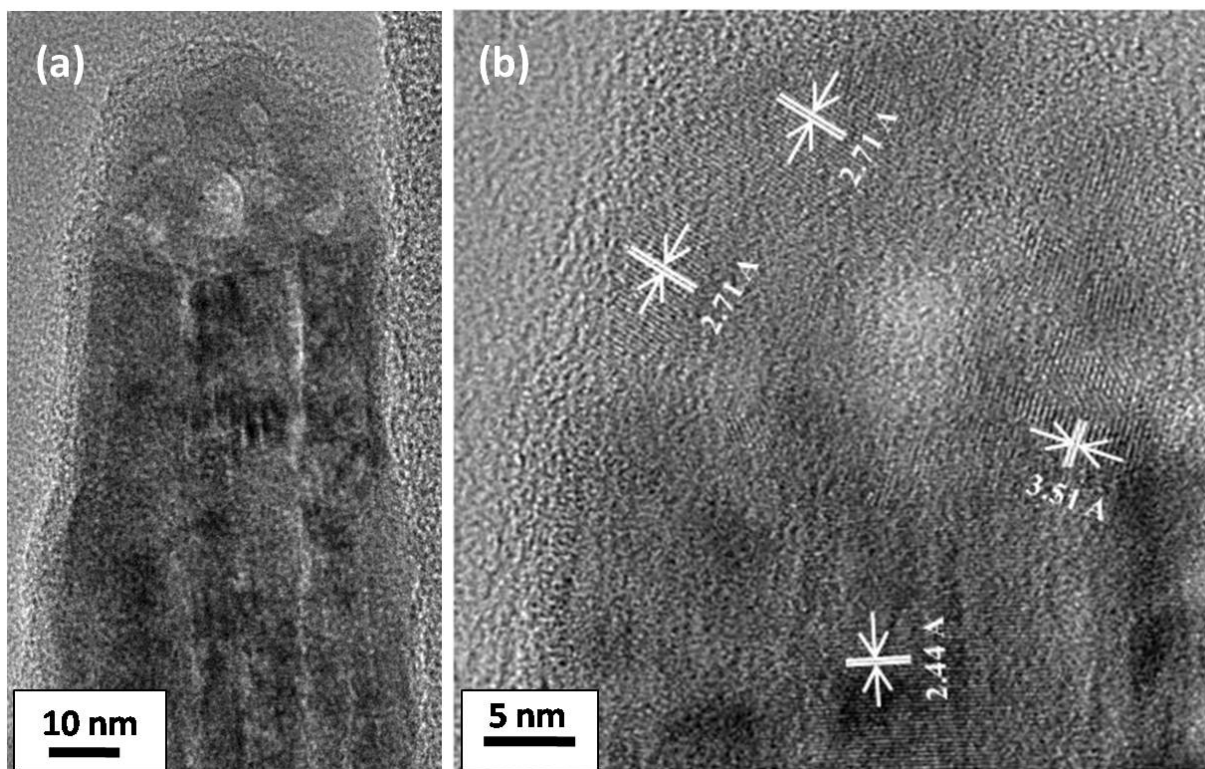
Figures 5-5 shows TEM images of TiN nanorods capped with TiO$_x$ nanomasks after annealing at 600°C in vacuum for 3 hours. (a) is the corresponding low magnification TEM image. (b) is the enlarged picture of the nanorod apex.

The depressed area on the top is resulted from the removal of the dome-shaped TiO$_x$ nanomask formed in the final stage of AAO anodization and with a convex bottom embedded in the TiN layer. Some TiN nanorods have a less regular top shape with a larger diameter. The irregular dome shape [28,147] is due to that TiO$_x$ nanodots, which regulated the final geometric shape of the nanorods during dry etch, are formed at domain boundaries of AAO templates. The presence of crystalline TiN nanorod is confirmed by glancing angle X-ray diffractometry and TEM study. The XRD spectrum shown in Figure 5-7 shows three reflection peaks indexed as (111), (220) and (311) for the cubic TiN lattice structure.
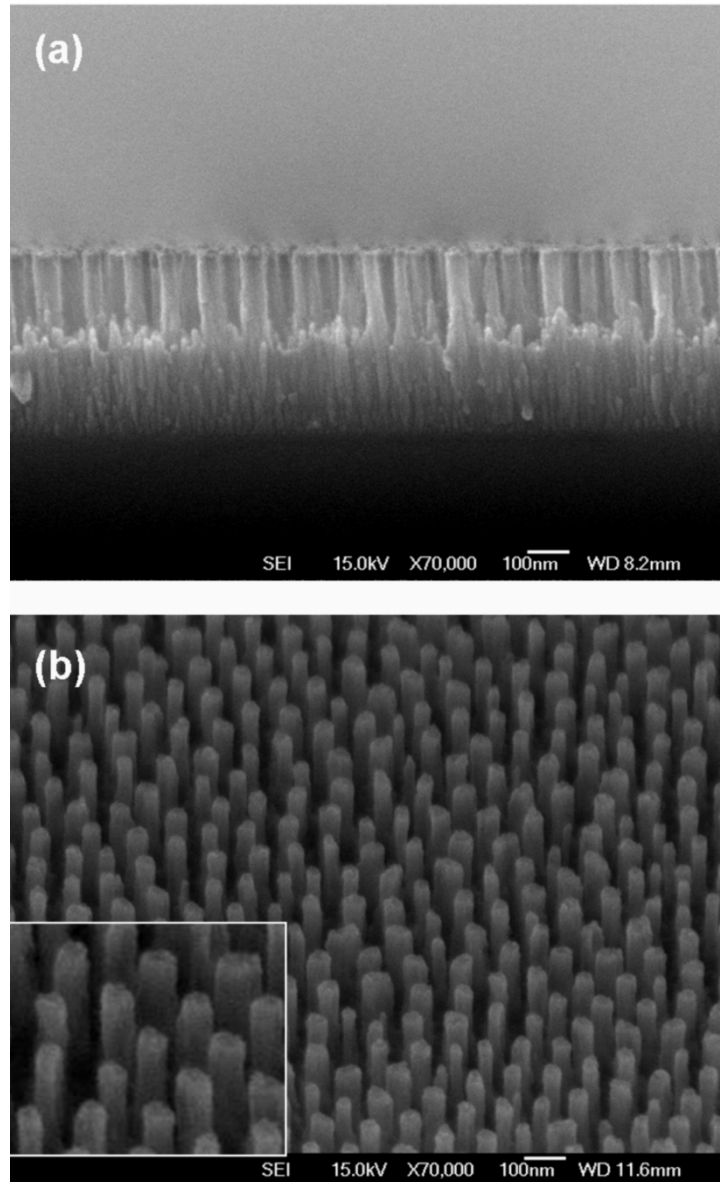
Figure 5-6 shows SEM images of TiN nanorods of 50 sec.etching after the removal of TiO_x nanomasks: (a) cross-section image and (b) side-view image.

The inset of Fig. 5-8(a) is the selected area diffraction (SAD) pattern of the TiN nanorod. Three diffraction rings are indexed as (111), (200) and (311) lattice orientations of the TiN cubic lattice structure. Figure 5-8(b) shows the high resolution TEM image of the upper portion of a TiN nanorod after the removal of the nanomask and vacuum annealing treatment. The fringe spacing of two nanocrystals are estimated to be 2.10 Å, which corresponds to (200)

lattice orientations of the TiN crystal. On the top of the nanorod, a protruding edge was formed. The protruding feature of the top edge can significantly affect field emission characteristics of the TiN nanorod array due to the local field enhancement effect.
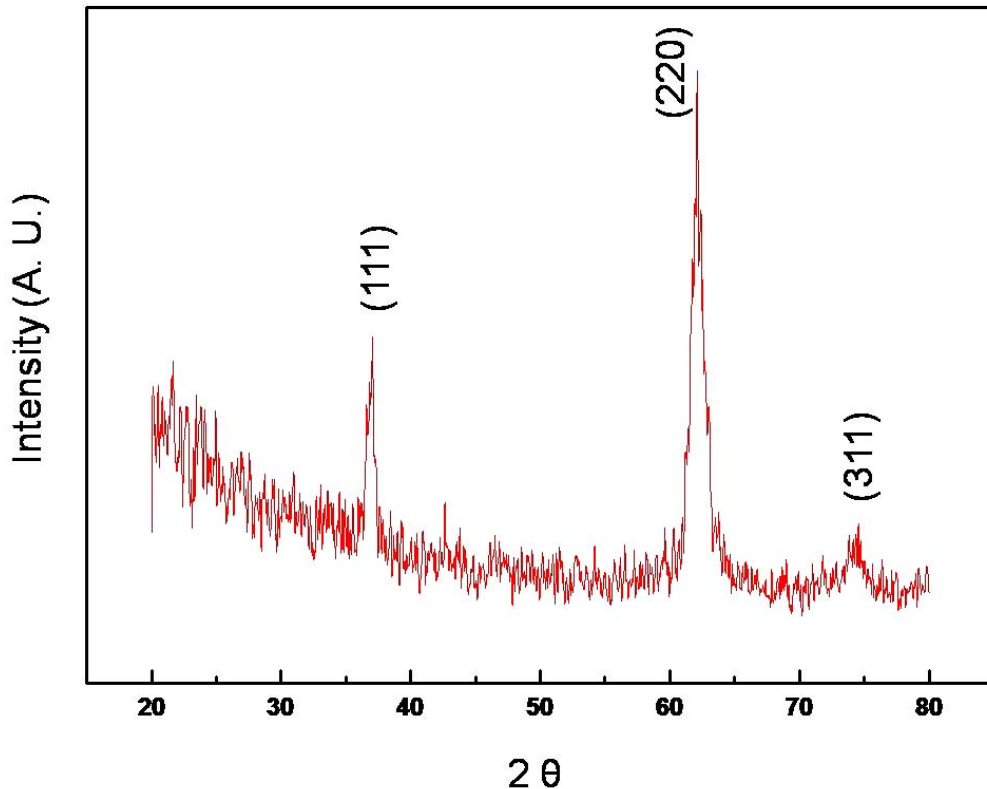
Figures 5-7 shows the glancing angel XRD spectrum of the TiN nanorod array after the anneal treatment at 600°C.

5.4 Field Emission from TiN Nanopillar Arrays

Figure 5-9 illustrates the field emission current density - applied electric field (J-E) curve of TiN nanorod arrays. Also shown in the figure is the corresponding Fowler-Nordheim (F-N) plot. The F-N plot of TiN nanorod arrays exhibits two linear segments between 150 – 500 V with a break at ~250 V. The turn-on field of TiN nanorods, which is herein defined as the field at the intersection of the two straight lines extrapolated separately from the first linear rising segment and the background of the F-N plot, is determined to be 1.6 V/μm.
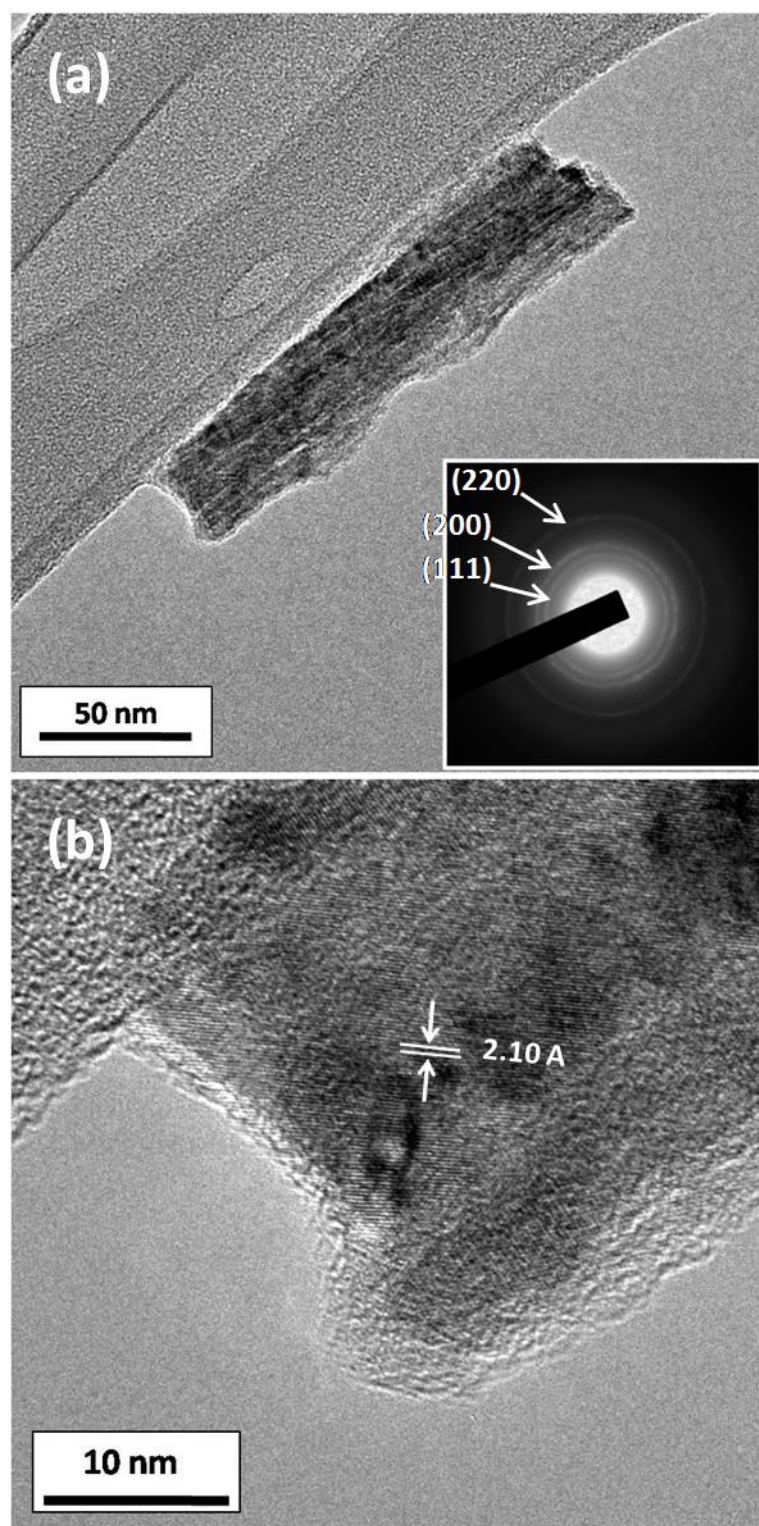
Figures 5-8 shows the TEM image of the TiN nanorod after the removal of the nanomask and the vacuum anneal treatment. (a) is the corresponding low magnification TEM image. (b) is the enlarged picture of the nanorod apex.

As compared with other field emitter arrays fabricated with AAO templation, the TiN nanorod array has a better turn-on field. For instance, our previous reports indicate that AAO templated carbon nanotubes, TiO_2 nanodots and α-carbon coated Si nanocones have turn-on fields of 3.1, 5.6 and 6.2 V/µm, respectively [62] [148] [150]. These field emitter arrays are similar in emitter density and comparable in work function ($\sim$ 4.6 eV) but different in geometric shapes at the emitting site. In general, field emission characteristics of an emitter are primarily determined by the work function and geometric structure of the field emitter. Therefore, the low turn-on field of TiN nanorods can be ascribed to the high aspect ratio and the presence of the sharp top edge on nanorods as will be discussed later. In addition, even if the presence of the top edge was ignored, a turn-on field of ~2.5 V/µm estimated from the linear segment in the high voltage regime was nevertheless better than that of carbon nanotubes grown in AAO. This is probably due to that TiN nanorods are better aligned and more uniform in arrangement than CNTs grown in the AAO, resulting in a smaller screen effect and a smaller consequent turn-on field. Moreover, the low electrical resistivity of the TiN nanorod with the columnar microstructure can help to sustain a high conduction current and lead to a better field emission performance.

Based on the Fowler-Nordheim field emission theory, the emission current is related to the applied voltage by the following equation:

$$I = aV^2 \exp(-b/V) \tag{5-1}$$

where V is the applied voltage, and a and b are generally considered as constants for a given field emission measurement. a is a function of the emitting area, cathode work function (ϕ) and field enhancement factor (β). The enhancement factor β correlates the applied voltage with the local electric field E_{loc} at the emitting surface by the relation $E_{loc} = \beta(V/d)$, where d is the separation between the cathode and the anode, and is closely related to the geometric shape of the field emitter. According to Eq. (5-1), the slope of the F-N plot equals b, which denotes for $Bd\phi^{3/2}/\beta$ with B as a constant. The slopes of the two segments in the low and high

applied voltage regimes are calculated to be about -120 and -550, respectively. Because β is inversely proportional to the slope, the low voltage regime should have a larger β value than the high voltage regime by a factor of ~4.6. In general, field emitters with a small tip radius and a high aspect ratio have a high enhancement factor. The higher β value in the low voltage regime by a factor of ~4.6 suggests that the shallower linear segment was due to field emission from the protruding edge on the top of the TiN nanorod. Since the emitting area at the top edge occupies only a small portion of the cross-section of the nanorod, significant current emission does not occur until the applied voltage reaches ~250 V, where the two linear segments intercept.

For the protruding structure on the top of an field emitter, the measured field enhancement factor (β_T) at the protrusion equals the product of the enhancement factor of the bulk emitter (β_1) and the local enhancement factor due to the protrusion (β_2), $\beta_T = \beta_1 \times \beta_2$ [151]. If the contribution of the protruding edge to the total emission current measured in the high voltage regime is not important because of the very small effective emitting area, available is the assumption that the enhancement factor in the high voltage regime, where the bulk nanorod is the primary emitter, can be approximated to be β_1. Thus the field gain solely due to the protrusion (β_2) is estimated to be ~4.6. When the protruding edge on the top of the nanorod is considered as a wedge-shaped emitter, the geometry of a half cylinder with an elliptical cross section, as shown by the schematic drawing in Fig. 5-9, can be used to evaluate β_2. Kosmahl has derived the relation of the field enhancement factor of a wedge emitter (β_w) with the major and minor axes c and b of the elliptical cross section by

$$\beta_w = 1+(c/\rho)^{1/2} \tag{5-2}$$

where ρ is the radius of curvature of the ellipsoid on the long axis and equals b^2/c [152]. For a wedge-shaped emitter, c and b correspond to the wedge height and the half width of the wedge base, respectively. A rough estimation reveals that the protrusion on nanorods shown in Fig. 5-4(a) has a height in the range of ~7 - 10 nm and the base width of the protruding edge

estimated from Fig 5-8(b) is ~7 nm, i.e., b is ~ 3.5 nm. If an average height of ~8.5 nm is assumed, the elliptical cylinder model will give a value of β_w ~3.4. Compared with the β_2 value, the elliptical wedge model underestimates the field enhancement factor of the
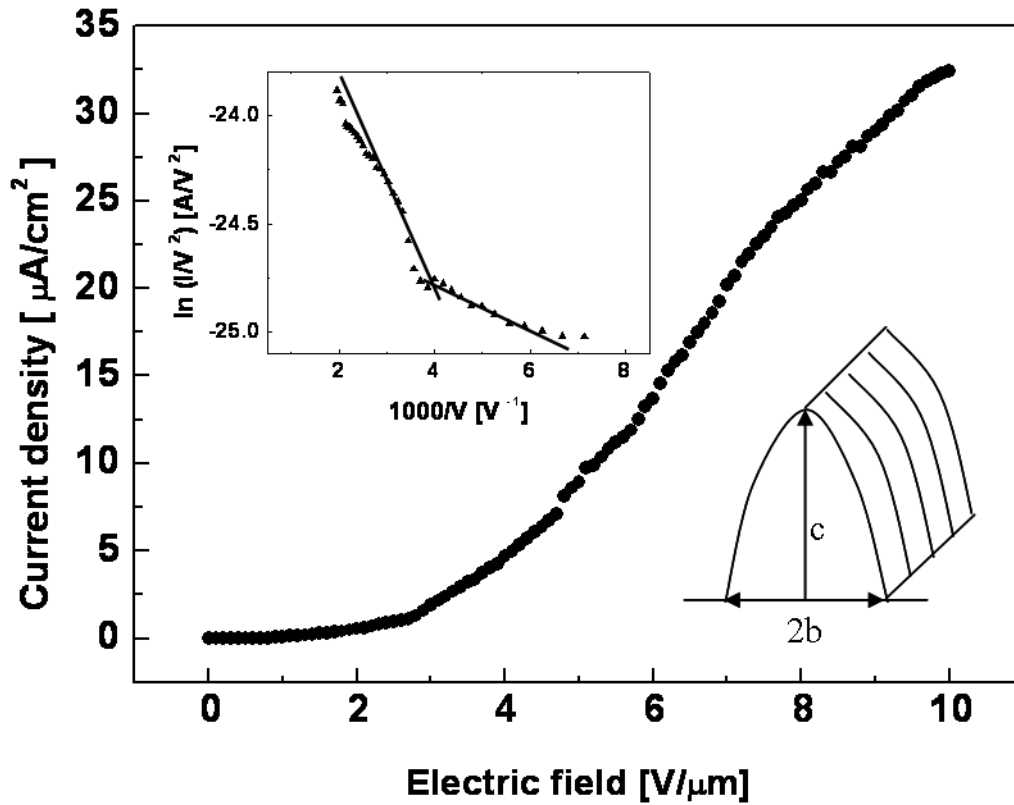
Figures 5-9 shows the J-E curve of the field emission of the TiN nanorod array. The F-N plot is shown in the inset. Also shown in the figure is a schematic drawing of the half cylinder with an elliptical cross section. c and b are the major and minor axes of the ellipsoid, respectively.

protruding edge by ~26%. The underestimation may result from many reasons. First, the geometric shape of the protruding edge is assumed to be an ideal elliptical cylinder and this is not completely true. Moreover, the array technological parameter distribution effect on such field emission characteristics as variations in emitter geometry and work function should be taken into account [153]. This can be easily conceived by examining the TEM image of Fig. 5-4(a), in which nanomask capped TiN nanorods do not exhibit the same boundary shape at

the interface between TiN nanorods and TiO$_x$ nanomasks. In addition, the SEM image of Fig. 5-6(b) also shows a wide distribution of nanorod diameters. Variation in the shape and diameter of field emitters can significantly affect the field enhancement factor through the geometric factor [154], and thus a narrow distribution of the enhancement factor (β_1) over the TiN nanorod array is difficult to obtain. As a result, an underestimation by 26% is considered to be not surprising and it is proper to use the elliptical cylinder model to evaluate the field enhancement effect of the nanosized protruding edge on the field emission of the TiN nanorod array.

5.5 Summary

By reactive ion etching, well ordered TiN nanorods are fabricated on Si substrates with TiO$_x$ nanodots prepared by AAO templation as masks. Removal of TiO$_x$ nanomasks leaves a concaved top surface on TiN nanorods. The protruding edge on the top surface of TiN nanorods results in the nonlinear Fowler-Nordheim field emission characteristics of a low turn-on field of 1.6V/μm. The top edge of nanorods locally enhances the electric field by a factor of ~4.6 and thereby decreases the turn-on field. The elliptical wedge cylinder model is used to estimate the local field enhancement factor of the protruding edge, and an underestimation by ~26% is found as compared with that derived from the F-N plot. The underestimation is ascribed to the large variation in geometric structure of nanorods and the non-ideal elliptical wedge shape of the protruding edge.

Chapter 6

Study on the application of amorphous carbon coated Si nanotip arrays

6.1 Introduction

Nanostructured cold cathode materials have received considerable attention for their potential field emission applications because of the low threshold field for electron field emission [155-159]. Among various materials known to be suitable for the construction of field emission cathodes, crystalline Si has long been used as the starting material to fabricate field emitters owing to the excellent electronic and mechanical properties and well-developed process techniques. Si field emission arrays can be readily fabricated on silicon wafers by standard microfabrication, such as micromachining and integrated circuit processes. Photolithography process is required to manufacture field emitter arrays when conventional microfabrication methods are used and, therefore, the size and density of field emitters are limited by the optical resolution of the lithography tool. Lots of nanofabrication methods with Si wafers to prepare nanoscaled field emitters without photomasking have recently been developed. J. C. She et al. [159-160], C.-H. Hsu et al. [51] and H. C. Lo et al. [161] have prepared Si nanotips by plasma-etching, in which Si substrates used in-situ deposited SiC nanoclusters as nanomasks. Q. Wang et al.[162] have fabricated α-carbon (α-C) coated Si nanotips on a porous silicon substrate in a hot filament chemical vapor deposition system. Either SiC-capped or α-carbon coated Si tip arrays presented considerable enhancements on field emission properties as compared to the uncoated. However, most previously reported Si nanotips did not show an ordered arrangement, because the preparation methods did not provide growth processes to regulate arrangements of nanotips. Herein, porous anodic aluminum oxides (AAO) were employed as templates to fabricate titanium oxide nanopillars

with a hexagonally close-packed (hcp) arrangement, in which TiOx were used as masks to direct the formation of silicon nanotips on Si substrates in microwave plasma chemical vapor deposition (MPCVD) system. The amorphous carbon could be coated in situ onto Si nanotips during the nanotip formation with the gas mixture of CH_4 and H_2 as plasma source. Also studied were field-emission characteristics of α-carbon coated Si nanotips.

6.2 Fabrication of amorphous carbon coated on Si nanotip arrays

Figure 6-1 illustrates the fabrication steps of α-C coated Si nanotips. Sputter deposition of TiN thin films in 30 nm thickness proceeded initially on 4-inch p-type Si (100) wafers of $15\sim25$ Ω-cm in resistivity and followed by the deposition of Al films in 3μm thickness on TiN layers by thermal evaporation. Anodic oxidation of the Al film was carried out in 0.3M oxalic acid ($H_2C_2O_4$) at 25 ^{o}C under a constant polarization voltage of 40V. The underlying TiN film could be partially anodically oxidized to form TiO_x nanopillars under the bottom of AAO pore channels when the Al anodization was completed. The AAO layer was then removed by wet chemical etch in a solution of 6 vol % H_4PO_3 and 1.5wt % CrO_3 at 60 ^{o}C for 40 min. TiO_x nanodots were then used as nanomasks to etch TiN layers and the underlying Si substrates in an inductively coupled plasma reactive ion etch (ICP-RIE) system with the gas mixture of BCl_3 and Cl_2 as plasma source. Working conditions of the RIE process are 400 W plasma power on the 4-inch substrate plate, 100 W substrate bias power, 10 torr working pressure and 35 sccm flow rates for both BCl_3 and Cl_2 gases. Fabrication of α-C coated Si nanotips was then carried out in a microwave plasma CVD (MPCVD) system under the working conditions of 300W microwave power on the 1-inch substrate plate, 200 W bias power, 1 torr working pressure, 20:80 of the CH_4:H_2 sccm ratio and 30 min of deposition time.
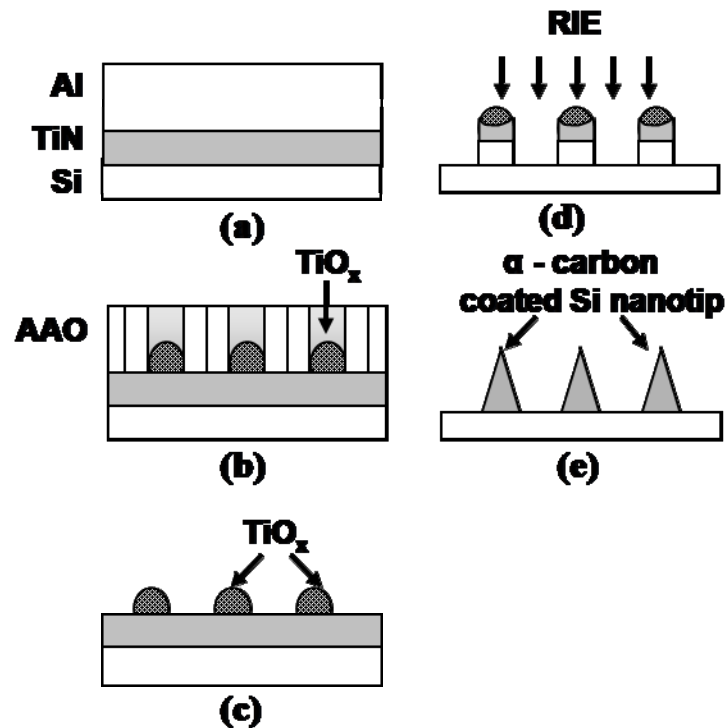
Figure 6-1 shows the fabrication steps of α-C coated Si nanotips: (a) TiN and Al deposited on the Si wafer by physical vapor deposition, (b) anodic oxidation of the Al film and formation of TiO_x nanomasks, (c) removal of the AAO layer by wet etch, (d) reactive ion etch of the remanent TiN and the Si substrate, (e) Si nanotip formation by plasma etch and in-situ deposition of the α-C layer on nanotips during the MPCVD process.

6.3 Characterization of amorphous carbon coated on Si nanotip arrays

Nanoporous AAO template, consisted of highly ordered pore channels with uniform pore sizes between 70 nm and 80 nm and pore to pore distance about 100 nm, was obtained under the anodic oxidation conditions described above. In the late stage of aluminum anodization, the underlying TiN film could also be anodically oxidized as the interface between the electrolyte and the AAO barrier layer approached the TiN area adjacent to the pore bottom [163]. O^{2-}/OH^- ions in the electrolyte solution could diffuse through the thin AAO barrier layer and initiated anodic oxidation of the TiN layer to form titanium oxide nanoparticles

under AAO pore channels. Because the anodic oxidation was accompanied with volume expansion, TiO_x particles protruded out of the TiN layer and grew into a pillar shape. The as-prepared nanopillars were basically amorphous titanium oxides according to our previous study [28]. Figure 2 shows the cross-sectional SEM image of TiO_x nanopillars after the removal of AAO layers by wet etch. TiO_x nanopillars were ~70 nm in height, and, like the AAO template, had a well-ordered hexagonal arrangement as shown in the inset of Fig. 6-2. Since TiO_x nanopillars were only formed under the AAO pore bottom, it was necessary to remove the remaining TiNs before TiO_x pillars were used as hardmasks to fabricate Si nanotips. In order to etch the TiN layer, a gas mixture of BCl_3 and Cl_2 was used as plasma source in the ICP-RIE system.
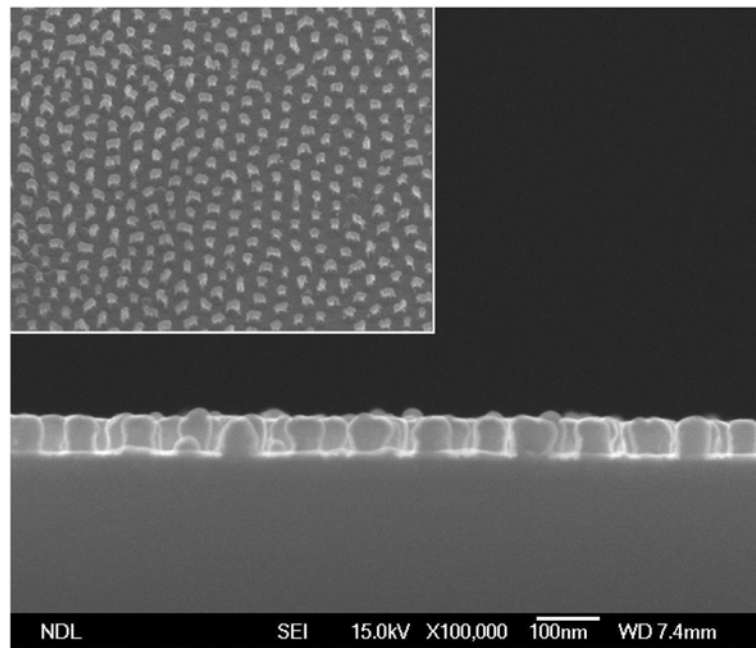
Figure 6-2 shows the cross-sectional SEM image of TiO_x nanopillars after the removal of the AAO layer by wet etch. The inset shows the plane-view SEM image of TiO_x nanopillar arrays.

TiO_x and Si could also be etched by the chorine-based plasma source, but the relatively large height of TiO_x nanopillars provided sufficient masking thickness to the underlying TiN and Si substrate so that the arrangement pattern of nanopillars could be successfully transferred to

the Si substrate. RIE etch leaded to the formation of a well-ordered nanocone structure with

TiO_x and TiN on the apex and Si at the lower portion of the nanocone.

Figure 6-3 shows a side-view SEM image of the nanocone array after the RIE etch for (a) 40 sec., (b) 45 sec., (c) 50 sec., (d) 55 sec. and (e) 60sec.. The nanocone array had a hexagonal arrangement as the TiO_X nanomask. From the SEM image, some nanocones exhibited a less regular cone shape, and the remanent TiO_x/TiN nanomasks were not very uniform in size. This was due to that the pattern transfer from those irregular TiO_x nanopillars formed under AAO pore channels near domain boundaries of the AAO template layer would produce nanocones with irregular shapes [163]. After the RIE process, the thus prepared TiO_X/TiN/Si nanocones then received further plasma treatment in the MPCVD system with the gas mixture of H_2/CH_4 as plasma source. During the plasma treatment, the residual TiO_x and TiN were completely removed and the formation of sharp Si nanotips could be achieved by chemical erosion with hydrogen radicals and ion sputtering. Figure 6-3 (a1), (b1), (c1), (d1) and (e1) are the side-view SEM images of Si nanotips after plasma treatments of nanocone arrays after RIE etches for 40 sec., 45 sec., 50 sec., 55 sec. and 60sec., respectively. The tip-to-tip distance of most Si nanotips shown in the SEM image was ~100nm and close to the AAO pore-to-pore distance. Under RIE etch for 60 sec. the TiO_x/TiN nanomask became smaller or even disappeared. After the MPCVD process, Si nanotip was scattering while the TiO_x/TiN nanomask disappeared. In this condition, the nanotip height became shorter. According to electron diffraction study as shows in Figure 6-4, nanotips consisted of crystalline silicons. These observations indicated that formation of Si nanotips was a result of plasma etches of the Si substrate. The angle could be tailored by varying the RIE time. The average aspect ratio of Si nanotips, which was defined herein as the ratio of the nanotip height to the diameter at the half height of nanotips, could be also tailored by varying the RIE time.
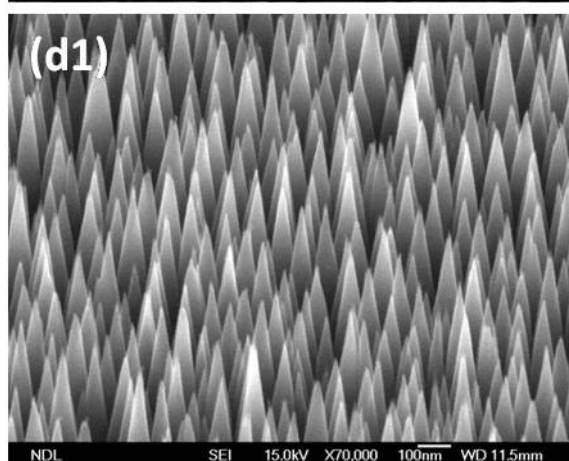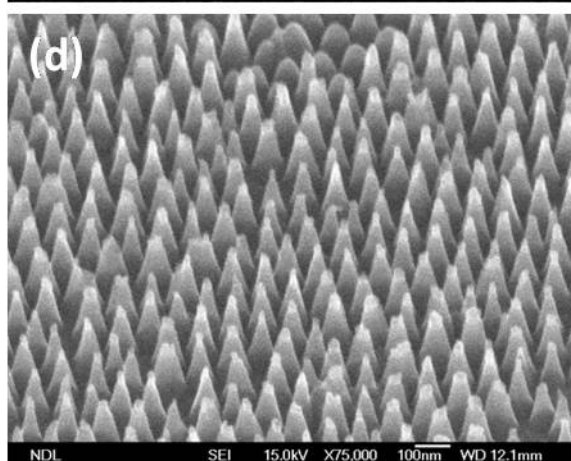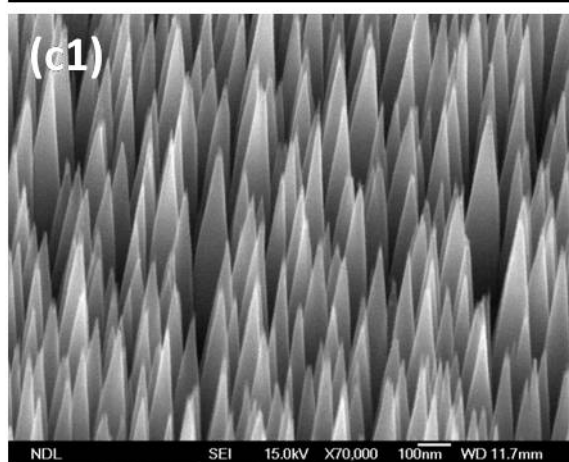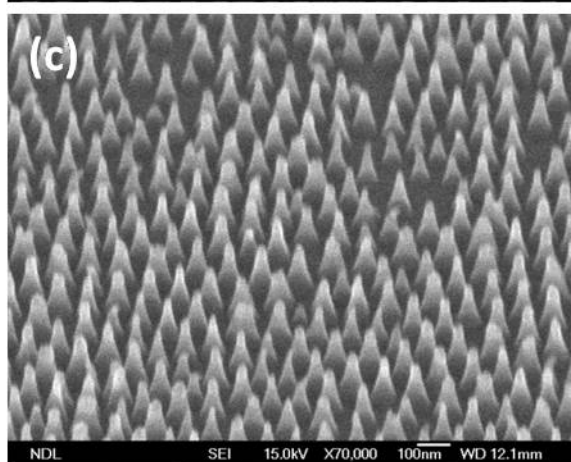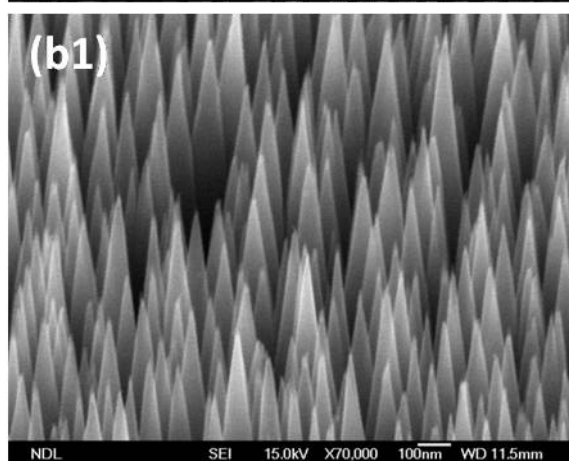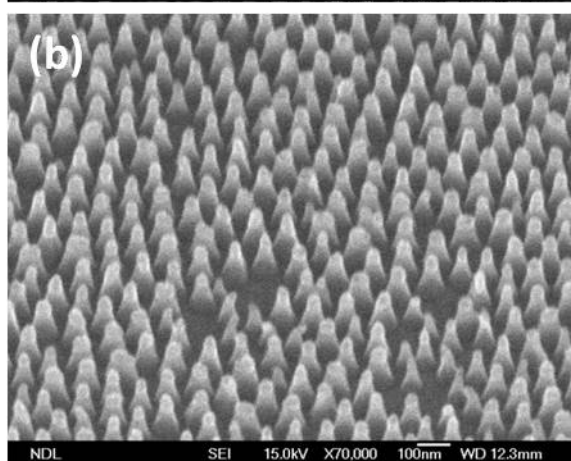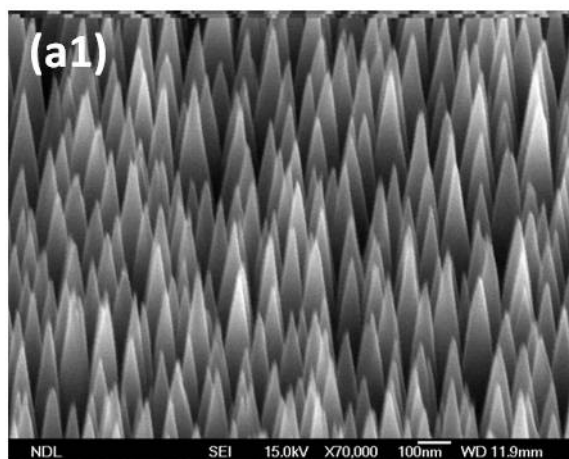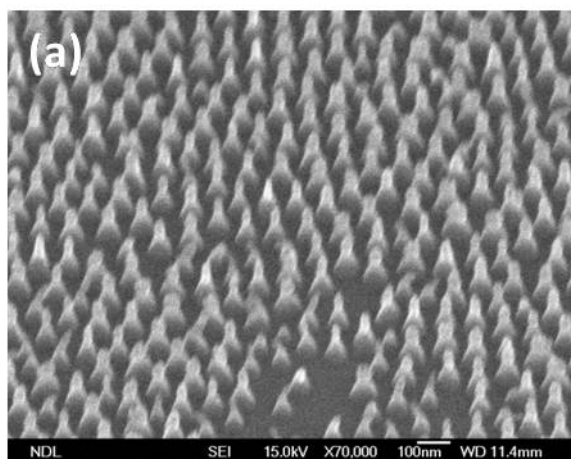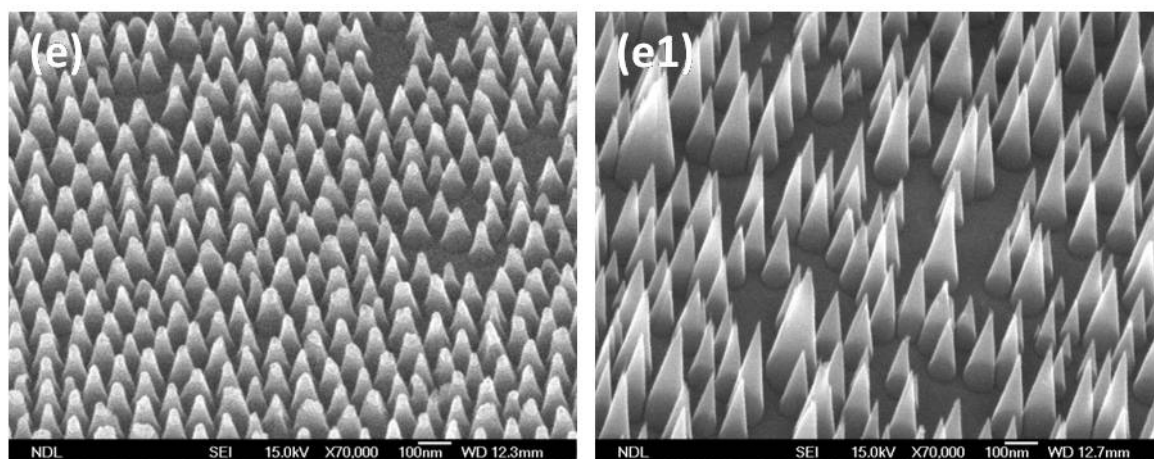
Figure 6-3 shows the side-view SEM images of $TiO_x/TiN/Si$ nanocone arrays after RIE etches for (a) 40 sec., (b) 45 sec., (c) 50 sec., (d) 55 sec. and (e) 60sec. (a1), (b1), (c1), (d1) and (e1) show the side-view SEM images of Si nanotips after plasma treatments of nanocone arrays after RIE etches for 40 sec., 45 sec., 50 sec., 55 sec. and 60sec., respectively.

Longer RIE time might result in the size and thickness reductions of TiO_x/TiN nanomasks and thereby led to the formation of sharper Si nanotips during the MPCVD process. Although rather ordered in arrangement, Si nanotip arrays seemed to be more random than TiO_x nanomask arrays. In addition to that irregular TiO_x nanomasks, such as those denoted in Figure 6-3 (a)-(e), could mis-shape the final geometric configuration of Si nanotips, it was likely that some nanoclusters randomly scattered on Si substrates with the formation of additional Si nanotips. The origin of nanoclusters could be either TiO_x/TiN nanomasks dislodged from the nanocone apex or sputtered and/or redeposited silicon containing clusters during the MPCVD process as reported previously [160].

During the etch of Si substrates in the MPCVD system, a α-carbon layer could be in-situ deposited on Si nanotips. A TEM image of the Si nanotip, separated from the Si substrate by ultrasonic agitation, is shown in Fig. 6-5. The inset shows that the surface of the Si nanotip was coated by an amorphous layer with a thickness of ~5 nm.
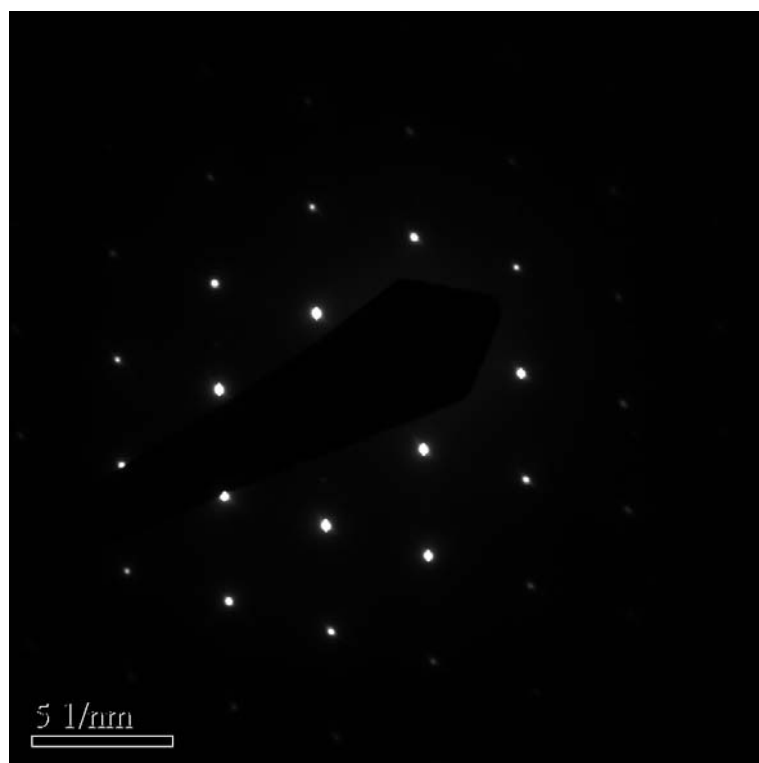
Figure 6-4   Electron diffraction pattern of Si nanotips.

Figure 6-6 (a) shows the bright-field TEM image of the Si nanotip segment coated by an amorphous layer and (b) and (c) reveal elemental mapping of carbon and silicon from Electron Energy Loss Spectroscopy (EELS) imaging, respectively. Analysis of Si nanotips demonstrated that the amorphous layer was mainly composed of carbon. Raman spectroscopy and Auger spectroscopy were employed to probe the chemical structure of the surface α-C layer on nanotips. Figure 6-7 shows the Raman spectrum of the α-C coated Si nanotip array in the range of $1100 - 2000 \text{ cm}^{-1}$. Raman spectroscopy has been widely used to characterize the chemical structure of chemical-vapor-deposited carbon materials, such as diamond-like carbon (DLC) and carbon nanotubes [164,165]. Disordered graphitic carbon materials exhibit two major Raman peaks, G and D peaks, in the range of $1300 - 1700 \text{ cm}^{-1}$ [165] , and the two peaks are often used to characterize sp^2 chemical bonding structure of CVD deposited carbon materials.

75
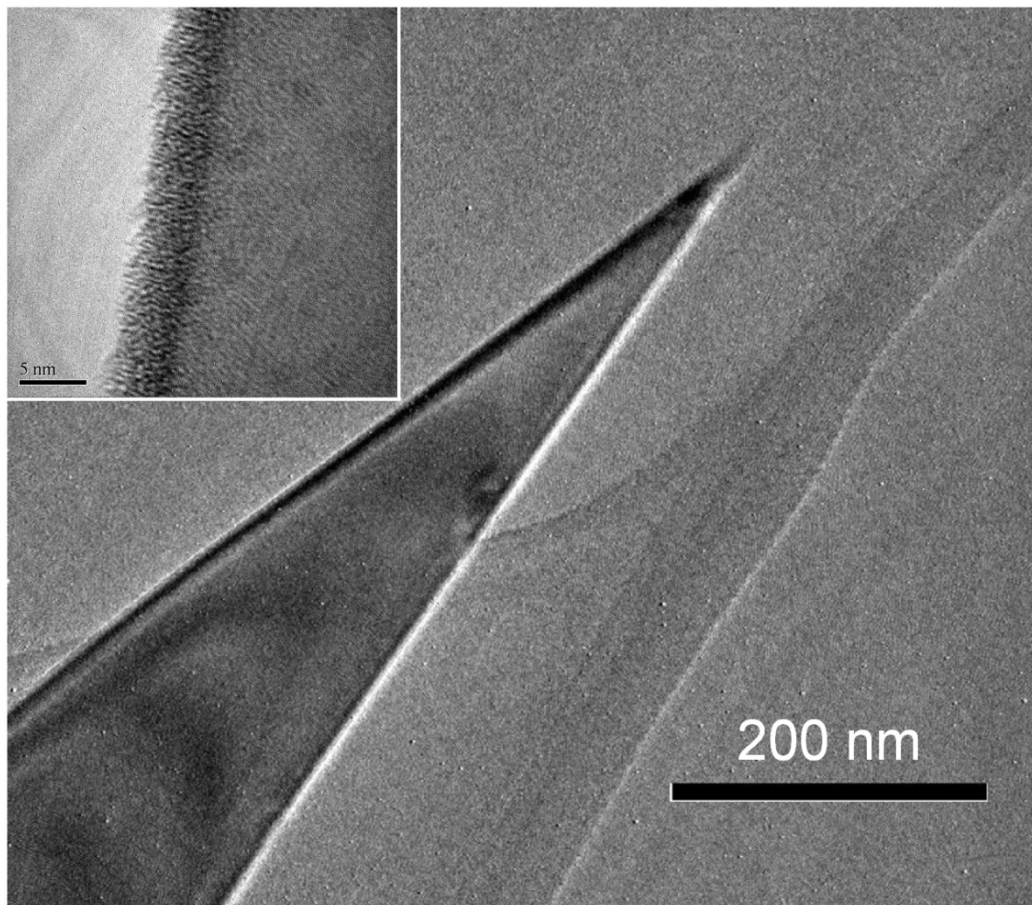
Figure 6-5 shows the TEM image of Si nanotips. The Si nanotip was coated by an amorphous layer with a thickness of ~5 nm as shown in the inset.

The D peak is commonly considered to be a ring breathing mode in a disordered graphitic structure and the G peak is due to sp^2 bond stretching. Peak features of both Raman modes, such as peak position and intensity, are greatly dependent on the sp^2 bonding structure of CVD deposited carbon materials. The G peak is particularlly useful to reveal nanocrystallinity of the graphitic structure [164]. For a perfect and infinite graphite crystal, the D peak is absent in the Raman spectrum and the G peak situates at 1580 cm^{-1}.   As the large graphite crystal disintegrates into nanocrystalline clusters, the G peak shifts to a higher wavenumber and the D peak becomes prominent, as shown in Fig. 6-8. [165].
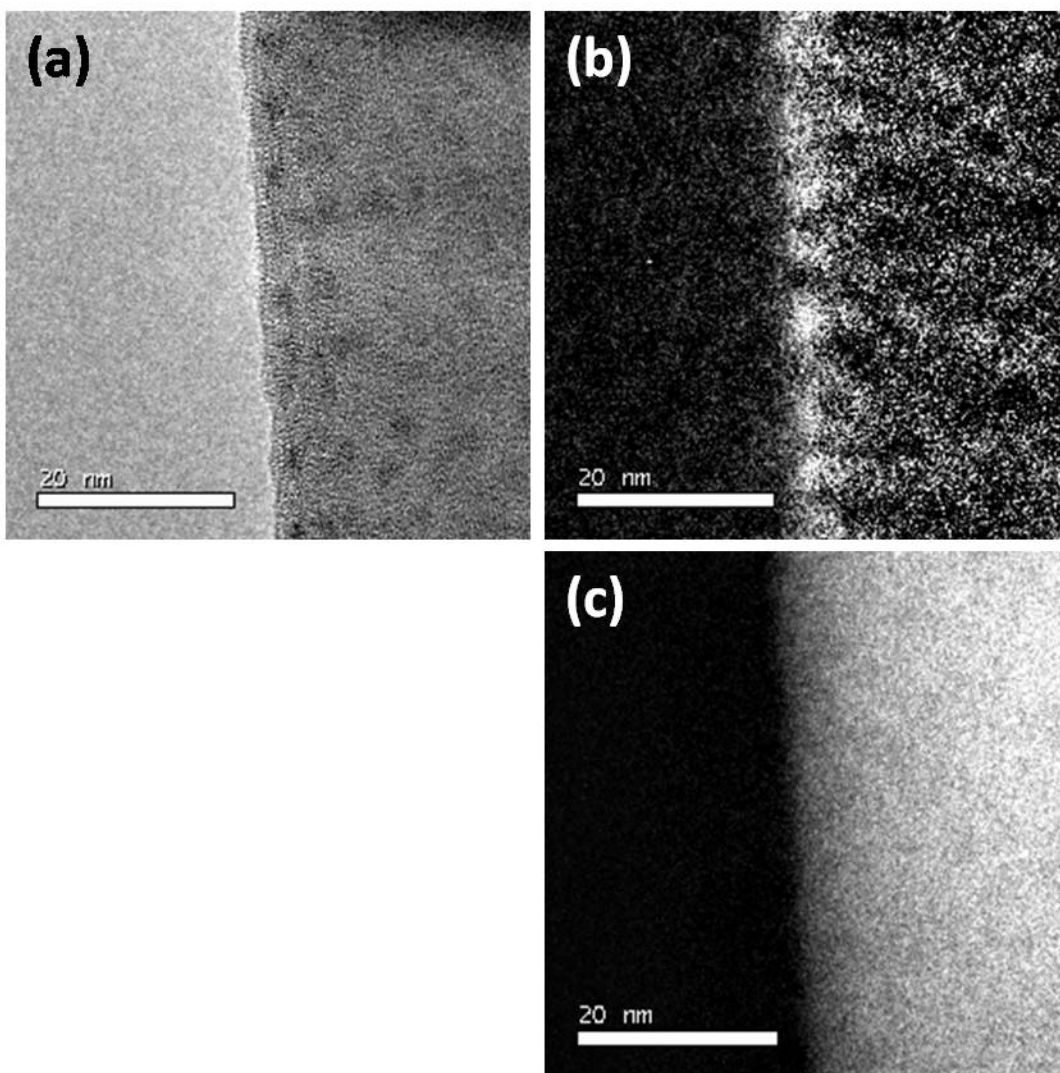
Figure 6-6 shows EELS mappings (a) Bright-field TEM image showing the segment of Si nanotip coated by an amorphous layer; (b) and (c) show elemental mapping of carbon and silicon respectively.

G and D peaks of the carbon overlayer in this study appeared at ~1607 cm^{-1} and ~1335 cm^{-1}, respectively. The peak position of the G mode and a large intensity ratio of the D peak to G peak implied that a significant amount of nanosized graphitic structures were likely present in the carbon layer.
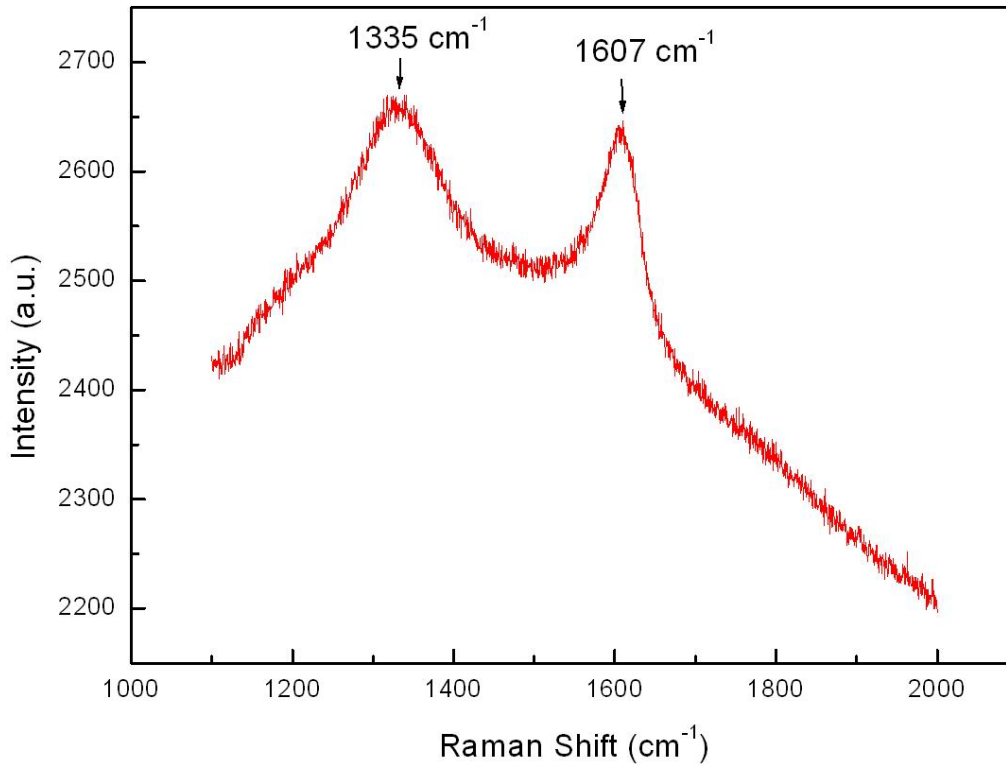
Figure 6-7 Raman spectrum of the α-C coated Si nanotip array.

In addition, Auger study also suggested the deposition of graphitic carbon on the Si nanotips.

Figure 6-9 is a differential C (KVV) Auger electron spectrum in the energy range of 200 - 300

eV for amorphous carbon coated Si nanotips. Because valence electrons are involved in C

(KVV) Auger transitions, the peak position and line shape of C (KVV) series are significantly

affected by the chemical bonding structure of carbon atoms and, therefore, are often used to

qualitatively characterize the allotropic form of carbon. The peaks at ~259 eV and ~246 eV,

are due to the C (KV_1V_1) transition and the C (KV_2V_1) transition, respectively [166-167]. The

Auger line shape demonstrated a chemical structure with more characteristics of graphitic

carbon and suggested that the thin carbon layer was rich in graphitic bondings. This was

consistent with the Raman spectroscopy analysis described above. The presence of

nanocrystralline graphitic structure in the carbon layer on the Si nanotip array provided an

electrically conductive path for electrons to the Si nanotip apex, and thereby made possible a lower turn-on voltage for the field-emission. Otherwise, the relatively high resistivity of the Si substrate, from which Si nanocones were fabricated, would have had retarded the electron conduction and the field-emission performance.
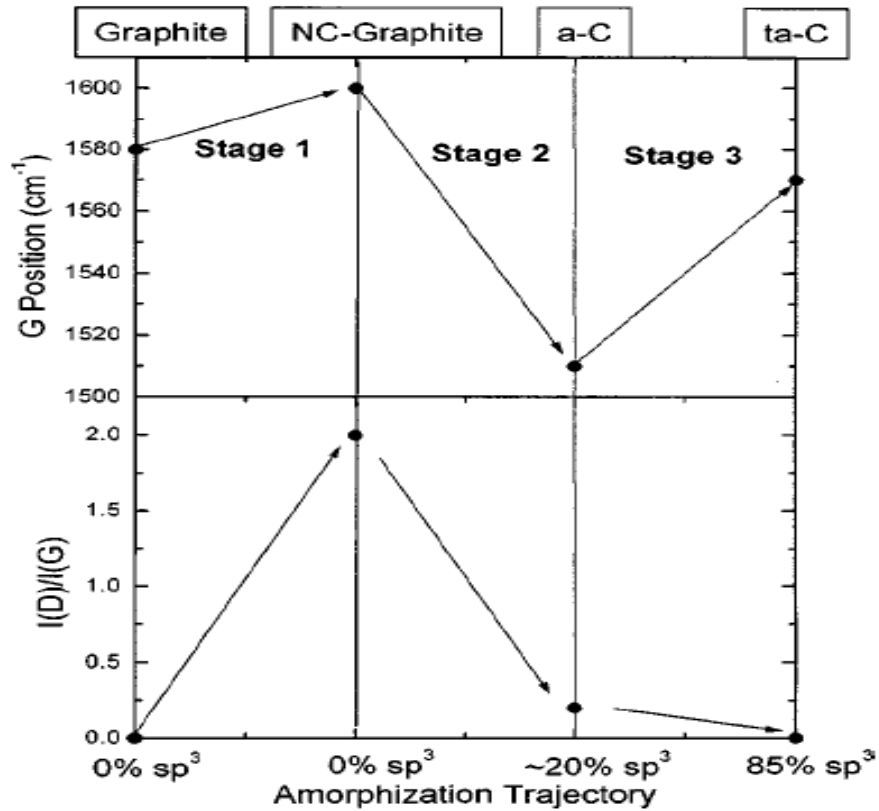
Figure 6-8   Amorphization trajectory showing a schematic variation of the *G* position and
           I(*D*)/*I*(*G*) ratio [165].
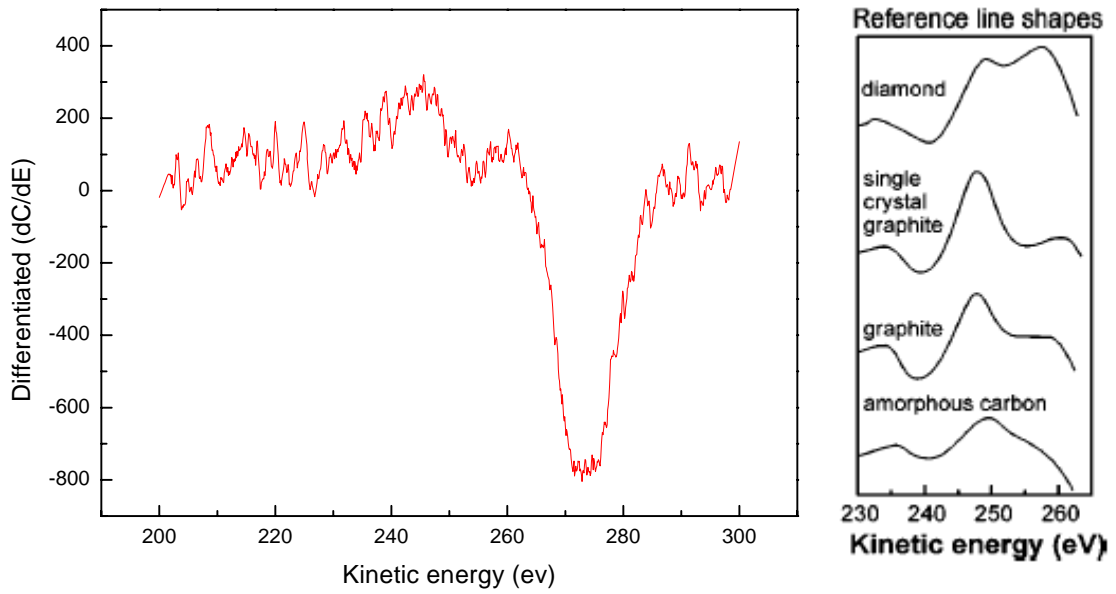
Figure 6-9 shows the C(KVV) Auger electron spectrum of the α-C coated Si nanotip array. Reference line shapes of diamond, graphite and amorphous carbon are provided for comparison [168].

6.4 Field Emission from Amorphous Carbon Coated Si Nanotip Arrays

Sharp Si nanotips could greatly enhance the local field at the tip apex, and thereby dramatically improved the field emission property. The dependence of the emission current density of a field emitter on the applied field obeys the Fowler-Nordheim (F-N) relation [169].

$$I = aV^2 \exp(-b/V) \tag{6-1}$$

where V is the applied voltage, and a and b are constants under practical measurement conditions. In general, b equals $Bd\phi^{3/2}/\beta$, where ϕ is the local work function of the emitter tip, d the separation between the emitter and the anode, B a constant (= 6.53×10^7 V · eV$^{-3/2}$ · cm^{-1}) and β the enhancement factor. β correlates the applied voltage V with the local electric field E$_{loc}$ at the emitting surface by the relation: E$_{loc} = \beta(V/d)$.
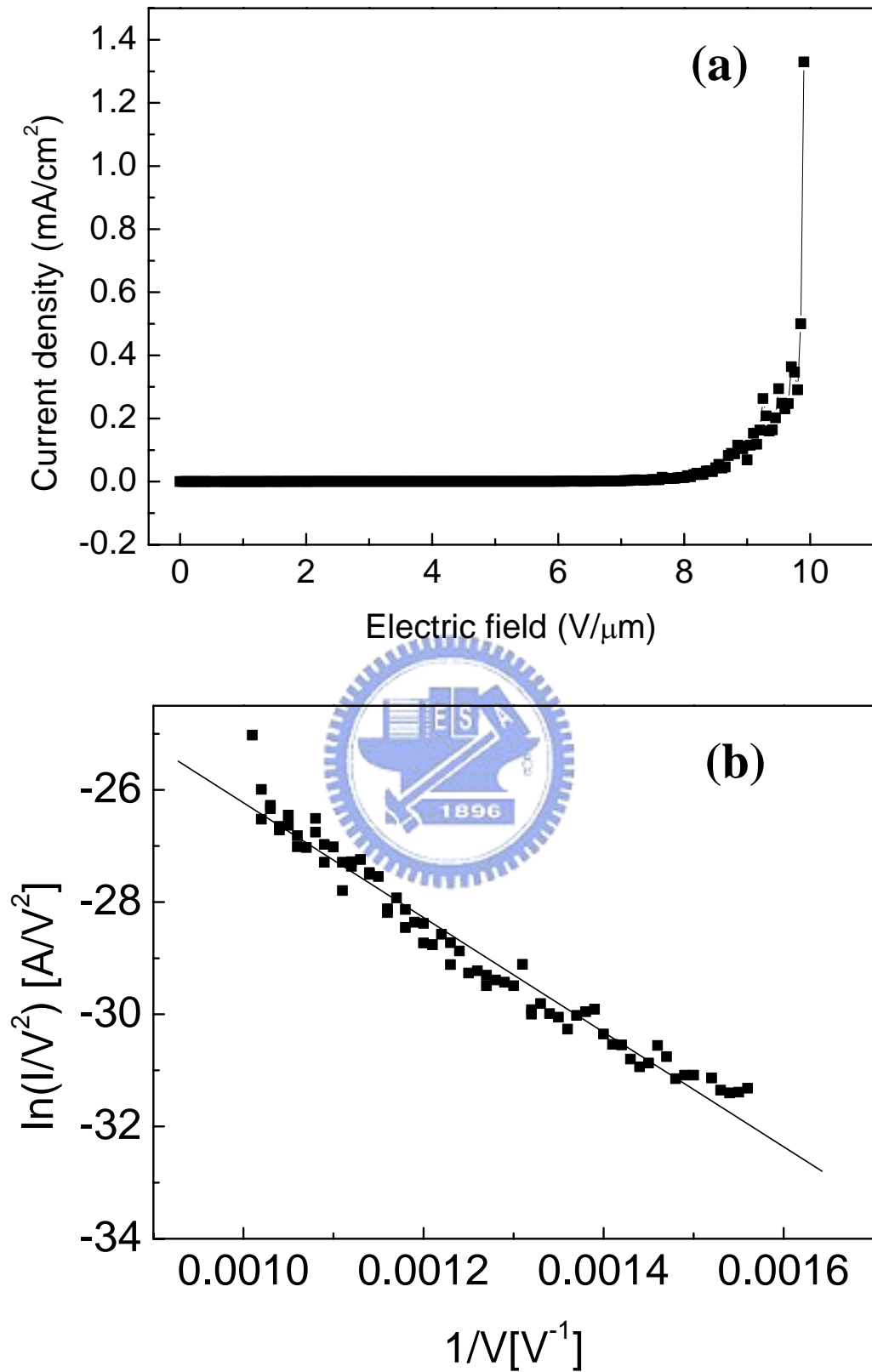
Figure 6-10 shows (a) the J-E curve and (b) the Fowler-Nordheim plot for the α-C coated Si nanotip array.

β is closely related to the geometric shape of the field emitter, and can be approximated by

$$\beta = \frac{d}{kr(d-r)} \qquad (6\text{-}2)$$

where r is the radius of curvature of the tip, and k is a constant depending on the tip geometry [154]. For a simple diode measurement configuration, d is usually much larger than r, i.e., $d \gg r$, and thus β can be approximated as $1/kr$. This suggests that emitters with sharper tips have better field emission characteristics due to the larger β value. Figure 6-10 (a) shows the field emission current density (J) of the α-C coated Si nanotip array as a function of the electric field (E). The F-N plot derived from the J-E curve is shown in Fig. 6-10 (b). The field enhancement factor of a field emitter can be estimated from the slope of the F-N plot and equals $-Bd\phi^{3/2}/\beta$. The slope of the F-N plot in Fig. 8 was -10222, and the β value of the Si nanotip was thus calculated to be 659 by assuming the work function of graphite to be 4.6 eV [170]. The relatively large β value, compared to some previously reported values for Si nanowires, e.g. $\beta = 455$ in reference 159, could be attributed to the sharp tip apex and the high aspect ratio of Si nanotips. Combining with the nanocrystalline graphitic structure of the α-C coating layer, which had a higher electrical conductivity and a lower work function than crystalline silicon, the very sharp tip shape significantly improved the field emission property of the Si nanotip array.

6.5 Summary

Successful fabrication of α-C coated silicon nanotips have been attained by the microwave plasma chemical vapor deposition (MPCVD) with nanoporous AAO as templates. Si nanotips were produced by plasma etch and the α-C layer was in-situ deposited on nanotips under MPCVD process conditions. During the plasma etch, the Si substrate was masked by the well ordered TiO$_x$ nanopillar array formed under the bottom of AAO pore channels and

consequently had a close-packed hexagonal arrangement as the AAO pore channel array. TiO$_x$ nanomasks transferred the hexagonal arrangement pattern to the Si substrate to form the well-ordered Si nanotip array. The in-situ deposited α-C layer on the Si nanotip was rich in nanocrystalline graphitic carbons according to Raman and Auger electron spectroscopies. Due to the sharp geometric feature, the Si nanotip had a large field enhancement factor of 659 and, therefore, exhibited excellent field emission performances.

Chapter 7 Iridium oxide coated Si nanotip arrays

7.1 Introduction

Nanostructured materials usually exhibit interesting physical and chemical characteristics due to the nanometer-scaled dimension as well as the large surface-to-volume ratio and therefore receive extensive studies on a variety of applications of these intriguing properties. One of the most widely studied subjects is the cold-cathode field emission which has many potential technical applications such as field emission flat panel displays, cold-cathode microwave devices and the electron source in x-ray tubes [171]. Nanostructured materials with a small curvature and/or a high aspect ratio can enhance local electric field and greatly improve the field emission efficiency to assure a promising potential for electron field emitters[155-159]. Various nanostructured materials, including carbon nanotubes[172-174], IrO_2 nanorods [100], ZnO nanowires [175,176], Si nanotips [51] and TiN nanorods [177] etc., have been reported to achieve this goal. Although reports on Si nanotips as field emitters are far less in the past decade than such one dimensional nanomaterials as carbon nanotubes, Si nanotips probably pose less difficulty to be integrated into a field emitter device. The crystalline Si has long been used as the starting material to fabricate Spindt-type field emitters because of their excellent electronic mechanical properties and well-developed microfabrication processes. While lithography process may limit the size and density of Si field emitters due to the image resolution of the lithography tool, other preparation methods without photomasking do not usually provide a growth process to regulate the arrangement of nanosized field emitters. TiO_x nanodots are prepared with porous anodic aluminum oxides (AAO) as templates and used as masks to fabricate highly ordered Si nanotips coated with a α-carbon layer [149]. Although the sharp apex of the Si nanotip can greatly enhance the field emission, the Si nanotip has the same disadvantages as most Spindt-type field emitters. The field emission stability of a field emitter with a low work function is very susceptible to

surface changes in chemical state and microstructure, such as surface oxidation and contamination. During the field emission, Si tip field emitters may suffer from plasma damage as well as insulating oxide growth and degrade field emission. Emphasis of this study is laid upon the improvement of field emission properties of field emitters by the electrodeposition of chemically stable iridium oxide IrO_2 nanoparticles on the surface of ordered Si nanotip arrays.

IrO_2 is an electrically conductive oxide with a resistivity of ~39 $\mu\Omega$ cm [108] and thermally stable up to $>$ 600°C depending on the preparation method [107]. Iridium oxide has a relatively low work function of 4.23 eV [178], and has been demonstrated to have better field emission properties than Ir, Mo and W emitters [99]. IrO_2 nanoparticles were deposited on ordered Si nanotips by bipolar galvanostatic pulse electrodeposition. The pulse electrochemical deposition offers many advantages over conventional physical vapor deposition techniques, including simplicity of the experimental setup, low growth temperature and large deposition area. The size and uniformity of nanoparticles can be well controlled by tuning the anodic and cathodic pulse current density and the pulse duration. By increasing the nucleation density and avoiding particle agglomeration, nanosized IrO_2 particles can be uniformly deposited on Si nanotips. Because of the very small curvature, nanoparticles can greatly enhance the local electric field and exhibit better field emission characteristics than bare Si nanotips.

7.2 Fabrication of iridium oxide coated Si nanotip Arrays

The fabrication procedure of ordered Si nanotip arrays has been reported previously [149]. Figure 1 illustrates the fabrication steps of iridium oxide nanoparticle coated Si nanotip arrays. In brief, TiN thin films in 30 nm thickness and Al films in 3 μm thickness were sequentially deposited on 6-inch p-type Si(100) wafers with the resistivity of 0.01 Ω-cm. Anodic oxidation of Al films was carried out in a 0.3M oxalic acid ($H_2C_2O_4$) solution at 25°C,

and thereby the underlying TiN films were partially anodically oxidized under the bottom of AAO pore channels. AAO layers were then removed by wet chemical etch in a solution of 6 wt% H_3PO_4 and 1.5 wt% CrO_3 at 60°C. Exposed TiO_x nanodots were then used as nanomasks to etch the remaining thin TiN layers and the underlying Si substrates in an inductively coupled plasma reactive ion etch (ICP-RIE) system. TiO_x nanodots were subsequently used as nanomasks to etch TiN layer by using the gas mixture of BCl_3 and Cl_2. Working conditions of the RIE process were 400 W plasma power, 100 W substrate bias power, 10 mtorr working pressure and 35 sccm flow of the plasma gas source for 40 sec. The underlying Si substrate uses the gas mixture of SF_6, Cl_2 and O_2 as the plasma source. The RIE process was performed under the following working conditions: plasma power 400 W, substrate bias power 120 W, working pressure 10 mtorr and flow in the plasma gas source for 40 sec at 10, 40 and 5 sccm, respectively. Wet etching is applied to remove silicon oxides in HF, HNO_3 and H_2O so that the volume ratio is 9:6:180 and there appear sharp Si nanotips.

Electrochemical deposition of IrO_2 nanaoparticles on Si nanotips was performed by bipolar galvanostatic pulse electrodeposition in a three electrode cell system with Si nanotips as the working electrode, thin platinum plate as the counter electrode and saturated calomel electrode (SCE) as the reference electrode. The electrodeposition solution was an aqueous solution of $IrCl_4 \cdot H_2O$ (0.3 g in 200 ml H_2O), oxalic acid $H_2C_2O_4 \cdot 2H_2O$ (1g), and H_2O_2 (2 ml). The pH of the solution was adjusted to ~10.5 by the addition of K_2CO_3 [101]. All solutions were prepared in deionized water (>18 MΩ). Before electrodeposition onto Si nanotips, the solution was aged for two days. The pulse electrodeposition of the IrO_2 nanoparticle layer on the Si nanotip array required 75 pulse cycles. After the electrodeposition, nanotips were annealed in oxygen at 600°C for 3hrs.
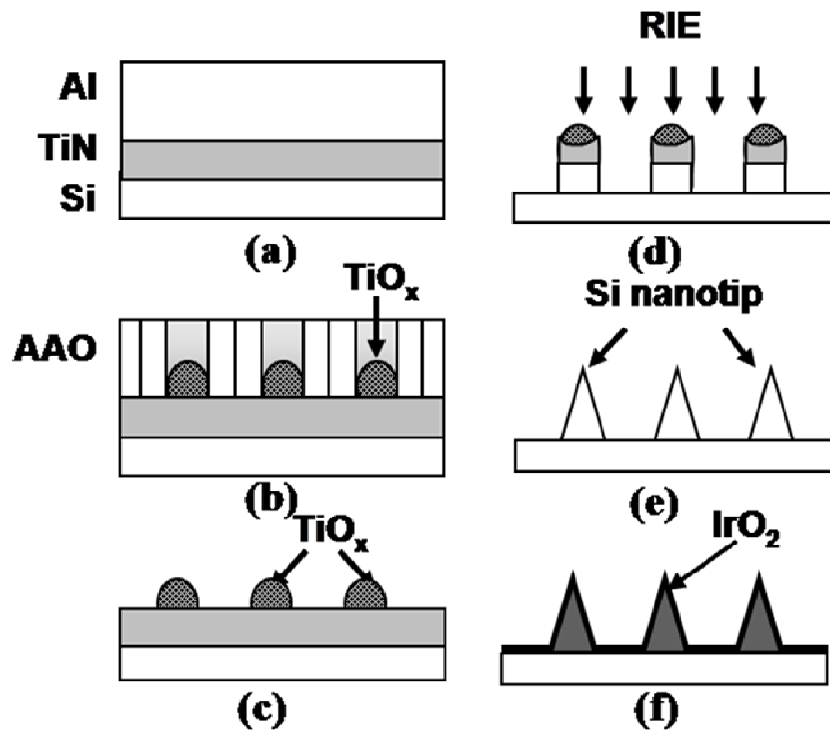
Figure 7-1 shows the fabrication steps of AAO templated Si nanotips with electrodeposited IrO$_2$ nanoparticles. (a) TiN and Al deposition on Si wafers by physical vapor deposition, (b) anodic oxidation of the Al film and formation of TiO$_x$ nanodots, (c) removal of the AAO layer by wet etch, (d) reactive ion etch of the remaining TiN and the Si substrate, (e) formation of Si nanotips and (e) electrodeposition of IrO$_2$ nanoparticles on Si nanotips.

7.3 Characterization of Si nanotips Arrays

Figures 7-2 shows the side-view SEM images of the fabrication of Si nanotip arrays. The side-view SEM image in Fig.7-2 (a) reveals that the TiO$_x$ nanomask arrangement was compliant with the pore arrangement of the AAO template and had a nanomask density of ~1x10^{10} cm^{-2}. To etch the TiN layer, a gas mixture of BCl$_3$ and Cl$_2$ was used as the plasma source in the ICP-RIE system. TiO$_x$ and Si could also be etched by the chorine-based plasma source, but the relatively large height of the TiO$_x$ nanomask provided sufficient masking thickness to the underlying TiN and Si substrate so that the arrangement pattern of nanopillars could be successfully transferred to the Si substrate, as shown in Fig. 7-2 (b).

Gas mixture of Cl_2, SF_6 and O_2 were used as the plasma source to etch Si substrates and form Si nanotips of high aspect ratio, as shown in Fig. 7-2 (c). The Si nanotip array had an ordered hexagonal arrangement as AAO as well. The surface silicon oxide of the Si nanotip was removed by wet etching. Si nanotips were uniform in size and shape as shown in Fig. 7-2 (d). Most Si nanotips had a height of ~200 nm and a base width of 100 nm with an apex angle of ~28°. The geometric shape of nanotips could be tailored by varying the RIE time. As the size and thickness of TiO_x/TiN nanomasks became smaller due to a longer etch time, taller and sharper Si nanotips could be produced.
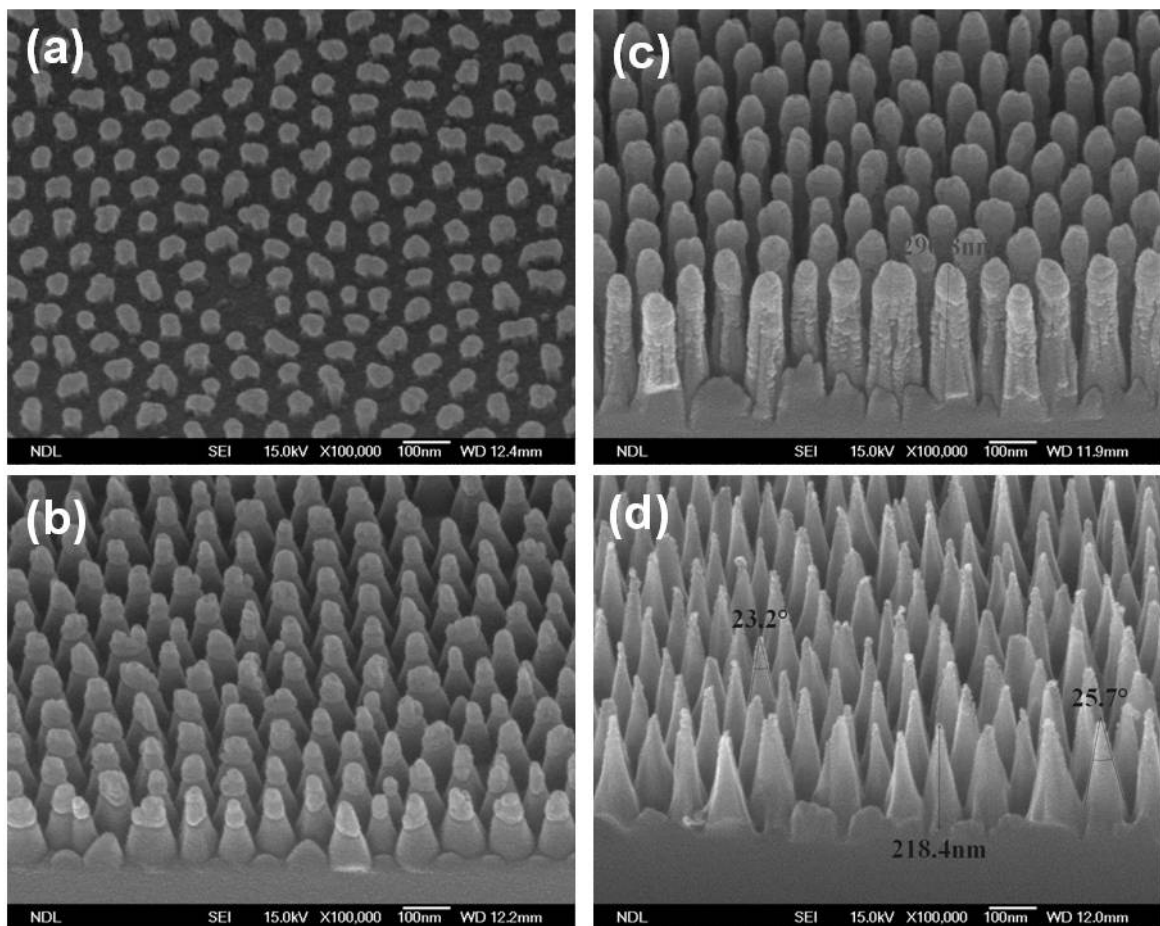
Figure 7-2 shows the fabrication process of Si nanotips (a) TiO_x nanomasks after the removal of the AAO layer by wet etch. (b) the TiO_x/TiN/Si nanocone array after the RIE etch by Cl_2 and BCl_3 for 40 sec. (c) the TiO_x/TiN/Si nanocone array after the RIE etch by SF_6, Cl_2 and O_2 for 40 sec. (d) removal of the oxide layer by wet chemical etch and the formation of sharp Si nanotips.

Before electrodeposition of IrO$_2$ on Si nanotips, confirmation of complete removal of silicon oxides on the Si nanotip surface is necessary. Figure 7-3 shows the XPS silicon *2p* spectra in each fabrication step. After wet etching, silicon oxides on the Si nanotip surface were completely removed. Electrochemical deposition is related to the constituent, concentration, temperature and pH value of the electrolyte. Yamanaka recipe to prepare IrO$_2$ electrolyte suggested that IrO$_2$ was insoluble in alkaline solutions and its electrodeposition rate increased as the increase of pH value [101]. Previous studies revealed that before electrodeposition, the solution was aged for several days [97,102]. Figure 7-4 shows the UV-visible absorption spectral change of the electrolyte at pH~10.5. The fresh solution
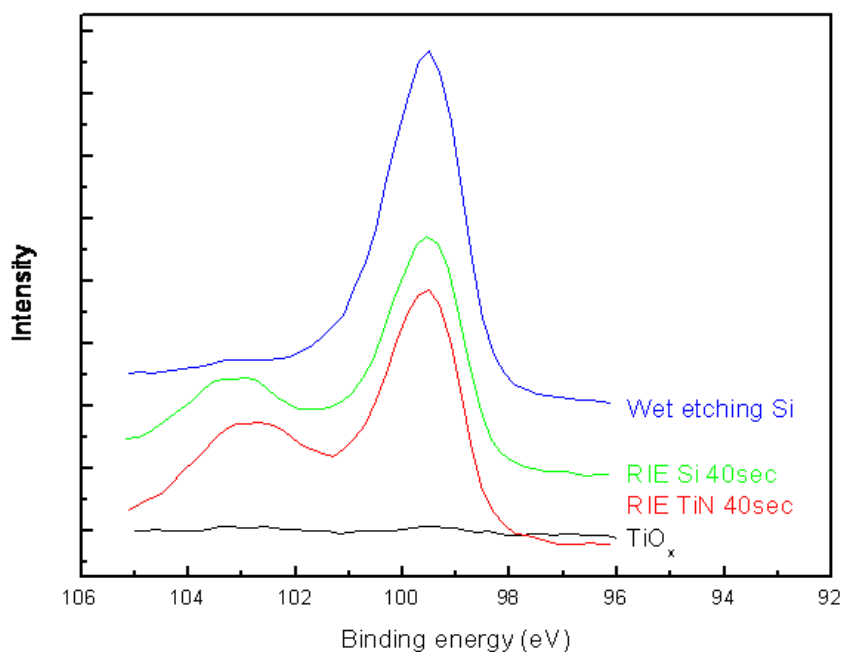
Figure 7-3   XPS silicon *2p* spectra in each fabrication step.
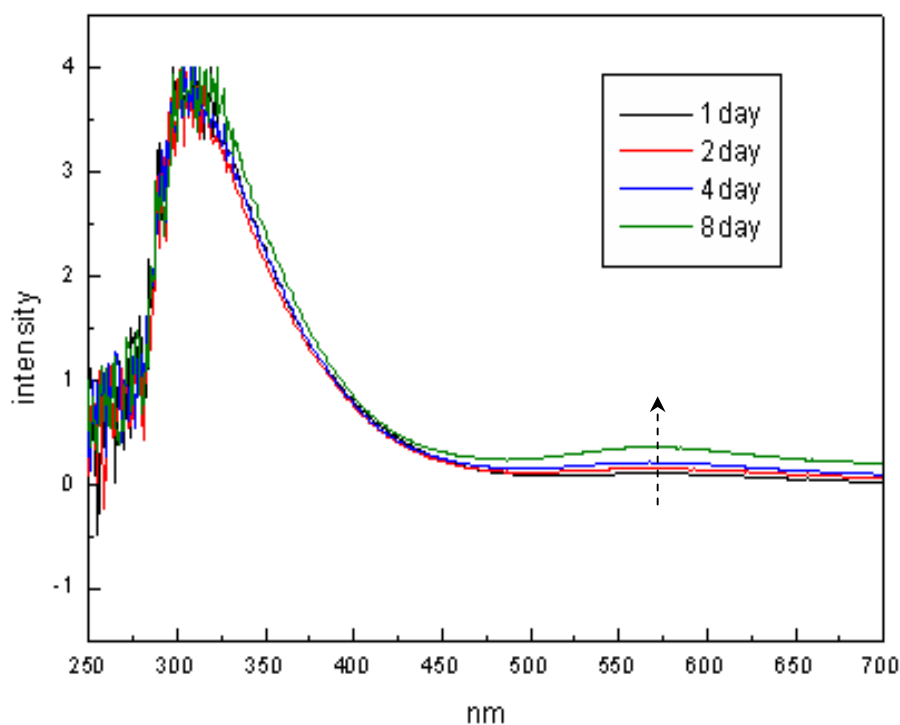
Figure 7-4 UV-visible absorption spectral change of the electrolyte at pH~10.5.

exhibited obvious absorption maximums at k_{max} = 318 nm. As aging time went on, the absorbance at 318 nm grew up and an absorption band at 570 nm appeared to give a blue solution. After aging for 8 days, absorbance increases at 318 and 570 nm were saturated to 3.91 and 0.35, respectively and provided the stable blue solution. The absorption band at 570 nm in the present solution suggests the formation of IrO_2 colloids by solution aging.

7.4 Characterization of iridium oxide coated Si nanotip Arrays

During the electrodeposition, oxalate ligands complexed with iridium ions can be easily oxidized in the basic solution, decompose into CO_2 and leave insoluble iridium oxide precipitate on the anode [102]. In the bipolar pulse electrodeposition, iridium oxide was

deposited on Si nanotips during the anodic current pulse and dissolved from nanotips during the cathodic current pulse. Pulse electrodeposition could be distinguished in three types, as shown in Fig. 7-5. Under the pulse electrodeposition condition, the size distribution and thickness of the deposited nanoparticle layer is less susceptible to variations of the anode surface geometric structure. Because Si nanotips were highly ordered, the current density distribution was uniform over the anode surface and led to the deposition of a conformal iridium oxide layer with a uniform particle size distribution.
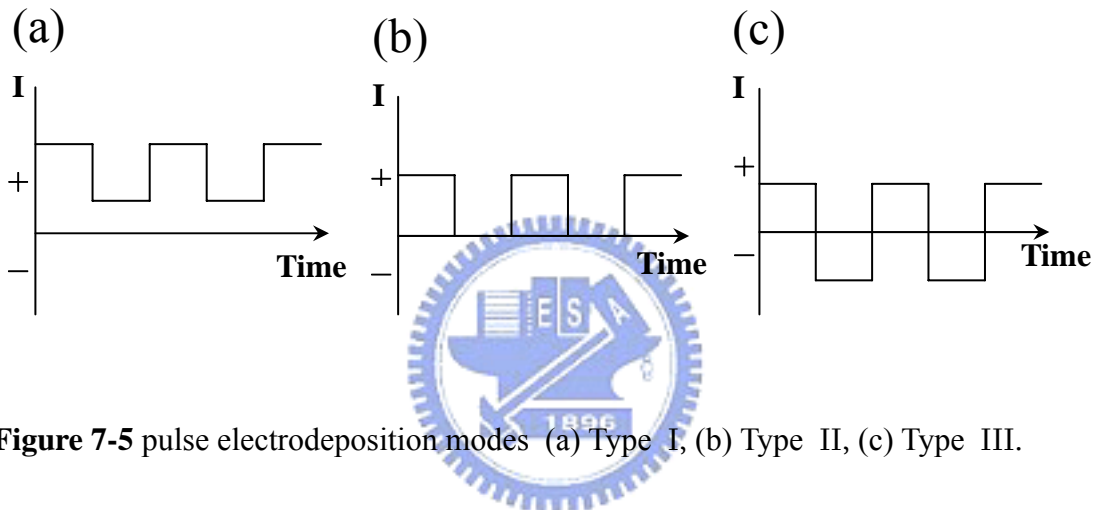
Figure 7-5 pulse electrodeposition modes (a) Type I, (b) Type II, (c) Type III.

Table 7-1 presents the pulse electrodeposition parameters of *Type I*. Variable deposition conditions such as deposition time or deposition frequency bring about evident changes in the basic surface morphology. SEM images in Fig.7-6 clearly tell that the pulse electrodeposited nanoparticle layer of *Type I* deposits on Si nanotips with particle accumulation on the tip apex. The current as the variable in deposition time or deposition frequency is fixed at I_1=0.7 mA and I_2=0.5 mA. Figure 7-6 (a), (b) and (c) correspond to the condition (1) of the sample (1), the condition (2) of the sample (2) and the condition (3) of the sample (3), respectively. It is obvious from Fig.7-6 (a) and (b) that the electrodeposited IrO_X nanoparticle layer thickness is directly proportional to the increasing deposition time. IrO_X nanoparticles are accumulated on Si nanotip apex and modify the original Si nanotip shape. The Si nanotip shape has local field on the apex and gives rise to a higher deposition rate. Nanotips become blunter with

deposition time. Si nanotips shown in Fig.7-6 (b) and (c) were prepared with different pulse current frequency. According to the morphology of these two tip arrays, pulse current frequency is found to control the nucleation rate. Lower pulse current frequency brings about higher nucleation rate and results in finer crystal grains. The finer crystal grain with smaller curvature of nanotip radius could be captured on Si nanotip apex because the lower the pulse current frequency, the lower the iridium ions oxidized rate and the lower deposition rate. Deposition rate in Figure 7-6 (b) is lower than that in Figure 7-6 (c). Revealed in Table 7-2 are pulse electrodeposition parameters of *Type III*. The experimental parameter is correlated with the current amplitude, the pulse current frequency and the duration time of the anode pulse current. Figure 7-7 presents SEM images of IrOx nanoparticles pulse electrodeposited on Si nanotips by the *Type III* mode. Figure 7-7 (a) displays the condition (4) of the sample (4). There is no IrO_X nanoparticle agglomeration on the nanotip apex as shown in the SEM image. Figure 7-7 (b) shows the condition (5) of the sample (5). No IrO_X nanoparticle agglomeration appear on the nanotip apex by the pulse-current amplitude (I_1= 0.5 mA, I_2= - 0.1 mA), as shown in the SEM image. Figure 7-7 (c) illustrates the condition (6) of the sample (6). The electrochemical deposition of IrO_X nanoparticles onto the nanotip surfaces proceeds through the nucleation of IrO_X clusters and the subsequent film growth. The overpotential that is partitioned across the space charge layer and the Helmholtz layer must be overcome. IrO_X nanoparticles appear on nanotips at the pulse current amplitude (I_1= 0.7 mA, I_2= - 0.1 mA). Figure 7-7 (d) shows the condition (7) of the sample (7). The deposition condition is I_1 = 0.7 mA and I_2 = -0.1 mA with the fixed duration time of 0.1 sec. The frequency in condition (7) is 10 times that in condition (6). The SEM image in Fig 7-7 (d) demonstrates that the deposition layer is fully captured on the Si nanotip. Long duration benefits nanoparticle grain growth.

Table 7-1 pulse electrodeposition parameters of *Type I.*

IrO$_x$	(1)	(2)	(3)
I$_1$ (mA)	0.7		
I$_2$ (mA)	0.5		
t$_1$ (sec)	0.2	0.2	0.02
t$_2$ (sec)	0.1	0.1	0.01
Total time (sec)	200	300	300
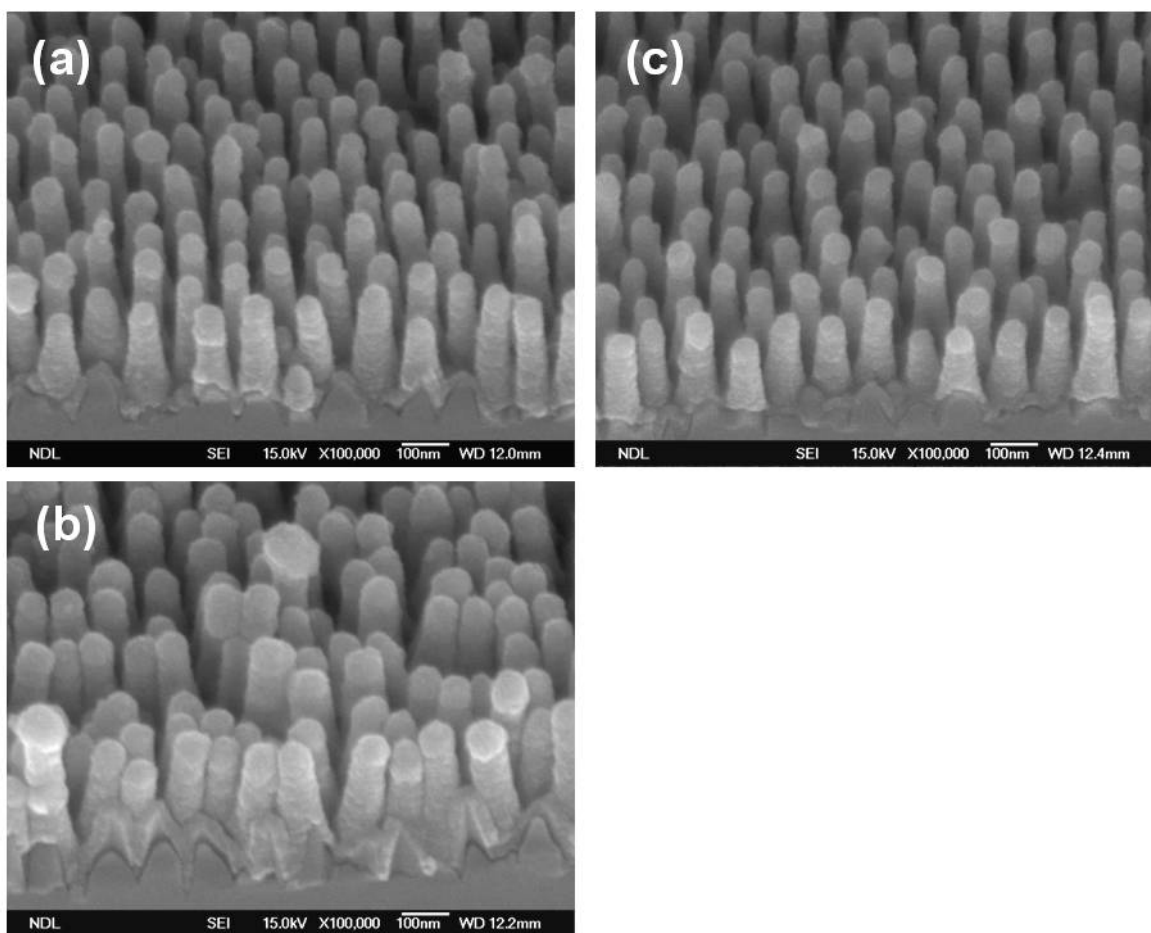
Figure 7-6 SEM images of the pulse electrodeposited nanoparticle layers   (a) side view of the sample (1) in the condition (1),   (b) side view of the sample (2) in the condition (2) and (c) side view of the sample (3) in the condition (3).

Table 7-2 pulse electrodeposition parameters of *Type III.*

IrO_x	(4)	(5)	(6)	(7)	(8)
I_1 (mA)	0.3	0.5	0.7	0.7	0.7
I_2 (mA)	-0.1				
t_1 (sec)	0.01			0.1	0.04
t_2 (sec)	0.01			0.1	0.01
Total time (sec)	300				

Curvature radius of sample (7) is larger than that of sample (6). Figure 7-7 (e) shows the condition (8) of the sample (8). The deposition condition is I_1 = 0.7 mA and I_2 = -0.1 mA. The duration time at anode is 4 times that in condition (6). Si nanotips are obviously capped by the thick layer. Figure 7-8 is the TEM image of IrO_2/Si nanotips in condition (6). Clearly shown in the TEM image is that nanoparticles are below ~5 nm, well dispersed on Si nanotips and uniform in particle size distribution. Agglomeration of nanoparticles is not obvious even at the nanotip apex.

Figure 7-9 shows the XPS spectrum of nanoparticle coated Si nanotips annealed in oxygen ambient at 600^oC for 3hr. The XPS peak of the Ir ($4f_{7/2}$) electron is situated at 62.0 eV as shown in the inset of Fig. 7-9, and the peak site was found to be independent of the electrode potential. The positive binding energy shift of 1.1 eV of metallic Ir (60.9 eV) indicated the presence of IrO_2 on nanotips[179]. Si(2p) and Si(2s) signals clearly observed in the wide scan suggested that the IrO_2 nanoparticle layer was likely thinner than the escape depth of photoelectrons, which is typically below ~5 nm, and/or some area of Si nanotips was not covered by nanoparticles. This presence of crystalline IrO_2 particle was confirmed by glancing angle X-ray diffractometry and TEM study.
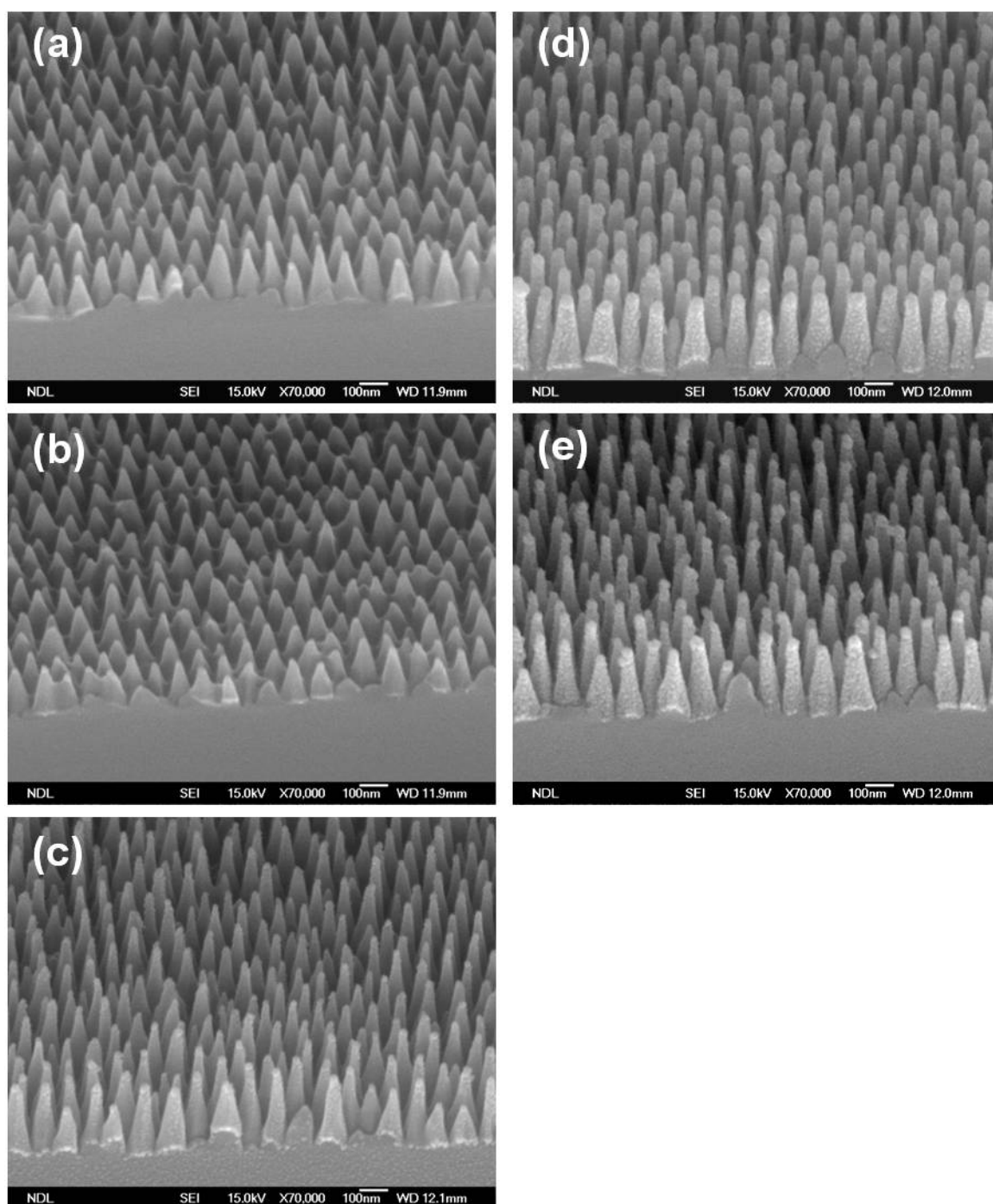
Figure 7-7 shows SEM images of pulse electrodeposited nanoparticle layers.　(a) side view of sample (4) in condition (4),　(b) side view of sample (5) in condition (5), (c) side view of sample (6) in condition (6), (d) side view of sample (7) in condition (7) and (e) side view of sample (8) in condition (8).

The XRD spectrum in Fig.7-10 shows three reflection peaks indexed as (110), (101) and (200) for the tetragonal IrO_2 lattice structure. Figure 7-11(a) is a TEM image of two Si nanotips after the anneal treatment at 600^0C in condition (6). The TEM image clearly indicates that nanoparticles are well dispersed on the Si nanotip and have a uniform particle size distribution smaller than ~5 nm. The inset of Fig. 7-11(a) is the selected area diffraction (SAD) pattern of the Si nanotip. Two diffraction rings are indexed as (110) and (101) lattice orientations of the IrO_2 tetragonal lattice structure. The high resolution TEM lattice image of the apex of a Si nanotip is shown in Fig.7-11(b). The fringe spacings of two nanocrystals are estimated to be 2.53 Å and 2.24 Å, which correspondrd to (101) and (200) lattice orientations of the IrO_2 crystal, respectively, and manifest the presence of IrO_2 nanoparticles on the tip apex, which is the prevailing emitting site during electron field emission.
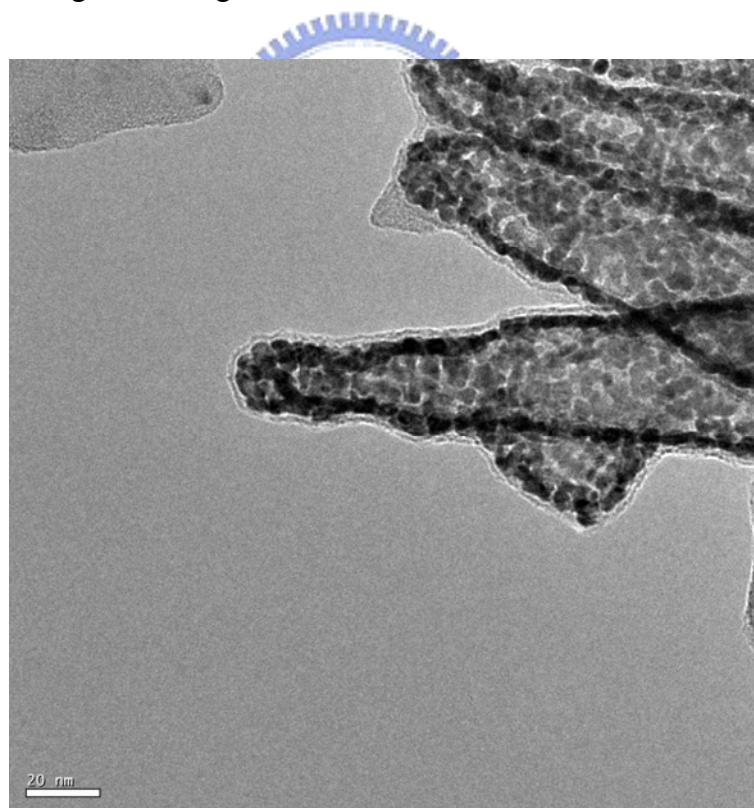
Figure 7-8 TEM image of the IrO_2/Si nanotip just deposited.
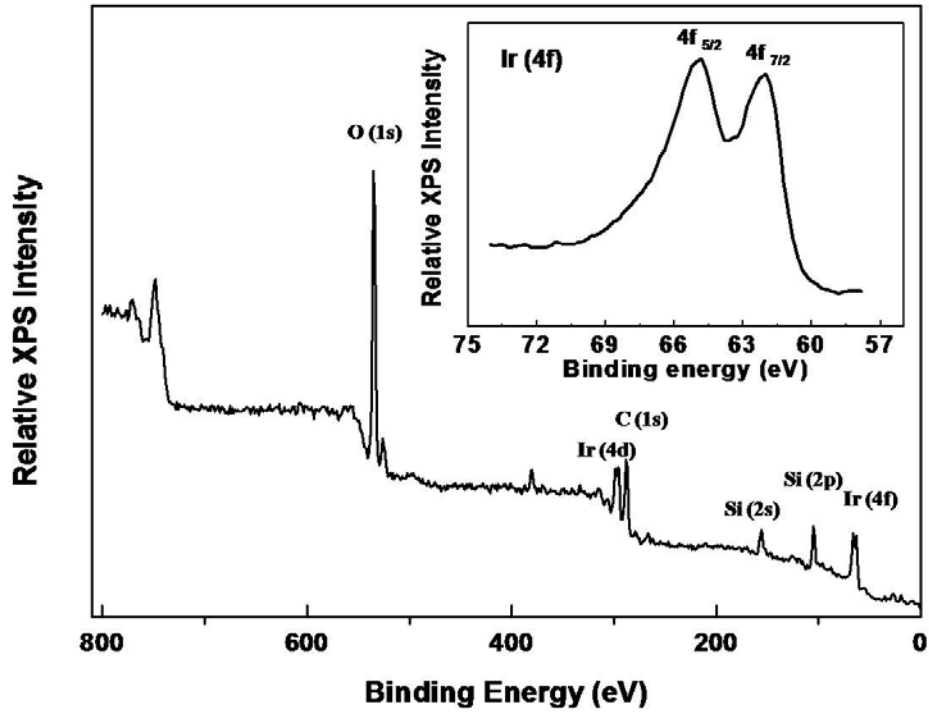
Figure 7-9 shows the XPS spectrum of the IrO$_2$/Si nanotip after the anneal treatment at 600°C in oxygen ambient for 3 hrs. The inset shows the energy window of Ir(4f) electrons.
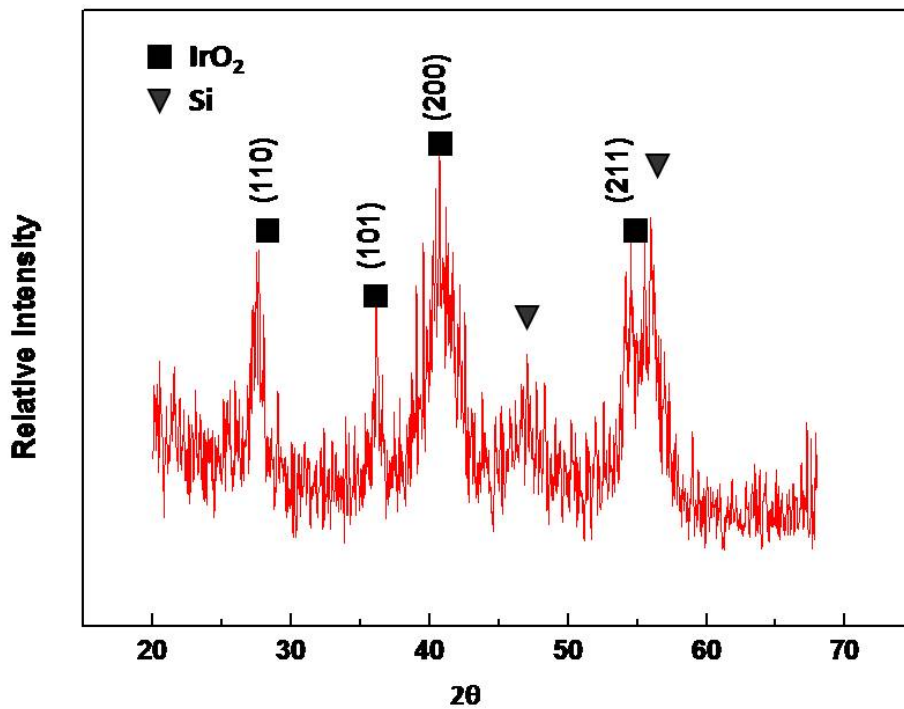
Figure 7-10 shows the glancing angel XRD spectrum of the IrO$_2$/Si nanotip array after the anneal treatment at 600°C.
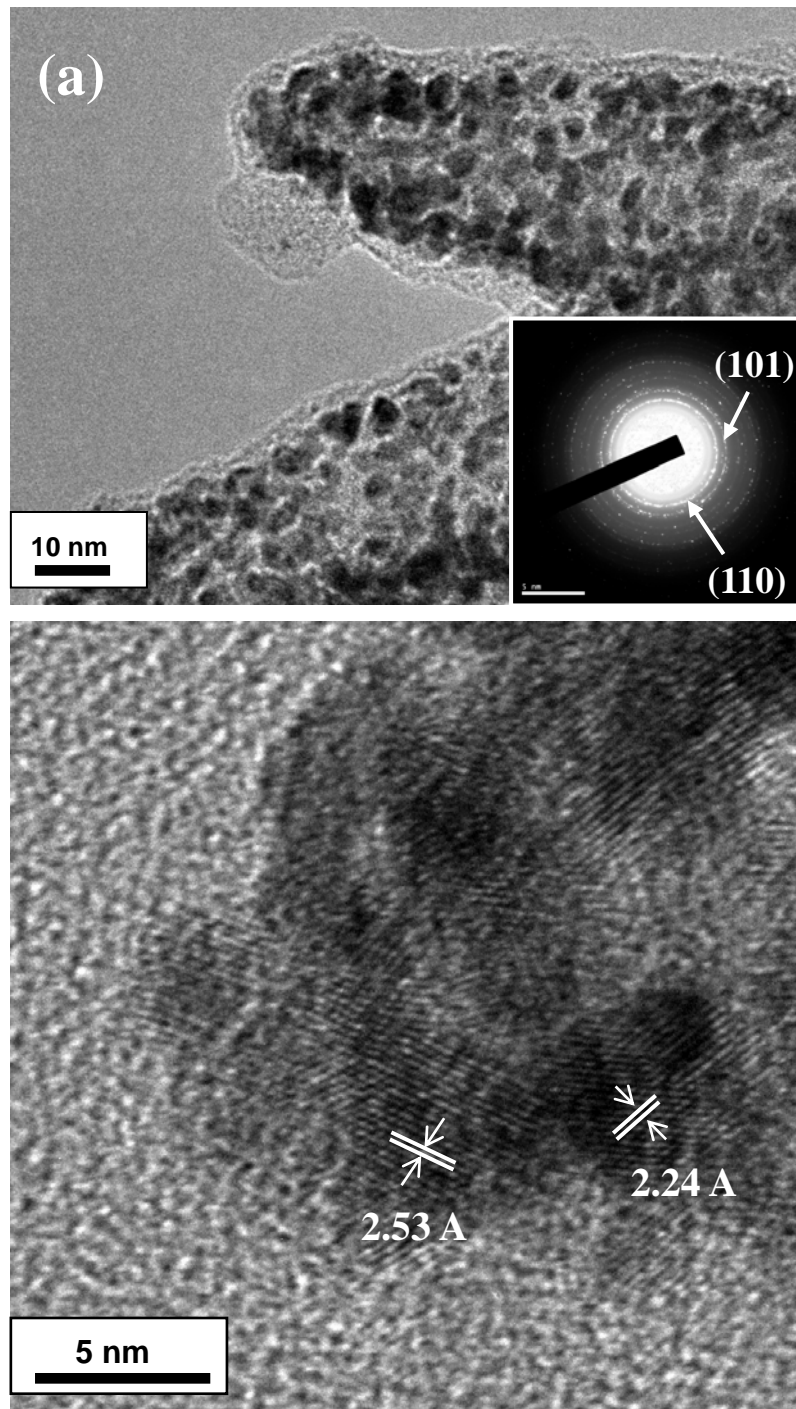
Figure 7-11 shows (a) TEM image of the IrO$_2$/Si nanotip in which the inset reveals the selected area diffraction (SAD) pattern of the nanotip and (b) HRTEM image of the tip apex of the upper nanotip shown in Fig. (a).

7.5 Field emission characteristic of iridium oxide coated Si nanotip arrays

IrO_2 nanoparticles on Si nanotips can significantly improve field emission characteristics of nanotips. Figure 7-12 (a) illustrates plots of field emission current density versus applied field (J-E) for Si nanotips with and without electrodeposited IrO_2 nanoparticles. J-E plots clearly demonstrate the superiority of IrO_2/Si nanotips on the field emission performance over bare Si nanotips.

Based on the Fowler-Nordheim (F-N) field emission theory, the field emission current density is related to the applied field by the following equation [180]:

$$J = A(\beta E)^2 \exp(-B\phi^{3/2}/\beta E) \tag{7-1}$$

where J is the current density in A/m^2, ϕ the work function of the emitter in eV, E the applied field of the flat-capacitor geometry in V/m and β the field enhancement factor. A is a function of ϕ and B is typically a constant for a given field emission measurement. The local electric field E_T at the emitting site can be correlated with the applied field E by the relation: $E_T = \beta E = \beta (V/d)$, where d is the separation between the cathode and the anode and V is the biased voltage. β is closely related to the geometric shape of the field emitting site. In general, field emitters with a small tip radius and a high aspect ratio have a high field enhancement factor. The corresponding Fowler-Nordheim (F-N) plots, which delineate the dependence of $\ln(J/E)$ on $1/E$, are shown in Fig. 7-12(b). The F-N slopes for the bare Si nanotip and the IrO_2/Si nanotip are estimated to be ~-616 and ~-445, respectively. According to Eq. (1), the F-N slope equals $-B\phi^{3/2}/\beta$, with $B = 6.53 \times 10^9$ (V $eV^{-3/2}$ m^{-1}). The β values of bare Si nanotips and IrO_2/Si nanotips are thus calculated to be ~84 and ~128, respectively, by assuming a work function of 4.6 eV for Si [181] and 4.23 eV for IrO_2 [178]. The very large β value of both emitters is certainly due to the sharp apex of nanotips. An increase in the field enhancement factor by 52% as IrO_2 nanoparticles were deposited on Si nanotips can be ascribed to the geometric
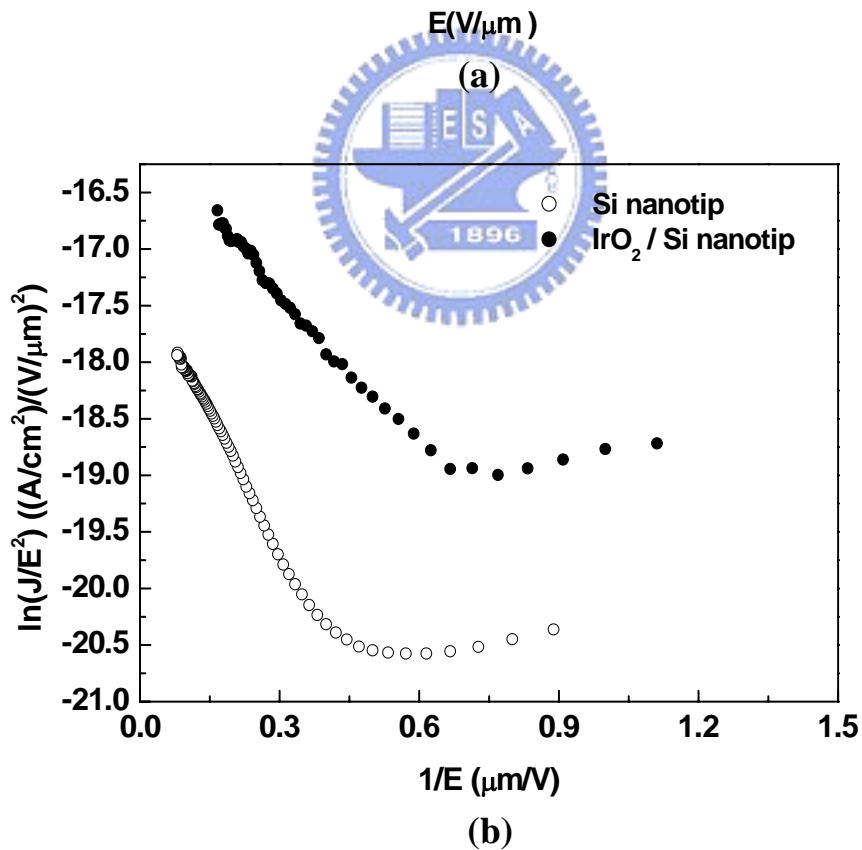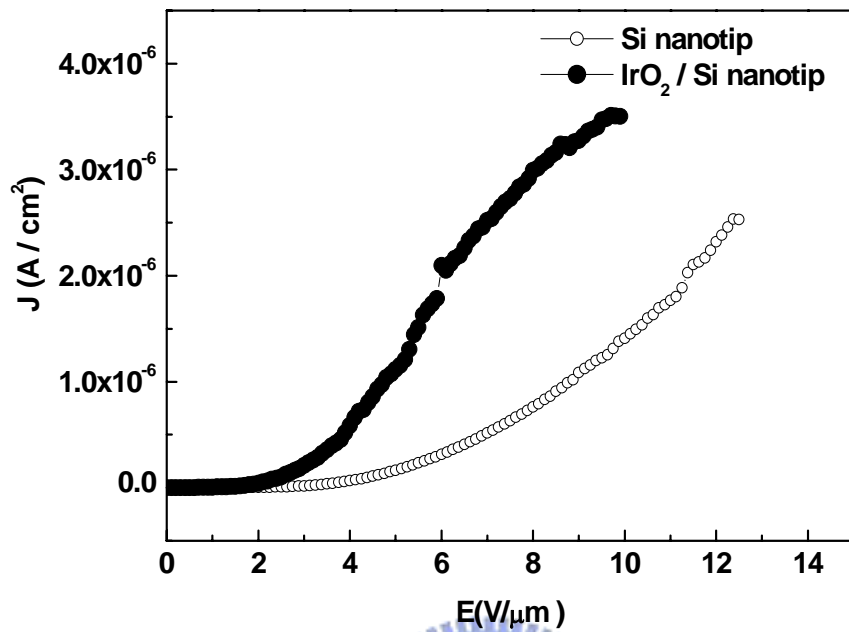
Figure 7-12 shows (a) J-E curve of Si nanotips and IrO_2/Si nanotip array; (b) the corresponding F-N plot of the J-E curve.
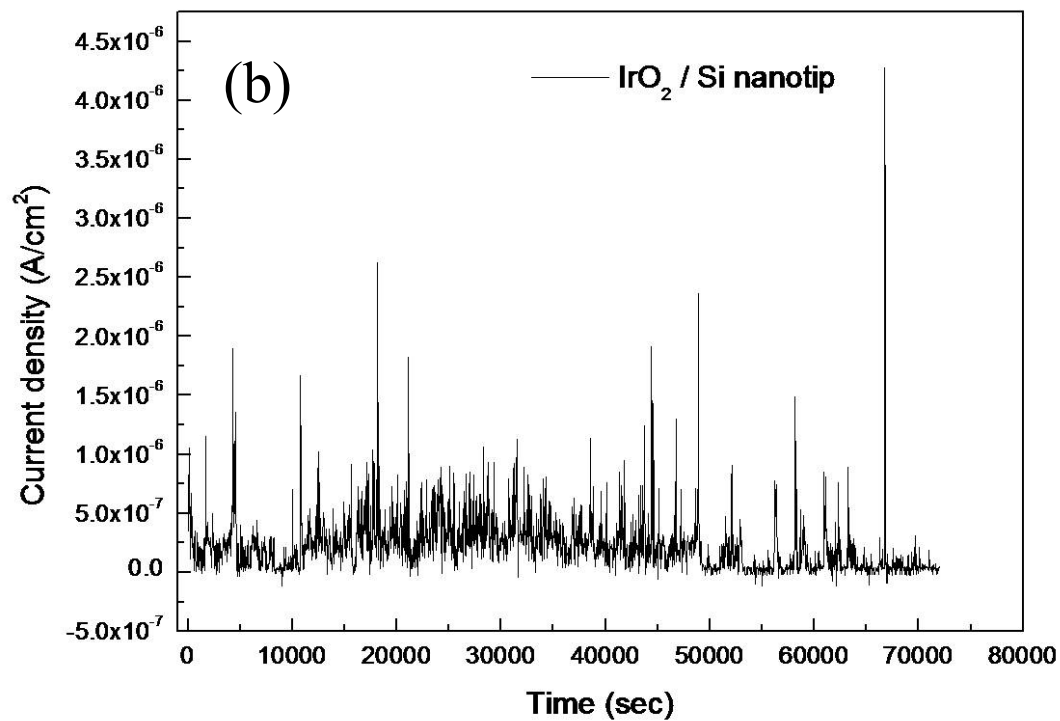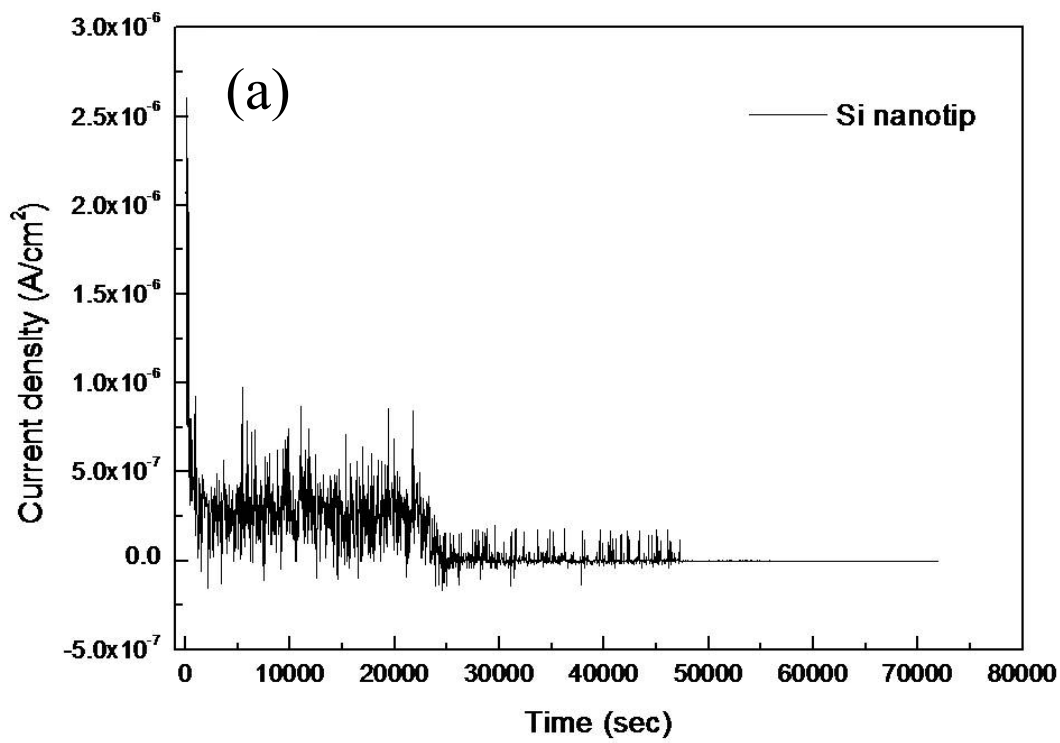
Figure 7-13 Emission current stability of field emitter arrays (a) Si nanotip (b) IrO$_2$/Si nanotip

modification of Si nanotips by nanoparticles. IrO_2 nanoparticles are smaller in curvature than the apex of Si nanotips and can consequently enhance the local electric field at the apex to improve the field emission efficiency of the nanotip emitter. Moreover, IrO_2 has a work function lower than Si, and therefore IrO_2 nanoparticles should produce more field emission current than bare Si nanotips even if the difference of field enhancement factors is ignored. With the two improvement factors of small curvature and low work function of IrO_2 nanoparticles, IrO_2/Si nanotips are superior to bare Si nanotips in field emission characteristics. The turn-on field of IrO_2/Si nanotips, herein defined as the field at the intersection of the two straight lines extrapolated separately from the linear rising segment and the background, is determined to be 1.5 V/μm, while it is 2.0 V/μm for bare Si nanotips. At the electric field of 5 V/μm, IrO_2/Si nanotip emitters have a field emission current density of 1.13×10^{-6} A/cm^2, which is about seven times that of bare Si nanotips. Si and Si/ IrO_2 nanoemitters were operated under ultrahigh vacuum for extended periods of time, respectively. After 20 h of operation under a continuously applied field at the pressure of ~5×10^{-6} torr, IrO_2/Si tips show degradation at 15 h as indicated in Fig.7-13(b). IrO_2/Si tips confirm higher stability than Si nanotips during extended periods of operation under ultrahigh vacuum. Field emitter arrays of stable conductive IrO_2 oxides will definitely improve the overall reliability of commercial vacuum microelectronic devices.

7.6 Summary

Fabricated successfully were highly ordered Si nanotips by the AAO templation and electrodeposited IrO_2 nanoparticles on Si nanotip arrays by the bipolar pulse electrodeposition. The pulse electrodeposition leads to the formation of a conformal IrO_2 nanoparticle layer on ordered Si nanotips. IrO_2 nanoparticles have a uniform size distribution below 5 nm. IrO_2/Si nanotips have a lower turn-on field of 1.5V/μm and a larger field enhancement factor

compared with bare Si nanotips. The superior field emission performances of IrO_2/Si nanotips are ascribed to the small curvature and the lower work function of IrO_2 nanoparticles. IrO_2/Si tips show higher stability than Si nanotips during extended periods of operation under ultrahigh vacuum.

Chapter 8

Conclusions and future works

8.1 Conclusions

In this study, ordered arrays of nanostructures including TiN nanopillar, Si nanotip, α -C/Si nanotip, IrO_2/Si nanotip are successfully fabricate by using the nanopores of anodic aluminum oxide (AAO) films as templates. Ordered nanomask arrays of titanium oxides are constructed by anodizing the Al/TiN bilayered films. The TiO_X nanodots were then used as the nanomask for etching the TiN layer and the underlying layer in an inductively coupled plasma reactive ion etch (ICP-RIE) system. The field emission characteristics as well as field emitter applications of the nanostructures have been investigated. The primary results obtained in this thesis are summarized as follows:

(1) The aluminum film was introduced to produce the nanoporous AAO film with hexagonally arranged nanopores. The pore arrangements show with ordered domains in the diameters of a few micrometers. By tuning the anodic voltage, the nanodots have a uniform size distribution with a diameter of about 30 to 60 nm and an interdots distance of about 50 to 100 nm can be obtained.

(2) Combining reactive ion etching, we have fabricated well ordered TiN nanorods on the Si substrate using TiO_x nanodots as the mask, which was prepared by AAO templation method. Removal of the TiO_x nanomask left a concaved top surface on the TiN nanorod. The protruding edge on the top surface of the TiN nanorod resulted in nonlinear Fowler-Nordheim field emission characteristics with a low turn-on field of 1.6V/μm. The top edge of the nanorods locally enhanced the electric field by a factor of ~4.6 and thereby decreased the turn-on field. The elliptical wedge cylinder model was used to

estimate the local field enhancement factor of the protruding edge, and an underestimation by ~26% was found as compared with the one derived from the F-N plot. The underestimation was ascribed to a large variation in geometric structure of the nanorods and the non-ideal elliptical wedge shape of the protruding edge.

(3) The α-C coated silicon nanotips by microwave plasma chemical vapor deposition using nanoporous AAO as a template was successfully in our study. The Si nanotips were produced by plasma etch and the α-C layer was in-situ deposited on the nanotips under the MPCVD process conditions. During the plasma etch, the Si substrate was masked by the well ordered TiO_x nanopillar array, which was formed under the bottom of AAO pore channels and thus had a close-packed hexagonal arrangement as the AAO pore channel array. The TiO_x nanomasks transferred the hexagonal arrangement pattern to the Si substrate leading to the formation of the well-ordered Si nanotip array. The in-situ deposited α-C layer on the Si nanotip was rich in nanocrystalline graphitic carbons. Due to the sharp geometric feature, the Si nanotip had a large field enhancement factor of 659 and turn-on field of 6.25V/μm.

(4) We have fabricated highly ordered Si nanotips using AAO templation method, and electrodeposited IrO_2 nanoparticles on the Si nanotip array by bipolar pulse electrodeposition. The pulse electrodeposition led to the formation of a conformal IrO_2 nanoparticle layer on the ordered Si nanotips. The IrO_2 nanoparticles had a uniform size distribution of < 5 nm. The IrO_2/Si nanotip had a lower turn-on field of 1.5V/μm and a larger field enhancement factor compared with the bare Si nanotip. The better field emission performance of the IrO_2/Si nanotip was ascribed to the small curvature and a lower work function of the IrO_2 nanoparticles. The β values of the bare Si nanotips and the IrO_2/Si nanotip were thus calculated to be ~84 and ~128, respectively. IrO_2/Si tips

show better stability than Si nanotips during extended periods of operation under ultrahigh vacuum conditions.

(5) Comparison between nanostructured emitters including TiN nanopillar, α-C/Si nanotip, and IrO_2/Si showed nanotip that the turn on field increased in the order : IrO_2/Si nanotip＜ TiN nanopillar＜α-C/Si nanotip. The large β value of the emitters was certainly due to the sharp apex and high aspect ratio of the nanotips. The IrO_2 nanoparticles had a uniform size distribution of < 5 nm is smallest curvature radius in all of the emitters. The IrO_2 nanoparticles on the Si nanotip had a smaller curvature than the apex of the bare Si nanotip, it could more effectively enhance local electric field at the apex and thus improve the field emission efficiency of the nanotip emitter.

8.2 Future Works

We have shown that anodic aluminum oxide (AAO) is an ideal template material for preparing ordered arrays of the nanostructure. The obtained nanoemitter arrays are highly promising for electron field emission applications. However, some subjects should be further studied:

1. Tuning the field emitters density to avoid the screen effect for better field emission property.

2. Investigations of other emitter materials, such as PdO, electrodeposited onto nanostructures that has produced intriguing improvements in emission performance.

3. Fabrication of a triode-type field emission device that field emitters formed by AAO templated. The fabrication process is an easily controllable and integrated circuit (IC) technology compatible process.

4. Self-organized ordered arrays of the nanostructure should be further studied, which is scientific importance and technological significance of future applications other than field emission, such as fuel cell, solar cell, and gas sensor.
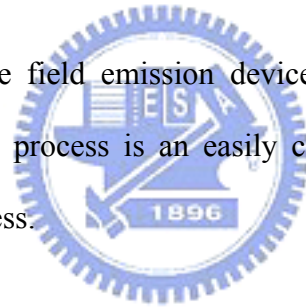
Reference

[1]   C. H. Bennett and D. P. DiVincenzo, Nature, 404 (2000) 247, "Quantum information and computation".

[2]   D. Gammon, Nature, 405 (2000) 899, "Semiconductor physics: Electrons in artificial atoms".

[3]   P. G. Collins, M. S. Arnold, and P. Avouris, Science 292 (2001) 706, "Engineering carbon nanotubes and nanotube circuits using electrical breakdown".

[4]   S. Frank, P. Poncharal, Z. L.Wang, andW. A. de Heer, Science 280 (1998) 1744, "Carbon nanotube quantum resistors".

[5]   T. Rueckes, K. Kim, E. Joselevich, G. Y. Tseng, C.-L. Cheung, and C. M. Lieber, Science, 289 (2000) 94, "Carbon nanotube-based nonvolatile random access memory for molecular computing".

[6]   A. I. Vorobyova, E. A. Outkina, and A. A. Khodin, Russian Microelectronics, 36 (2007) 384 "Self-Organized Growth Mechanism for Porous Aluminum Anodic Oxide".

[7]   Y. C. Sui, D. R. Acosta, J. A. González-León, A. Bermúdez, J. Feuchtwanger, B. Z. Cui, J. O. Flores, and J. M. Saniger, J. Phys. Chem. B 105 (2001) 1523 , "Structure, Thermal Stability, and Deformation of Multibranched Carbon Nanotubes Synthesized by CVD in the AAO Template".

[8]   H. Masuda, M. Yotsuky and M. Ishida, Jpn. J. Appl. Phys. 37 (1998) L1090, "Spatially Selective Metal Deposition into a Hole-Array Structure of Anodic Porous Alumina Using a Microelectrode".

[9]   T. Gao, J. C. Fan, G. W. Meng, Z. Q. Chu and L. D. Zhang, Thin Solid Films 401 (2001) 102, "Thin Au film with highly ordered arrays of hemispherical dots".

[10]   Kyungtae Kim and Sung M. Cho, Sensors Proceedings of IEEE, 2 (2004) 705, "Pd nanowire sensors for hydrogen detection".

[11] O. Jessensky, F. MÜ ller, Applied Physics Letters 72 (1998) 1173, "Self-organized formation of hexagonal pore arrays in anodic alumina".

[12] A. P. Li *et al*., J. Appl. Phys. 84 (1998) 6023, "Hexagonal pore arrays with a 50–420 nm interpore distance formed by self-organization in anodic alumina".

[13] F. Li, L. Zhang, and R. M. Metzger, Chem. Mater. 10 (1998) 2470, "On the Growth of Highly Ordered Pores in Anodized Aluminum Oxide".

[14] V. Sadasivan, C. P. Richter, L. Menon, and P. F. Williams, AIChE Journal 51 (2005) 649, "Electrochemical Self-Assembly of Porous Alumina Templates".

[15] Hideki Masuda, Kenji Fukuda, Science 268 (1995) 1466, "Ordered Metal Nanohole Arrays Made by a Two-Step Replication of Honeycomb Structures of Anodic Alumina".

[16] Sunil Kumar Thamida and Hsueh-Chia Chang, Chaos 12 (2002) 240, "Nanoscale pore formation dynamics during aluminum anodization".

[17] H. Masuda, F. Hasegwa, and S. Ono, J. Electrochem. Soc. 144 (1997) L127, "Self-Ordering of Cell Arrangement of Anodic Porous Alumina Formed in Sulfuric Acid Solution".

[18] H. Masuda, K. Yada, and A. Osaka, Jpn. J. Appl. Phys., Part2 37 (1998) L1340, "Self-Ordering of Cell Configuration of Anodic Porous Alumina with Large-Size Pores in Phosphoric Acid Solution".

[19] A. P. Li, F. Müller, A. Birner, K. Nielsch, and U. Gösele, J. Appl. Phys. 84 (1998) 6023, "Hexagonal pore arrays with a 50–420 nm interpore distance formed by self-organization in anodic alumina".

[20] Jung Sang Suh, Kwang Seok Jeong, Jin Seung Lee, and Intaek Han, Applied Physics Letters 80 (2002) 2392, "Study of the field-screening effect of highly ordered carbon nanotube arrays".

[21] Liu, S. M., L. M. Gan, L. H. Liu, W. D. Zhang, and H. C. Zeng, Chem. Mater. 14 (2002) 1391, "Synthesis of single-crystalline TiO_2 nanotubes".

[22] Hsieh, Chien-Te, Jin-Ming Chen, Rong-Rong Kuo, and Yue-Hao Huang, App. Phys.

Lett. 84 (2004) 1186, "Fabrication of well-aligned carbon nanofiber array and its gaseous-phase adsorption behavior".

[23] Ding, J. X., J. A. Zapien, W. W. Chen, Y. Lifshitz, S. T. Lee, and X. M. Meng, Appl. Phys. Lett. 85 (2004) 2361, "Lasing in ZnS nanowires grown on anodic aluminum oxide templates".

[24] Li, Y., G. W. Meng, L. D. Zhang, and F. Phillipp, Appl. Phys. Lett. 76 (2000) 2011, "Ordered semiconductor ZnO nanowire arrays and their photoluminescence properties".

[25] Liu, Changh ong, Juan Antonio Zapien, Yuan Yao, Xiangmin Meng, Chun Sing Lee, Shoushan Fan, Yeshayahu Lifshitz, and Shuit Tong Lee, Adv. Mater. 15 (2003) 838, "High-density, ordered ultraviolet light-emitting ZnO nanowire arrays".

[26] Kyungtae Kim, Moonjung Kim, and Sung M. Cho, Materials Chemistry and Physics 96 (2006) 278, "Pulsed electrodeposition of palladium nanowire arrays using AAO template".

[27] Stoleru, V. G. and E. Towe, Appl. Phys. Lett. 85 (2004) 5152, "Optical properties of nanometer-sized gold spheres and rods embedded in anodic alumina matrices".

[28] Po-Lin Chen, Cheng-Tzu Ku, and Fu-Ming Pan, and Tzeng-Guang Tsai, Applied Physics Letters 80 (2002) 2392, "Preparation and phase transformation of highly ordered TiO2 nanodot arrays on sapphire substrates".

[29] Ataul Aziz Ikram, David T. Crouse, and Michael M. Crouse, Materials Letters 61 (2007) 3666, "Electrochemical fabrication of cadmium telluride quantum dots using porous anodized aluminum on a silicon substrate".

[30] Sauer, G., G. Brehm, S. Schneider, K. Nielsch, R. B. Wehrspohn, J. Choi, H. Hofmeister, and U. Gösele, J. Appl. Phys. 91 (2002) 3143, "Highly ordered monocrystalline silver nanowire arrays".

[31] Wang, X. F., J. Zhang, H. Z. Shi, Y. W. Wang, G. W. Meng, X. S. Peng, L. D. Zhang, and J. Fang, J. Appl. Phys. 89 (2001) 3847, "Fabrication and temperature dependence of the resistance of single-crystalline Bi nanowires".

[32] Nishizawa, Matsuhiko, Kiyoshi Mukai, Susumu Kuwabata, Charles R. Martin, and

Hiroshi Yoneyama, J. Electrochem. Soc. 144 (1997) 1923, "Template synthesis of polypyrrole-coated spinel $LiMn_2O_4$ nanotubes and their properties as cathode active materials for lithium batteries".

[33] Lakshmi, Brinda B., Charles J. Patrissi, and Charles R. Martin, Chem. Mater. 9 (1997) 2544, "Sol-gel template synthesis of semiconductor oxide micro- and nanostructures".

[34] Lei, Y., L. D. Zhang, G. W. Meng, G. H. Li, X. Y. Zhang, C. H. Liang, W. Chen, and S. X. Wang, Appl. Phys. Lett. 78 (2001) 1125, "Preparation and photoluminescence of highly ordered TiO_2 nanowire arrays".

[35] Zhang, X. Y., L. D. Zhang, W. Chen, G. W. Meng, M. J. Zheng, and L. X. Zhao, Chem. Mater. 13 (2001) 2511, "Electrochemical fabrication of highly ordered semiconductor and metallic nanowire arrays".

[36] Liang, Jianyu, Hope Chik, Aijun Yin, and Jimmy Xu, J. Appl. Phys. 91 (2002) 2544, "Two-dimensional lateral superlattices of nanostructures: Nonlithographic formation by anodic membrane template".

[37] Zhang, J., L. D. Zhang, X. F. Wang, C. H. Liang, X. S. Peng, and Y. W. Wang, J. Chem. Phys. 115 (2001) 5714, "Fabrication and photoluminescence of ordered GaN nanowire arrays".

[38] Liu, Changhong, Juan Antonio Zapien, Yuan Yao, Xiangmin Meng, Chun Sing Lee, Shoushan Fan, Yeshayahu Lifshitz, and Shuit Tong Lee, Adv. Mater. 15 (2003) 838, "High-density, ordered ultraviolet light-emitting ZnO nanowire arrays".

[39] Lee, Jin Seung, Geun Hoi Gu, Hoseong Kim, Kwang Seok Jeong, Jiwon Bae, and Jung Sang Suh, Chem. Mater. 13 (2001) 2387, "Growth of carbon nanotubes on anodic aluminum oxide templates: fabrication of a tube-in-tube and linearly joined tube".

[40] R. Gomer, Field Emission and Field Ionization, Harvard University Press, Cambridge, MA (1961)

[41] Cheng, Yuan and Otto Zhou, C. R. Physique 4 (2003) 1021, "Electron field emission from carbon nanotubes".

[42] Fowler, R. H. and L. W. Nordheim, Proc. Roy. Soc., Ser. A 119 (1928) 173, "Electron emission in intense electric fields".

[43] R. C. Smith, J. D. Carey, R. D. Forrest, and S. R. P. Silva ,J. Vac. Sci. Technol. B 23 (2005) 632,"Effect of aspect ratio and anode location on the field emission properties of a single tip based emitter".

[44] L. Nilsson, O. Groening, C. Emmenegger, O. Kuettel, E. Schaller, L. Schlapbach, H. Kind, J-M. Bonard, and K. Kern, Appl. Phys. Lett. 76 (2000) 2071, "Scanning field emission from patterned carbon nanotube films".

[45] Jung Sang Suh, Kwang Seok Jeong, Jin Seung Lee, and Intaek Han, Appl. Phys. Lett. 80 (2002) 2392, "Study of the field-screening effect of highly ordered carbon nanotube arrays".

[46] C. A. Spindt, C. E. Holland, A. Rosengreen, and I. Brodie, IEEE Trans. Electron Devices, 38, (1991) 2355, "Field-Emitter Arrays for Vacuum Microelectronics".

[47] E. Gogolides, S. Grigoropoulos, A.G. Nassiopoulos, Microelectronic Engineering 27 (1995) 449, "Highly Anisotropic Room-Temperature sub-half-micron Si Reactive Ion Etching using Fluorine only containing gases".

[48] W. Chen, H. Ahmed, Appl. Phys. Lett. 63 (1993) 1116, "Fabrication of high aspect ratio silicon pillars of <10 nm diameter".

[49] Yan Chen, Liping Guo, and David T. Shaw, Journal of Crystal Growth 210 (2000) 527, "High-density silicon and silicon nitride cones".

[50] X.D. Bai, C.Y. Zhi, S. Liu, E.G. Wang, and Z.L. Wang, Solid State Communications 125 (2003) 185, "High-density uniformly aligned silicon nanotip arrays and their enhanced field emission characteristics".

[51] C. H. Hsu, H. C. Lo, C. F. Chen, C. T. Wu, J. S. Hwang, D. Das, J. Tsai, L. C. Chen, and K. H. Chen, Nano Letters, 4 (2004) 471, "Generally Applicable Self-Masked Dry Etching Technique for Nanotip Array Fabrication".

[52] S. Johnson, A. Markwitz, M. Rudolphi, H. Baumann, S. P. Oei, K. B. K. Teo, and W. I. Milne, Appl. Phys. Lett. 85 (2004) 3277, "Field emission properties of self-assembled

silicon nanostructures on n- and p-type silicon".

[53] Tomohiro Shimizu, Tian Xie, Jo Nishikawa, Shoso Shingubara, Stephan Senz, and Ulrich Gösele, Adv. Mater. 19 (2007) 917,"Synthesis of Vertical High-Density Epitaxial Si(100) Nanowire Arrays on a Si(100) Substrate Using an Anodic Aluminum Oxide Template".

[54] V. Zorba , I. Alexandrou , I. Zergioti, A. Manousaki, C. Ducati, A. Neumeister, C. Fotakis, G.A.J. Amaratunga, Thin Solid Films 453 –454 (2004) 492, "Laser microstructuring of Si surfaces for low-threshold field-electron emission".

[55] V. Zorba, P. Tzanetakis, C. Fotakis, E. Spanakis, E. Stratakis, D. G. Papazoglou, and I. Zergioti, Appl. Phys. Lett. 88 (2006) 081103,"Silicon electron emitters fabricated by ultraviolet laser pulses".

[56] K. Seeger and R. E. Palmer, Appl. Phys. Lett. 74 (1999) 1627, "Fabrication of silicon cones and pillars using rough metal films as plasma etching masks".

[57] Y. M. Fung, W. Y. Cheung, I. H. Wilson, Dihu Chen, J. B. Xu, S. P. Wong, and R. W. M. Kwok, J. Vac. Sci. Technol. B 19 (2001) 884, "Electron field emission characteristics of textured silicon surface".

[58] G S Huang, XLWu, Y C Cheng, X F Li, S H Luo, T Feng and Paul K Chu, Nanotechnology 17 (2006) 5573, "Fabrication and field emission property of a Si nanotip array".

[59] Du, G. H., Q. Chen, R. C. Che, Z. Y. Yuan, and L.-M. Peng, Appl. Phys. Lett. 79 (2001) 3702, "Preparation and structure analysis of titanium oxide nanotubes".

[60] Lei, Y., L. D. Zhang, G. W. Meng, G. H. Li, X. Y. Zhang, C. H. Liang, W. Chen, and S. X. Wang, Appl. Phys. Lett. 78 (2001) 1125, "Preparation and photoluminescence of highly ordered TiO2 nanowire arrays".

[61] B Xiang, Y Zhang, Z Wang, X H Luo, YW Zhu, H Z Zhang and D P Yu, J. Phys. D: Appl. Phys. 38 (2005) 1152, "Field-emission properties of TiO2 nanowire arrays".

[62] Po-Lin Chen, Wen-Jun Huang, Jun-Kai Chang, Cheng-Tzu Kuo, and Fu-Ming Pan, Electrochemical and Solid-State Letters, 8 (2005) H83, "Fabrication and Field Emission

Characteristics of Highly Ordered Titanium Oxide Nanodot Arrays".

[63] Kumar, Krishnankutty-Nair P., Scr. Metall. Mater. 32 (1995) 873, "Growth of rutile crystallites during the initial stage of anatase-to-rutile transformation in pure titania and in titania-alumina nanocomposites".

[64] Zhang, Hengzhong, Feng Huang, Benjamin Gilbert, and Jillian F. Banfield, J. Phys Chem. B 104 (2000) 3481, "Molecular dynamics simulations, thermodynamic analysis, and experimental study of phase stability of zinc sulfide nanoparticles".

[65] Zhang, Hengzhong and Jillian F. Banfield, J. Mater. Chem. 8 (1998) 2073, "Thermodynamic analysis of phase stability of nanocrystalline titania".

[66] S. Kanamori, Thin Solid Films 136 (1986) 195, "Investigation of reactively sputtered TiN films for diffusion barriers".

[67] N. Kumar, J. T. McGinn, K. Pourrexaei, B. Lee, and E. C. Douglas, J. Vac. Sci. Technol. A 6, (1988) 1602, "Transmission electron microscopy studies of brown and golden titanium nitride thin films as diffusion barriers in very large scale integrated circuits ".

[68] J. M. Poitevin and G. Lemperiere, Thin Solid Films 97 (1982) 69, "Influence of substrate bias on the composition, structure and electrical properties of reactively d.c.-sputtered TiN films".

[69] N. Yokoyama, K. Hinode, and Y. Homma, J. Electrochem. Soc. 138 (1991) 190, "LPCVD Titanium Nitride for ULSIs".

[70] Jae-Woong Nah, Byoung-June Kim, Dong-Kak Lee, and Jung-Joong Lee, J. Vac. Sci. Technol. A 17 (1999) 463, "Color, structure, and properties of TiN coatings prepared by plasma enhanced chemical vapor deposition".

[71] Dong-Gu Lee, Dong-Ki Baik, Nam-Seok Kang, Won-Ki Cho, Sang-Jo Yoon, Tae-Young Kim, Hyun-Deog Hwang, Dong-Hoon Ahn, and Myung-Ho Park, J. Vac. Sci. Technol. B 18 (2000) 1085, "Fabrication of volcano-type TiN field emitter arrays".

[72] Y. Hu, K. Huo, Y. Ma, Y. Lu, J. Xu, Z. Hu and Y. Chen, J. of Nanosci. and Nanotechnology, 7 (2007) 2922, "Synthesis and field emission characterization of

titanium nitride nanowires".

[73]   Seung-Youl Kang, Jin Ho Lee, Yoon-Ho Song, Yuon Tae Kim, Kyoung Ik Cho, and Hyung Joun Yoo, J. Vac. Sci. Technol. B 16 (1998) 871, "Emission characteristics of TiN-coated silicon field emitter arrays".

[74]   S. Albin, W. Fu, A. Varghese, A. C. Lavarias, and G. R. Myneni, J. Vac. Sci. Technol. A, 17 (1999) 2104, "Diamond coated silicon field emitter array".

[75]   J. Liu, V.V. Zhirnov, A.F. Myers, G.J. Wojak, W.B. Choi, J.J. Hren, S.D. Wolter, M.T. McClure, B.R. Stoner, J.T. Glass, J. Vac. Sci. Technol. B: 13 (1995) 422, "Field emission characteristics of diamond coated silicon field emitters".

[76]   W.P. Kang, J.L. Davidson, M. Howell, B. Bhuva, D.L. Kinser, D.V. Kerns, Q. Li, J.F. Xu, J. Vac. Sci. Technol. B: 14 (1996) 2068, "Micropatterned polycrystalline diamond field emitter vacuum diode arrays".

[77]   V.V. Zhirnov, A.B. Voronin, E.I. Givargizov, A.L. Meshchery kova, J. Vac. Sci. Technol. B: 14 (1996) 2034, "Emission stability and high current performance of diamond-coated Si emitters".

[78]   M.-Y. Jung, D.W. Kim, S.S. Choi, Y. Kim, Y. Kuk, K.C. Park, J. Jang, Thin Solid Films 294 (1997) 157, "Fabrication of a nanosize Si-tip coated with a thin diamond-like carbon film".

[79]   S. Lee, S. Lee, S. Lee, D. Jeon, K.-R. Lee, J. Vac. Sci. Technol. B: 15 (1997) 457, "Self-aligned silicon tips coated with diamondlike carbon".

[80]   S. Lee, B.-K. Ju, Y.-H. Lee, D. Jeon, M.-H. Oh, J. Vac. Sci. Technol. B: 15 (1997) 425, "Fabrication and field emission study of gated diamondlike-carbon-coated silicon tips".

[81]   C.-G. Ko, B.-K. Ju, Y.-H. Lee, J.-H. Park, M.-H. Oh, Jpn. J. Appl. Phys. 35 (1996) L1305, "Fabrication and Characterization of Diamond-Like Carbon Coated Knife Edge Field Emitter Array".

[82]   P. J. Fallon and L. M. Brown, Diamond Relat. Mater. **2** (1993) 1004, "Analysis of chemical-vapour-deposited diamond grain boundaries using transmission electron microscopy and parallel electron energy loss spectroscopy in a scanning transmission

electron microscope".
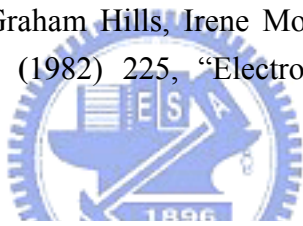
[83] Takuji Nakagawa, Keisuke Kageyama, Hiroshi Takage, Yukio Sakabe, Soshu Kirihara, and Yoshinari Miyamoto, Japanese Journal of Applied Physics 46 (2007) 7117, "Diamond-Structure Photonic Crystals Composed of Ceramic Spheres in Resin and Their Microwave Properties".

[84] C. Z. Wang and K. M. Ho, Physical Review Letters 71 (1993) 1184, "Structure, Dynamics, and Electronic Properties of Diamondlike Amorphous Carbon".

[85] J. Robertson, Phys. Rev. B 53 (1996) 16302, "Recombination and photoluminescence mechanism in hydrogenated amorphous carbon".

[86] N. A. Fox, W. N. Wang, T. J. Davis, J. W. Steeds, and P. W. May, Appl. Phys. Lett. 71 (1997) 2337, "Field emission properties of diamond films of different qualities".

[87] Ph. Niedermann, W. Ha¨nni, N. Blanc, R. Christoph, and J. Burger, J. Vac. Sci. Technol. A 14 (1996) 1233, "Chemical vapor deposition diamond for tips in nanoprobe experiments".

[88] V. V. Zhirnov, E. I. Givargizov, A. V. Kandidov, B. V. Seleznev, and A. N. Alimova, J. Vac. Sci. Technol. B 15 (1997) 446, "Emission characterization of diamond-coated Si field emission arrays".

[89] H. C. Cheng, T. K. Ku, B. B. Hsien, S. H. Chen, S. Y. Leu, C. C. Wang, C. F. Chen, I. J. Hsieh, and J. C. M. Huang, Jpn. J. Appl. Phys., Part 1 34 (1995) 6926, "Fabrication and Characterization of Diamond-Clad Silicon Field Emitter Arrays".

[90] F. Y. Chuang, C. Y. Sun, H. F. Cheng, W. C. Wang, C. M. Huang, and I. N. Lin, Technical Digest of the 9th International Vacuum Microelectronics Conference, St. Petersburg, Russia, 7–12 July 1996, p. 339.

[91] B. S. Satyanarayana, A. Hart, W. I. Milne, and J. Robertson, Appl. Phys. Lett. 71 (1997) 1430, "Field emission from tetrahedral amorphous carbon".

[92] R. S. Becker, G. S. Higashi, Y. Chabal, and A. J. Becker, Phys. Rev. Lett. 65 (1990) 1917, "Atomic-scale conversion of clean Si(111):H-1×1 to Si(111)-2×1 by electron-stimulated desorption".

[93]   D. R. Tallant, J. E. Parmeter, M. P. Siegal, and R. L. Simpson, Diam. Relat. Mater. 4 (1995) 191, "The thermal stability of diamond-like carbon".

[94]   G. A. J. Amaratunga and S. R. P. Silva, Appl. Phys. Lett. 68 (1996) 2529, "Nitrogen containing hydrogenated amorphous carbon for thin-film field emission cathodes".

[95]   V. S. Veersamy, J. Yuan, G. A. J. Amaratunga, W. I. Milne, K.W. R. Gilkes, M.Weilner, and L. M. Brown, Phys. Rev. B 48 (1993) 17954, "Nitrogen doping of highly tetrahedral amorphous carbon".

[96]   Y. Jung, J. Lee, and Y. Tak, Electrochemical and Solid-State Letters, 7 (2004) H5, "Electrochromic Mechanism of IrO2 Prepared by Pulsed Anodic Electrodeposition".

[97]   M. Yagi, E. Tomita, and T. Kuwabara, Journal of Electroanalytical Chemistry, 579 (2005) 83, "Remarkably high activity of electrodeposited IrO_2 film for electrocatalytic water oxidation".

[98]   J. M. Zhang, C. J. Lin, Z. D. Feng, and Z. W. Tian, Journal of Electroanalytical Chemistry, 452 (1998) 235, "Mechanistic studies of electrodeposition for bioceramic coatings of calcium phosphates by an in situ pH-microsensor technique".

[99]   B. R. Chalamala, R. H. Reuss, K. A. Dean, E. Sosa, and David E. Golden, J. Appl. Phys., 91 (2002) 6141, "Field emission characteristics of iridium oxide tips".

[100] R. S. Chen, Y. S. Huang, Y. m. Liang, C. S. Hsieh, D. S. Tsai, K. K. Tiong, Applied Physics Letters 84 (2004) 1552, "Field emission from vertically aligned conductive IrO2 nanorods".

[101] Kazusuke Yamanaka, Jpn. J. Appl. Phys. 28 (1989) 632, "Anodically Electrodeposited Iridium Oxide Films (AEIROF) from Alkaline Solutions for Electrochromic Display Devices".

[102] M. A. Petit and V. Plichon, Journal of electroanalytical chemistry, 444 (1998) 247, "Anodic electrodeposition of iridium oxide films".

[103] R. K. Kawar, P. S. Chigare, P. S. Patil, Applied Surface Science, 206 (2003) 90, "Substrate temperature dependent structural, optical and electrical properties of spray

deposited iridium oxide thin films".

[104] P. C. Liao, W. S. Ho, Y. S. Huang, and K. K. Tiong, Journal of Materials Research, 13 (1998) 1318, "Characterization of sputtered iridium dioxide thin films".

[105] R. S. Chen, A. Korotcov, Y. S. Huang, and D. S. Tsai, Nanotechnology, 17 (2006) R67, "One-dimensional conductive IrO_2 nanocrystals".

[106] B. R. Chalamala, Y. Wei, R. H. Reuss, S. Aggarwal, S. R. Perusse, B. E. Gnade, and R. Ramesh, J. Vac. Sci. Technol. B 18 (2000) 1919, "Stability and chemical composition of thermally grown iridium-oxide thin films".

[107] M. A. EI Khakani, M. Chaker, and E. Gat, Applied Physics Letters 69 (1996) 2027, "Pulsed laser deposition of highly conductive iridium oxide thin films".

[108] http://www.webelements.com/webelements/compounds/text/Ir/Ir1O2-12030498.html

[109] M. Ohring, The Materials Science of Thin Films, Academic Press, New York, 1992, P.197

[110] Romankiw L T and Palumbo T A 1988 Electrodeposition Technology, Theory and Practice ed L T Romankiw and D R Turner (Pennington, NJ: Electrochemical Society) p 13

[111] Budevski E B 1983 Comprehensive Treatise of Electrochemistry vol 7, ed B E Conway et al (New York: Plenum) p 399

[112] Budevski E, Staikov G and Lorenz W J 1996 Electrochemical Phase Formation and Growth (Weinheim: VCH)

[113] A. Milcheva, E. Vassilevaa and V. Kertov, J. Electroanal. Chem. 107 (1980) 323, "Electrolytic nucleation of silver on a glassy carbon electrode Part I. Mechanism of critical nucleus formation".

[114] A. Milchev and E. Vassileva, J. Electroanal. Chem. 107 (1980) 337, "Electrolytic nucleation of silver on a glassy carbon electrode Part II. Steady-state nucleation rate".

[115] A. Milchev and S. Stoyanov, J. Electroanal. Chem. 72 (1976) 33, "Classical and

atomistic models of electrolytic nucleation Comparison with experimental data".

[116] Gamini Gunawardena, Graham Hills and Irene Montenegro, J. Electroanal. Chem. 138 (1982) 241, "Electrochemical nucleation Part II. The electrodeposition of silver on vitreous carbon".

[117] G. Scherb and D. M. Kolb, J. Electroanal. Chem. 396 (1995) 151, "Cu deposition onto n-GaAs(100): optical and current transient studies".

[118] P. M. Vereecken, K. Strubbe and W. P. Gomes, J. Electroanal. Chem. 433 (1997) 19, "An improved procedure for the processing of chronoamperometric data: Application to the electrodeposition of Cu upon (100) n-GaAs".

[119] Southampton Electrochemistry Group 1990 Instrumental Methods in Electrochemistry (New York: Ellis Horwood)

[120] Gamini Gunawardena, Graham Hills, Irene Montenegro and Benjamin Scharifker, J. Electroanal. Chem. 138 (1982) 225, "Electrochemical nucleation Part I. General considerations".

[121] Benjamin Scharifker and Graham Hills, J. Electrochim. Acta 28 (1983) 879, "Theoretical and experimental studies of multiple nucleation".

[122] E. Bosco and S. K. Rangarajan, J. Electroanal. Chem. 134 (1982) 213, "Electrochemical phase formation (ECPF) and macrogrowth Part I. Hemispherical   models".

[123] M. Y. Abyaneh, Electrochim. Acta 27 (1982) 1329, "Calculation of overlap for nucleation and three-dimensional growth of centres".

[124] Alexander Milchev, Electrochim. Acta 28 (1983) 947, "Role of the substrate state in electrochemical nucleation".

[125] M. Sluyters-Rehbach, J. H. O. J. Wijenberg, E. Bosco, and J. H. Sluyters, J. Electroanal. Chem. 236 (1987) 1, "The theory of chronoamperometry for the investigation of electrocrystallization Mathematical description and analysis in the case of

diffusion-controlled growth".

[126] M. V. Mirkin and A. P. Nilov, J. Electroanal. Chem. 283 (1990) 35, "Three-dimensional nucleation and growth under controlled potential".

[127] A. Milchev, W. S. Kruijt, M. Sluyters-Rehbach, and J. H. Sluyters, J. Electroanal. Chem. 350 (1993) 89, "Probabilistic analysis of the distance between clusters randomly distributed on the electrode surface".

[128] Jan W. M. Jacobs, J. Electroanal. Chem. 247 (1988) 135, "Note on a theory of three-dimensional electrochemical nucleation with diffusion-controlled growth".

[129] G Oskam, J G Long, A Natarajan and P C Searson, J. Phys. D: Appl. Phys. 31 (1998) 1927, "Review article: Electrochemical deposition of metals onto silicon".

[130] Yoshihiro Nakato, Keiichi Ueda, Hiroyuki Yano, and Hiroshi Tsubomura, J. Phys. Chem. 92 (1988) 2316, "Effect of microscopic discontinuity of metal overlayers on the photovoltages in metal-coated semiconductor-liquid junction photoelectrochemical cells for efficient solar energy conversion".

[131] P. Bindra, H. Gerischer, and D. M. Kolb, J. Electrochem. Soc. 124 (1977) 1012, "Electrolytic Deposition of Thin Metal Films on Semiconductor Substrates".

[132] Oskam G, Long J G, Nikolova M and Searson P C 1997 Electrochemical Synthesis and Characterization of Materials ed P C Andricacos et al (New York: Materials Research Society) p 257

[133] G. Oskam, L. Bart, D. Vanmaekelbergh, and J. J. Kelly J. Appl. Phys. 74 (1993) 3238, "The electrical and electrochemical properties of gold-plated InP".

[134] G. Oskam, D. Vanmaekelbergh, and J. J. Kelly, Electrochim. Acta 38 (1993) 1115, "The influence of electrodeposited gold on the properties of III–V semiconductor

electrodes—part 3. Results on *n*-GaAs provided with thick gold l".

[135] A. Mozalev, G. Gorokh, M. Sakairi, and H. Takahashi, Journal of materials science 40 (2005) 6399,"The growth and electrical transport properties of self-organized metal/oxide nanostructures formed by anodizing Ta-Al thin-film bilayers".

[136] Ching-Jung Yang, Chih Chen, Pu-Wei Wu, Jia-Min Shieh, Shun-Min Wang, and Shih-Wei Liang, J. Mater. Res., 22 (2007) 1064, "Fabrication of ordered Ta_2O_5 nanodots using an anodic aluminum oxide template on Si substrate".

[137] Chia-Tien Wu, Fu-Hsiang Ko *, Hsin-Yen Hwang, Microelectronic Engineering, 83 (2006) 1567,"Self-aligned tantalum oxide nanodot arrays through anodic alumina template".

[138] Sun-Kyu Hwang, Junghyun Lee, Soo-Hwan Jeong, Pyung-Soo Lee, and Kun-Hong Lee, Nanotechnology 16 (2005) 850,"Fabrication of carbon nanotube emitters in an anodic aluminium oxide nanotemplate on a Si wafer by multi-step anodization".

[139] Hirokazu Shiraki, Yasuo Kimura, Hisao Ishii, Sachiko Ono, Kingo Itaya, and Michio Niwano, Applied Surface Science 237 (2004) 369, "Investigation of formation processes of an anodic porous alumina film on a silicon substrate".

[140] N. I. Tatarenko and A. M. Mozalev, Solid-State Electronics, 45 (2001) 1009, "Geometry and element composition of a nanoscale field emission array formed by self-organization in porous anodic aluminum oxide".

[141] Po-Lin Chen, Cheng-Tzu Kuo, Tzeng-Guang Tsai, Bo-Wei Wu, Chiung-Chih Hsu, and Fu-Ming Pan, Appl. Phys. Lett. 82 (2003) 2796, "Self-organized titanium oxide nanodot arrays by electrochemical anodization".

[142] Farver, John R. and Richard A. Yund, Earth Planet. Sci. Lett. 161 (1998) 189, "Oxygen grain boundary diffusion in natural and hot-pressed calcite aggregates".

[143] H. Ham, G. Z. Shen, J. H Cho, T. J. Lee, S. H. Seo and C. J. Lee, Chem. Phys. Lett., 404 (2005) 69,"Vertically aligned ZnO nanowires produced by a catalyst-free thermal evaporation method and their field emission properties".

[144] C. S. Hsieh, G. Wang, D. S. Tsai, R.S. Chen and Y. S. Huang, Nanotechnology, 16 (2005)

1885, "Field emission characteristics of ruthenium dioxide nanorods".

[145] X. Xiang and H. Zhu, Appl. Phys. A, 87 (2007) 651, "One-dimensional gallium nitride micro/nanostructures synthesized by a space-confined growth technique".

[146] Y. Hu, K. Huo, Y. Ma, Y. Lu, J. Xu, Z. Hu and Y. Chen, J. of Nanosci. and Nanotechnology, 7 (2007) 2922, "Synthesis and field emission characterization of titanium nitride nanowires".

[147] P. L. Chen, C. T. Kuo, F. M. Pan, and T. G. Tsai, Appl. Phys. Lett., 84 (2004) 3888, "Self-organized titanium oxide nanodot arrays by electrochemical anodization".

[148] T. M. Chen, F. M. Pan, J. Y. Hung, L. Chang, S. C. Wu, and C. F. Chen, J. Electrochem. Soc., 154 (2007) D215, "Amorphous Carbon Coated Silicon Nanotips Fabricated by MPCVD Using Anodic Aluminum Oxide as the Template".

[149] Zhang, Hengzhong and Jillian F. Banfield, J. Mater. Chem. 8 (1998) 2073, "Thermodynamic analysis of phase stability of nanocrystalline titania".

[150] P. L. Chen, J. K. Chang, C. T. Kuo, and F. M. Pan, Appl. Phys. Lett., 86 (2005) 123111-1, "Field emission of carbon nanotubes on anodic aluminum oxide template with controlled tube density".

[151] V. A. Solntsev and A. N. Rodionov, Solid State Electronics, 45 (2001) 853, "Investigation of electric field at the cathode with fractal structure of the surface".

[152] H. G. Kosmahl, IEEE Trans. Electron Devices., 38 (1991) 1534, "Analytic Evaluation of Field Emission Enhancement Factors for Ellipsoidal Cones and Elliptic Cross-Section Wedges".

[153] D. Nicolaescu, J. Vac. Sci. Technol. B, 12 (1994) 759, "Technological parameters distribution effects on the current-voltage characteristics of field emitter arrays".

[154] I. Brodie and P. R. Schwoebel, Porc. IEEE, 82 (1994) 1006, "Vacuum Microelectronic Devices".

[155] Po-Lin Chen, Jun-Kai Chang, Cheng Tzu Kuo, and Fu-Ming Pan, Diamond and Related Materials, 13 (2004)1949, "Anodic aluminum oxide template assisted growth of

vertically aligned carbon nanotube arrays by ECR-CVD".

[156] O. L. Golubev, T. I. Sudakova, and V. N. Shrednik, Technical Physics, 45(2000) 1575, "Temperature Dependence of the Work Function of Hafnium Islands on Tungsten".

[157] R. Z. Bakhtizin, S. S. Ghots, and E. K. Ratnikova, IEEE Transactions On Electron Devices, 38 (1991) 2398, "GaAs Field Emitter Arravs".

[158] S. H. Ahn, K. R. Lee, K. Y. Eun, and Dongryul Jeon, Surface and Coatingd Technology, 120-121 (1999) 734, "Stabilized field emission behavior of diamond-like carbon-coated Si tips".

[159] J. C. She, S. Z. Deng, N. S. Xu, R. H. Yao, and J. Chen, Applied Physics Letters, 88 (2006) 013112, "Fabication of vertically aligned Si nanowires and their application in a gated field emission device".

[160] J. C. She, K. Zhao, S. Z. Deng, J. Chen, and N. S. Xu, Applied Physics Letters, 87 (2005) 052105, "Field electron emission of Si nanotips with apexes of various compositions".

[161] H. C. Lo, J. S. Hwang, K. H. Chen, C. H. Hsu, C. F. Chen, and L. C. Chen, Applied Physics Letters, 83 (2003) 1420, "SiC-capped nanotip arrays for field emission with ultralow turn-on field".

[162] Q. Wang, J. J. Li, Y. J. Ma, X. D. Bai, Z. L. Wang, P. Xu, C. Y. Shi, B. G. Quan, S. L. Yue, and C. Z. Gu., Nanotechnology, 16 (2005) 2919, "Field emission properties of carbon coated Si nanocone arrays on porous silicon".

[163] Po-Lin Chen, Cheng Tzu Kuo, Tzeng-Guang Tsai, Bo-Wei Wu, Chiung-Chih Hsu, and Fu-Ming Pan, Applied Physics Letters, 82 (2003) 2796, "Self-organized titanium oxide nanodot arrays by electrochemical anodization".

[164] M.A. Tamor and W.C. Vassell, J. Appl. Phys., 76 (1994) 3823, "Raman "fingerprinting" of amorphous carbon films".

[165] A.C. Ferrari and J. Robertson, Phys. Rev. B, 61 (2000) 14095, "Interpretation of Raman spectra of disordered and amorphous carbon".

[166] K. B. K. Teo, M. Chhowalla, G. A. J. Amaratunga, W. I. Milne, G. Pirio, P. Legagneux, F. Wyczisk, J. Olivier, and D. Pribat , J. Vac. Sci. Technol. B, 20 (2002) 116, "Characterization of plasma-enhanced chemical vapor deposition carbon nanotubes by Auger electron spectroscopy".

[167] S.-C Seo and D.C. Ingram, J. Vac. Sci. Technol. A, 15 (1997) 2579, "Fine structures of valence-band, x-ray-excited Auger electron, and Plasmon energy loss spectra of diamondlike carbon films obtained using x-ray photoelectron spectroscopy".

[168] Teo, K. B. K., M. Chhowalla, G. A. J. Amaratunga, W. I. Milne, G. Pirio, P. Legagneux, F. Wyczisk, J. Olivier, and D. Pribat, J. Vac. Sci. Technol. B 20 (2002) 116, "Characterization of plasma-enhanced chemical vapor deposition carbon nanotubes by Auger electron spectroscopy".

[169] C. A. Spindt, I. Brodie, L. Humphrey, and E.R. Westerberg, J. Appl. Phys., 47 (1976)5248," Physical properties of thin-film field emission cathodes with molybdenum cones".

[170] Z. Xu, X. D. Bai, E. G. Wang, and Z. L. Wang, Applied Physics Letters, 87 (2005) 163106," Field emission of individual carbon nanotube with in situ tip image and real work function".

[171] G. Z. Yue., Q. Qiu, Bo Gao, Y. Cheng, J. Zhang, H. Shimoda, S. Chang, J. P. Lu, and O. Zhou, Applied Physics Letters, 81 (2002) 355,"Generation of continuous and pulsed diagnostic imaging x-ray radiation using a carbon-nanotube-based field-emission cathode".

[172] W. A. de Heer, A. Châtelain, and D. Ugarte, Science, 270 (1995) 1179, "A Carbon Nanotube Field-Emission Electron Source".

[173] Y. Saito and S. Uemura, Carbon, 38 (2000) 169, "Field emission from carbon nanotubes and its application to electron sources".

[174] J. M. Bonard, J. P. Salvetat, T. Stöckli, W. A. de Heer, L. Forró, and A. Châtelain, Applied Physics Letters, 73 (1998) 918,"Field emission from single-wall carbon nanotube films".

[175] Y. K. Tseng, C. J. Huang, H. M. Chen, I. N. Lin, K. S. Liu, and I. C. Chen, Adv. Funct.

Mater., 13 (2003) 811, "Characterization and field emission properties of needle-like zinc oxide nanowires grown vertically on conductive zinc oxide films".

[176] S. H. Jo, J. Y. Lao, Z. F. Ren, R. A. Farrer, T. Baldacchini, and J. T. Fourkas, Applied Physics Letters, 83 (2003) 4821,"Field-emission studies on thin films of zinc oxide nanowires".

[177] Te Ming Chen, Jui-Yi Hung, Fu-Ming Pan, L. Chang, J.-T. Sheu, and Shich-Chuan Wu, Electrochemical and Solid-State Letters, 11 (2008) K40,"Fabrication and Field-Emission Characteristics of TiN Nanorods with a Concave Top Surface".

[178] B. R. Chalamala, Y. Wei, R. H. Reuss, S. Aggarwal, B. E. Gnade, R. Ramesh, J. M. Bernhard, E. D. Sosa, and D. E. Golden, Appl. Phys. Lett.,74 (1999) 1394, "Effect of growth conditions on surface morphology and photoelectric work function characteristics of iridium oxide thin films".

[179] R. S. Chen, Y. S. Huang, Y. M. Liang, D. S. Tsai, Y. Chi, and J. J. Kai, Journal of Materials Chemistry, 13 (2003) 2525, "Growth control and characterization of vertically aligned IrO_2 nanorods".

[180] D. Nicolaescu, J. Vac. Sci. Technol. B, 11 (1993) 392," Physical basis for applying the Fowler-Nordheim J-E relationship to experimental I-V data".

[181] N. S. Xu, J. C. She, S. E. Huq, J. Chen, and S. Z. Deng, Applied Physics Letters, 73 (1998) 3668, "Enhancing electron emission from silicon tip arrays by using thin amorphous diamond coating".

Vita

姓名：陳德銘

性別：男

生日：1976.11.13

聯絡住址：302 新竹縣竹北市嘉祥一街 51 巷 6 號 2 樓

E-mail: fiber133@yahoo.com.tw

學歷

博士班	交通大學	材料科學與工程研究所	2002 ~ 2008
碩士班	義守大學	材料科學與工程研究所	2000 ~ 2002
大　學	義守大學	材料科學與工程學系	1996 ~ 2000

碩士論文題目：製程條件對縮墨鑄鐵及 TiC 強化縮墨鑄鐵基複合材料影響

之研究

證　　　　照：專利工程師

List of Publications

Journal Papers:

1. Te-Ming Chen, Jui-Yi Hung, Fu-Ming Pan, L. Chang, J.-T. Sheu, and Shich-Chuan Wu,"Fabrication and Field Emission Characteristics of TiN Nanorods with a Concave Top Surface", Electrochemical and Solid-State Letters, 11, K40 (2008).

2. Te Ming Chen, F. M. Pan, J. Y. Hung, L. Chang, S. C. Wu, and C. F. Chen, "Amorphous Carbon Coated Silicon Nanotips Fabricated by MPCVD Using Anodic Aluminum Oxide as the Template", Journal of the electrochemical society, 154, D215 (2007).

3. Te-Ming Chen, J. Y. Hung, Fu-Ming Pan, L. Chang, S. C. Wu, and Ta-Chang Tien, "Pulse Electrodeposition of Iridium Oxide on Silicon Nanotips for Field Emission study", submitted to Journal of Nanoscience and Nanotechnology (accept).

4. Jitendra N. Tiwari, Te-Ming Chen, Fu-Ming Pan, Kun-Lin Lin, "Ordered silicon nanocones as a highly efficient platinum catalyst support for direct methanol fuel cells ", Journal of Power Sources, 182, 510 (2008).

Conference Papers:

1. Te-Ming Chen, Jui-Yi Hung, Fu-Ming Pan, L. Chang, and Shich-Chuan Wu,"Field-Emission Study of TiN Nanorods with a Concave Top Surface ", SNDT-2008.

2. Te-Ming Chen , Jui-Yi Hung, Fu-Ming Pan , and L. Chang ,"Surface Modification of Si Nanocones Fabricated by Porous Anodic Aluminum Oxide Templation" , MRS-2007.

3. Te-Ming Chen , Jui-Yi Hung, Fu-Ming Pan , and L. Chang,"Fabrication and Field Emission Characteristics of TiN Nanorods with a Concave Top Surface" , AVS-2007.

4. Te-Ming Chen, Fu-Ming Pan, Jui-Yi Hung, L. Chang, and Shich-Chuan Wu," Surface Modification of Si Nanocones Fabricated by Porous Anodic Aluminum Oxide Templation" , SNDT-2007.

5. Te-Ming Chen, Fu Ming Pan, L. Chang, and Jui-Yi Hung," Fabrication of carbon

coated silicon nanocone field emitters templated by porous anodic aluminum oxide”,
中國材料科學學會 95 年會論文發表會.